University of Sussex

OBSERVING THE EPOCH OF REIONIZATION AND DARK AGES WITH REDSHIFTED 21-CM HYDROGEN LINE

Hemant Shukla

Thesis submitted for the degree of Doctor of Philosophy to
University of Sussex
December 2014

Dedicated to:

Papa, Maate, and Behan.

UNIVERSITY OF SUSSEX

Hemant Shukla, Doctor of Philosophy

Observing the Epoch of Reionization and Dark Ages with redshifted 21-cm hydrogen line

Summary

The billion years subsequent to the Big Bang pose the next challenging frontier for precision cosmology. The concordant cosmological model, ΛCDM, propounds that during this period, the dark matter gravitationally shepherds the baryonic matter to form the primordial large-scale structures. This era is termed the Dark Ages (DA). The following era, the Epoch of Reionization (EoR), leads to the formation of the first stars and galaxies that reionize the permeating neutral hydrogen. The linear polarization of the cosmic background radiation and the Gunn-Peterson troughs in quasar absorption spectra provide indirect evidence for the EoR. Currently, there is no observational evidence for the DA.

While state-of-the-art radio telescope arrays, Low Frequency Array (LOFAR) and Square Kilometre Array (SKA), propose various strategies to observe the early phases of the Universe, the advanced simulations employing high-performance computing (HPC) methodologies continue to play significant role in constraining various models based upon limited observational data. Despite a wide range of research, there is no end-to-end simulation solution available to quantifiably address the observational challenges due to statistical and systematic errors including foregrounds, ionosphere, polarization, RFI, instrument stability, and directional dependent gains.

This research consolidates the cutting-edge simulation solutions, Cube-P^3M, C^2-Ray, and MeqTrees, to build an HPC prototype pipeline entitled, Simulating Interferometry Measurements (SIM). To establish and validate the efficacy of the SIM pipeline, the research builds a theoretical framework of two science drivers, *viz.*, the presence of Lyman-limit absorbers and measuring non-Gaussianity from the 21-cm data. Thereafter, using the LOFAR and SKA telescope configurations, the SIM generates data visibility cubes with direction dependent and independent propagation effects. Finally, SIM extracts the original signal through standard techniques exploring the parametric phase-space. Results are presented herein.

Preface

For thousands of years, the human species, in disparate emerging civilizations, has wondered about the very existence of the self and beyond. The species has posited profound and compelling questions, often addressing them with the power of imagination. The human spirit has soared on the wings of imagination to discover the very nature of the physical. The hovering vast dark globe of the night, punctuated with the seemingly distant glimmering lights has continued to kindle that imagination. My ancestors in India posited such questions many thousands of years ago. They disseminated their thoughts through chants delivered on rhythmic metre; a tradition practiced even today all across India. The writing of the thoughts came much later. Below, I share the verse from one such collection of thoughts, called Rig Veda, for its imaginary leap into the unknown; for its liberated thought; for its brilliance of wonderment that on occasion carries us not far from the truth; the illusive truth, which we continue to seek through the rigors and disciplines of science.

नासदासीन्नो सदासीत् तदानीं नासीद्रजो नो व्योमा परो यत्।
किमावरीवः कुह कस्य शर्मन्नम्भ्ः किमासीद्गहनं गभीरम्॥ १
न मृत्युरासीदमृतं न तर्हि न रात्र्या अह्न आसीत् प्रकेतः।
आनीदवातं स्वधया तदेकं तस्माद्धान्यन्न परः किं चनास॥ २
तम आसीत् तमसा गूलहमग्रे ऽप्रकेतं सलिलं सर्वमा इदम्।
तुच्छ्येनाभ्वपिहितं यदासीत् तपसस्तन्महिनाजायतैकम्॥ ३
कामस्तदग्रे समवर्ततधि मनसो रेतः प्रथमं यदासीत्।
सतो बन्धुमसति निरविन्दन् हृदि प्रतीष्या कवयो मनीषा॥ ४
तिरश्चीनो विततो रश्मिरेषामधः स्विदासीदुपरि स्विदासीत्।
रेतोधा आसन् महिमान आसन् त्स्वधा अवस्तात् प्रयतिः परस्तात॥ ५
को अद्धा वेद क इह प्र वोचत् कुत आजाता कुत इयं ।
अर्वाग्देवा अस्य विरर्जनेनाऽथा को वेद यत आबभूव॥ ६
इयं विसृष्टियर्त् आबभूव यदि वा दधे वा न।
यो अस्याध्यक्षः परमे व्योमन् त्सो अंग वेद यदि वा न वेद॥ ७

ऋगवेद - म॰ १० । अनु॰ ११ । सू॰ १२९

The verse from ancient Rig Veda contemplates the creation of the Universe and unabashedly enquires aloud the meaning and purpose of it all. There are many translations of the texts. Following is one such translation that was done in the late 1890s by an Indian philosopher named Vivekanand.

Then there was no existence, nor non-existence,
There was no world, nor the sky beyond.
What covered the mist? Of whom was that?
What was in the depths of darkness thick? [1]

Death was not then, nor immortality,
The night was neither separate from day,
But motionless did That vibrate
Alone, with Its own glory one -
Beyond That nothing did exist. [2]

At first in darkness hidden darkness lay,
Undistinguished as one mass of fluid,
Then That which lay in void thus covered
A glory did put forth by *Tapah* [heat]! [3]

First desire rose, the primal seed of mind,
(The sages have seen all this in their hearts
Sifting existence from non - existence.)
Its rays above, below and sideways spread. [4]

Creative then became the glory,
With self-sustaining principle below.
And Creative Energy above. [5]

Who knew the way? Who there declared
Whence this arose? Projection whence?
For after this projection came the gods.
Who therefore knew indeed, came out this whence? [6]

This projection whence arose,
Whether held or whether not,
He the ruler in the supreme sky, of this
He, O Sharman! knows, or knows not
He perchance! [7]

The Hymn of Creation
(A translation of the Nâsadiya-Sukta, Rig-Veda, X. 129.)
The Complete Works of Vivekananda (Volume 6), published, 1907

Acknowledgements

This research work started on January 7, 2011, in rather unusual and unprecedented circumstances. I was admitted to the University of Sussex doctoral program in physics with a fellowship. I was to be the full-time student, remotely located in the USA, where I was a full-time employee of the University of California/Lawrence Berkeley National Lab, Berkeley CA, leading my National Science Foundation funded project, ISAAC, developing advanced computational infrastructure for astrophysics applications and running a center that I had founded called ICCS. With all hands full, began a hectic yet most wonderful journey of erudition and exploration that I had always wished to embark upon. This journey was made seamless by the unwavering support and encouragement of many whom I get the privilege to thankfully acknowledge.

I would like to thank my advisor, Ilian Iliev, for his guidance over the years. While separated by the pond, our weekly online meetings allowed us to maintain a clear path for the research. Ilian's patient advice interlaced with doomsday warnings was the perfect recipes for motivating the completion of this work. I would like to thank my second advisor, Seb Oliver, for believing in my application as a remote student and making my case to the University of Sussex. I am also greatly thankful to the administrative staffof the school of mathematics and physical sciences, in particular, to Richard Chambers, who at numerous occasions resolved administrative issues, which arose from my remoteness.

This research will not be complete without the help of my collaborators. Garrelt Mellema has guided me through the concepts as a hands-on teacher, elucidating either through codes or by examples. I am deeply thankful to Leon Koopmans who trusted my ambitious plans when many in his team did not. Leon has been a patient advisor and collaborator who motivated the large part of the radio astronomy component of this research. I am also indebted to him for introducing me to the mustard soup in Groningen. I highly recommend. While on the topic of radio astronomy, Oleg Smirnov's seminal work on the radio astronomy interferometry measurement equation (RIME) is part of the foundation of this work. I read his four papers on RIME, back-to-back like some engrossing novel. I was so mesmerized by the mathematical development that I did what I usually don't, I contacted him out of the blue asking him if he would be kind enough to collaborate in my work. He agreed without hesitation and invited me to South Africa where he provided me with the basic tools of RIME. I haven't looked back since. I am truly thankful to him

for his help and support.

When deciding the topic for the thesis, I had a Venn diagram in my head of three sets, namely, radio astronomy, cosmology, and high-performance computing. The 21-cm cosmology was the obvious intersection. The logical question to ask was - what would 21-cm cosmology tell us about the early Universe. Having spent five years, from 2004-2009, as a team member of the Joint Dark Energy Mission group at Berkeley, I grew interested in the nature of space-time and wondered if there was any commonality between the dark energy and inflation. This thought process spawned the third component of my research - exploring the nature of inflation using the 21-cm. To further develop this work, during my residency at Sussex in the fall of 2012, I knocked on Andrew Liddle's door and told him of my plan. He liked it and introduced me to another collaborator, Donough Regan. Donough has been a great collaborator and guide. I am grateful to his help and friendship. I also respect him for his excellent taste in beer. While at Sussex I also decided to sit in Andrew's class on General Relativity. I was taking a class in ages... since 1994. My two cents to all those who wish to learn general relativity, take Andrew's class. I am very thankful to Andrew for his encouragement and support. Andrew was also the source of limited entertainment I allowed myself while in residency at Sussex. The play Constellation that he took us to in London was an experience to be had. The best thing of all these collaborations is that along with the work partnerships, I have formed very good friendships with many, for which I am happy and thankful.

I was always interested in astronomy. However, making it a career choice only happened after I saw Carl Sagan's Cosmos and read the book that my mother gifted me. Growing up, my mother taught me math and my sister taught me science. My father made sure that my English was grammatically correct. Science and math, I managed, but the nuances of English grammar remain a challenge to this day. Seeking a path in astronomy in my birthplace of India was not a trivial task. Through various academic meanderings, one day, I met Dr. Govind Swarup, the father of radio astronomy in India. Since, Dr. Swarup has been the beacon of inspiration. I will always remain grateful to his resolute support, affection, and encouragement.

I am grateful to all my teachers, mentors, and collaborators, in particular, to Alain Bonissent. Alain has been a mentor and a friend. I am very thankful for his help and support at every opportunity.

I am also thankful to Horst Simon for believing in me and helping me wherever he could. His partnership and support has helped me to take longer leaps and think big.

I know that Don Backer would be happy to see this thesis. I thank him for all his support and encouragement when he was with us.

I am thankful to my ISAAC and ICCS teams. Their hard work, dedication, and partnership has resulted in a successful 4 year project and empowered so many young scientists whom we trained in parallel algorithms. Hsi Yu's exemplary work on AMR, Steve Hartung's image subtraction pipeline, and two-point correlation effort with Intel, along with all the awards we received or were nominated for, define the success of ISAAC.

Without my friends the journey would be pointless. I am thankful to all my friends who unconditionally supported my idea of PhD in my old age. I am very grateful to those who provided valuable insights during various discussions. I would like to thank, David Hawkins, Melvyn Wright, Vibor Jelic, Vishambhar Pandey, Panos Labropoulous, Yi Mao, Anson D'Aloiso, Paul Shapiro, Anand Sivaramakrishanan, Perry Greenfield, and Kevin Marvel. I would also like to thank Ludwig Schwardt for including me in his then small team of two who were brave enough to run MeqTrees on Mac OS X.

This thank you would be incomplete without acknowledging all my non-human friends, in particular, Stormy and Snowy who continue to lighten the moment by their never ending theatrics. Not to mention their adopted patron who without tiring takes care of them.

And to all my life's events, good or bad. A simple but persistent reminder that if I am happy today then all that has led me to this place - good and bad - is worth acknowledging.

Finally, I am profoundly grateful to my closely-knit and loving family. I grew up in a household where the importance and value of knowledge and education was inculcated at very early age. Every educational milestone was incentivized by a gift of an expensive fountain pen. It used to be a prestigious and proud moment to get one of those pens. This thesis will mean a lot to my parents. My parents always wanted me to finish my PhD. This work is dedicated to the fond memory of my father and to my proud mother and sister. Without their unconditional love, care, and inspiration this journey would not have been possible. With sincere regards,

Hemant Shukla (Berkeley, November 2014)

Contents

Part I

Scientific Goals and Theoretical Background

Chapter 1

Introduction

At the fundamental level, all the physical processes are the manifestation of the intricate interplay of matter and energy, the two interchangeable universal tangibles. To understand the interplay occurring in the farthest reaches of the Universe, we strain to collect the weak electro-magnetic radiation (light) arriving from afar. We detect this radiation in forms of continuous fields or discrete bundles. In the latter half of the nineteenth century, the phenomenon of light was shown by James Clerk Maxwell to be due to the undulating electric and magnetic fields carrying energy through space-time. Later the same continuous electromagnetic fields were detected as discrete energy bundles called photons by extending the works of Max Planck and Albert Einstein. Through the twentieth century, various mathematical frameworks have been developed to model the phenomenon of light in its dual forms. Many, yet futile, attempts have been made to reconcile this dual behavior. The manifestation of the phenomenon of light in either form lays the foundation of all the observational cosmology research. From the chemical footprints of the photons fossilized in the images taken from the 100 meter telescope on Mount Wilson, CA, in 1922-23 by Edwin Hubble *et al.*, to the weak radio waves permeating the Universe detected by the Planck satellite in 2013 located far away at the Earth-Sun L_2 point, it is the light that elucidates and defines our understanding of the Universe.

The very first photons that we observe are from the time when the Universe was about 380,000 years old after the Big Bang. Before this period, the Universe was an expanding and tightly coupled hot and dense plasma of electrons, protons, photons, and many other particles. In this state, the free moving electrons coupled with photons through Thomson

scattering and resulted in an opaque (short mean free path for photons) Universe. As the expansion adiabatically cooled the Universe, the electric forces between the electrons and protons became relevant and allowed the formation of neutral hydrogen. This triggered the transition phase, often called the recombination era of the Universe when the matter decoupled from radiation releasing the first photons in the transparent Universe. These photons have a blackbody spectrum and have cooled from 3000 K (infrared), since their release, to 2.7 K (microwave) in the present day and they form a background radiation called the cosmic microwave background (CMB) radiation. In the 1940-50s, many scientists predicted and reported the existence of near-isotropic background. It was not until 1964-65 that the team of Arno Penzias and Robert Wilson conclusively measured the CMB. The detailed study of these photons, since, has revolutionized the field of cosmology and established the concordant cosmology in the form of the Λ-CDM model, where Λ represents the dark energy component and CDM stands for the cold-dark matter. In essence, the *first light* has narrated an in-depth tale of the early Universe.

Between the release of the first photons and the formation of the large-scale structures, the history of the Universe is not well known. While not much has been directly observed, there are various hints in the CMB observations and other deep observational data that indicate yet another phase transition in the Universe. The CMB data, for example, indicates that after the decoupling of the CMB, photons and the neutral hydrogen evolved independently only for another 700,000 years. Thereafter, the CMB photons again coupled with the electrons through Thomson scattering around one billion year after the Big Bang. The relevant question to ask is that where did the electrons come from? Especially in the expanding and therefore cooling Universe, conducive to the formation of neutral hydrogen. Based upon the observed large-scale structures, one could reasonably extrapolate that after the decoupling, the neutral hydrogen assembled in the intricate network of gravitational potentials due to the primordial (of quantum mechanical origins) density perturbations in the smooth dark matter and matter density fields. The gravitational collapse eventually led to the formation of the bodies capable of producing the ionizing photons giving rise to the ionized medium rich with free electrons. It takes 13.6 eV to ionize a hydrogen atom. This energy is equivalent to that of an ultraviolet photon. It is unclear what objects were responsible for the ionization of the intervening neutral hydrogen. However,

in various scenarios studied, the objects capable of releasing such energy could be early massive stars or black holes. The period in the history of the Universe from the decoupling until the formation of the first ionizing sources is called the Dark Ages. Thereafter, the Epoch of Reionization commences and ends around redshift $z = 6$, when all the permeating hydrogen is fully ionized. This permeating hydrogen, depending when it is referred to, is the pre-galactic (prior to the formation of galaxies) or the inter-galactic medium. To directly observe the Dark Ages (DA) and the Epoch of Reionization (EoR) makes a compelling case for the next generation of experiments.

The Second Light

But without the stars how do we observe in the dark? Our biases continue to precede our best of objective intentions. As humans, in general, we are optical light chauvinists because most of us 'see' in the narrow optical part of the otherwise extremely wide electromagnetic radiation spectrum. If we had evolved to 'see' in radio, perhaps we would have 'seen' the afterglow of the Big Bang all around us much early in the civilizational history.

The electromagnetic spectrum spreads far beyond either side of the visible light frequencies/wavelengths. Therefore, what is dark in the visible may not be so in other parts of the spectrum. As early as the 1930s, in the days of infancy of radio astronomy, it was known and later observed, in 1951 by Harold I. Ewen and Edwin M. Purcell, that the neutral hydrogen was 'visible' at rest frequency of 1420.4 MHz (21.1 cm) in the radio part of the electromagnetic spectrum.

The electron and the proton spin in the hydrogen atom split the 1s ground state in what is known as hyperfine structure. The energy between the states is very small, 5.901×10^{-6} eV. Compare this with the ground state energy of 13.6 eV. The higher energy state of the hyperfine structure is when the spins of the electron and the proton are parallel and lower when anti-parallel. This transition is spontaneous with the probability given by Einstein coefficient, $A_{10} = 2.85 \times 10^{-15}$ s^{-1}. The half-life of this radiation is roughly 1.1×10^7 years. However, a large amount of hydrogen in the universe compensates for the low probability and makes 21-cm photons very good tracer of neutral hydrogen. In addition, the small energy needed to flip the spins of the electron and proton was readily facilitated

by the CMB photons and the collisions between the hydrogen atoms. As a result, during the Dark Ages the neutral hydrogen glows in the 21-cm. The Dark Ages are not dark after all. After the CMB, a second ensemble of photons with wavelength of 21-cm were released in the Universe during the Dark Ages. The direct observation of these photons traces the underlying hydrogen. With the formation of the first ionizing sources, as the underlying neutral hydrogen is ionized, this radiation will fluctuate and subside across a redshift range constraining the ionization sources. Thus, for a large part of the duration of the Dark Ages and the Epoch of Reionization ranging from redshifts $z = 1000$ - 6, the 21-cm is observable in redshifted radio wavelengths of 210 - 1.5 m (1.41 - 200 MHz). See section §3.1 for the details on when the 21-cm is observable in absorption, emission, or not at all.

The next generation of radio telescopes are developed to further study the Universe through the narration of the *second light* of the neutral hydrogen. The CMB depicts only one epoch when the matter and radiation decoupled. The 21-cm radiation spans 700,000 years of evolutionary history of the early Universe. This will allow to map the three dimensional evolution of the ionization history of the Universe thus revealing the underlying physics. The stronger ionizing sources will burn out the intervening hydrogen much faster than the weaker ones. The fluctuation in the 21-cm photons will also trace the growth of the primordial anisotropies that took root to grow into the large-scale structures. Finally, the very first detection of the *second light* has the potential of revealing the processes and phenomena utterly unknown. For in depth pedagogical review of the 21-cm cosmology refer to Furlanetto et al. [2006] and Pritchard and Loeb [2012].

1.1 Frontiers of Precision Cosmology

At the writing of this thesis, the ΛCDM cosmological concordant model, based upon the Planck observational data [Planck Collaboration et al., 2013], states that the observable Universe today is 13.81 ± 0.05 Gyr old, geometrically flat, and expanding at a rate of 67.3 km s^{-1} Mpc^{-1}, and made up of three primary constituents - dark energy (68.3%), dark matter (26.8%), baryonic matter (4.9%), and neutrinos ($\ll 1\%$).

While many experiments have indirectly measured the amount of dark matter and dark energy in the Universe without the direct knowledge of their nature and composition, one of the essential pillars of the concordant model that remains largely unconfirmed observationally is the phase transition of the Universe at Planck scales (length $\sim 10^{-31}$ m, time $\sim 10^{-44}$ s), termed as inflation. Briefly, inflation explains away the lingering problems of the smoothness, flatness, and deficiency of exotic particles in the hot Big Bang model by introducing superluminal expansion of the Universe when its size and age were at the Planck scale. At these scales the quantum gravitational effects become relevant therefore motivating in depth inquiry. Scientists, Erast Gliner and Andrei Sakharov, suggested the precursor concepts of the exponential expansion of the Universe; however, Alan Guth, who also coined the term inflation in 1980, independently developed the idea.

Inflation solves the flatness and smoothness problems in the Big Bang model by stretching the geometry towards a flat curvature ($\Omega_k = 1$) and driving the causally related regions to non-causal locations (CMB differential$\Delta\ T/T \sim 10^{-5}$). Soon after the introduction of inflation, it became evident that besides explaining the original puzzles, the paradigm also forms the basis for explaining the origins of the cosmological principle of a homogeneous and isotropic Universe. More importantly, however, inflation predicts the formation of the observed large-scale structures as the consequence of the growth of the primordial quantum mechanical perturbations. These perturbations are Gaussian and adiabatic, *i.e.*, the fractional over and under densities in matter and energy are the same. The spatial power spectrum, also known as the Harrison-Zel'dovich spectrum, of these fluctuations is scale-invariant and is described by a power law. The inflationary paradigm predicts that the spectral index, $n_{\rm s}$, of this power spectrum is not exactly one, as expected for the scale-invariant (flat spectrum) case. For example, in the inflationary model with slow roll potential, the spectrum is expected to vary very slowly and that $|n_{\rm s} - 1| \ll 1$ [Lyth and Riotto, 1999]. The recent Planck measurement combined with the independent weak lensing results yield $n_{\rm s} = 0.9603 \pm 0.0073$ [Planck Collaboration et al., 2013].

The high precision observations of the thermal anisotropy sizes in the CMB, the flat curvature ($\Omega_k = 1$), and spectral index are strong indicators of the inflation paradigm. However, a class of competing models explains the inflationary phase requiring tests that

are more rigorous. The potential of the scalar field that drives the inflation classify the competing models into three categories, namely, weak field, strong field, and hybrid. One mechanism of differentiating between the models is to test for primordial non-Gaussianity in CMB. The primordial non-Gaussianity is related to the higher-order statistics of the CMB, namely the bispectrum. The bispectrum is defined by two parameters that are, the dimensionless non-linearity parameter $f_{\rm NL}$ that measures the amplitude, and the associated function that measures the shape of the bispectrum. The 1-σ Planck measurements of the local $f_{\rm NL}^{\rm loc} = 2.7 \pm 5.8$. This result along with related analyses in Planck Collaboration et al. [2013] support the originally proposed single-field slow-roll inflation model. However, the results are not conclusive and motivate further studies. In this research, we examine the non-Gaussianity by measuring the bispectrum of the 21-cm radiation from the Dark Ages and the Epoch of Reionization.

Another mechanism to categorically test for inflation is to measure the E- and B-modes of the polarization of CMB. The E- and B-mode encode the information of the gravitational wave generated during the inflationary epoch. The experiment titled BICEP-2 has announced in BICEP2 Collaboration et al. [2014] the detection of excess signal in B-mode at a specific angular scale. This is a significant result and direct detection of inflation. However, the results have been challenged since, with Planck results indicating that the excess may be attributed to the Galactic dust, [Planck Collaboration et al., 2014]. In addition, a joint study of BICEP-2 and Planck team has studied the same region of the sky and found string evidence of dust and not of B-modes, [Ade et al., 2015].

The in depth research of CMB has strengthened and established the concordant model. The future studies in the CMB polarization promise further insights into the primordial physics and initial conditions at quantum scales unexplored in particle-physics experiments. The detection of 21-cm signal from the Dark Ages and EoR will further revolutionize the field of cosmology. The 21-cm research provides complementary results to the established cosmological concordant model. In comparison to the CMB that is projected on the sky, the redshifted 21-cm data will cover multi epochs (using 21-cm tomography) revealing the evolution and growth of the structure. The emerging radio telescope arrays are poised to detect the 21-cm signal and promise a great new era for

cosmology.

1.2 Current and Future Telescopes and the Challenges

Current radio interferometers, *e.g.*, Giant Metre-wave Radio Telescope (GMRT) [Paciga et al., 2011], Low Frequency Array (LOFAR) [Harker et al., 2010], Murchison Widefield Array (MWA) [Lonsdale et al., 2009], PAPER [Parsons et al., 2010], etc, are poised to detect neutral hydrogen as fluctuations in the brightness temperature during the EoR. These observations are statistical in nature and yield matter power-spectra as a function of redshift. The signal is expected to be weak (five orders of magnitude below the foreground noise) and buried under poorly understood effects including the foregrounds, ionosphere, polarization, instrumental stability, and radio frequency interference (RFI). In order to make a successful detection it is imperative to assess the level of influence these effects will have on the signal for the current as well as future instruments, *e.g.*, Square Kilometre Array (SKA) and Hydrogen Epoch of Reionization Array (HERA). These arrays may have sensitivities to directly image the H II regions.

The LOFAR array dedicated to the EoR research is currently at the most advanced stages of the data acquisition and processing. Following is a brief review of the telescope and the associated challenges to gain the insight into the 21-cm experiments. This design is a prototypical layout for the upcoming telescope. While LOFAR is not an official precursor or pathfinder to SKA or HERA, the collective knowledge-base developed will form the foundation of the future DA and EoR experiments.

The LOFAR telescope array [van Haarlem et al., 2013] is a hybrid multi-configuration telescope with a densely populated core and sparsely distributed antennas to provide longer baselines for higher resolution. The antennas are not typical parabolic dishes that are traditionally electro-mechanically steerable. The antennas of LOFAR are termed as stations that are massive ensemble of fixed dipole antennas with wide field-of-view. Each station has set of dipole antennas sensitive to two broadband for frequencies entitled, low-band antennas (10-90 MHz) and high-band antennas (110-250 MHz). This corresponds to the range of redshifted neutral hydrogen ranging from of $z \sim 5 - 150$. From the epoch when the Universe was roughly 9 million years old to about a billion year old covering

Figure 1.1: The aerial view of the central LOFAR core. The stations are the dark grey tiles. The image shows 16 stations. [van Haarlem et al., 2013]

almost 8.5% of the early age of the Universe. There are 48 LOFAR stations spread across the norther Europe. The core with 40 stations are distributed in 180 km area in centered in the Dutch town of Exloo. The Figure 1.1 shows the central part of the core. The typical station near the core have 48 dual-polarized or 96 single-polarized dipole antennas. Signal from the dipoles is correlated to synthesize the interferometric aperture. The tracking and pointing of the LOFAR array is achieved by beam-forming. The beam-forming is a signal processing technique where the phases of the signals from different antennas are weighted (temporally shifted) in order to increase the sensitivity in a specific direction. The analog signal received at the dipoles is filtered, amplified, converted to intermediate frequency, and digitized. The signal is then divided in sub-bands using polyphase filter banks (better alternative to Fast Fourier Transform for channel sub-division) and prepared for correlation. The sub-bands for LOFAR are 156 or 195 kHz wide leading to 244 channels foe 48 MHz bandwidth per polarization. The computational loads vary but LOFAR science dat products are of the order of 5 PB per year.

The SKA Low-1 configuration is also a dipole antenna based array. However, it will be built with the receiver technologies from 5 years in the future that provide much higher

sensitivity (almost 100 times more than the current state-of-the-art). The Figure 1.2 shows the artists impression of the SKA Low 1 array designed for the low frequency research geared towards DA and EoR observations. This figure also shows the dipole antennas that will be spread out to yield roughly 5 square kilometer collecting area.

Figure 1.2: Artist's impression of the low frequency portion of the Square Kilometre Array (SKA-Low) to be constructed in western Australia in the latter part of 2017. The array will have 250,000 of the dipole antennas. [Image Courtesy: SKA website and as listed - Swinburne Astronomy Productions/ICRAR/U. Cambridge/ASTRON.]

The challenges to the signal detection are manifold and are categorized as the propagation effects that are cosmological/astrophysical, atmospheric, terrestrial and instrumental. Another set of challenges stem from the unprecedented computational loads. The data rates from LOFAR are in the Petascale (10^{15}) range while for SKA they will scale by three orders of magnitude to Exascale (10^{18}). For the successful detection of the redshifted 21-cm signal, in depth understanding of the propagation effects and their removal is critical. Also critical is the concerted effort by the radio astronomy community to develop standardized and scalable software solutions that could process the data rates of the future.

The extragalactic and Galactic foregrounds define the cosmological and astrophysical effects. These foreground ($> 10^3 - 10^4$ K) peak above the 21-cm redshifted signal (10 - 100 mK) in the frequency ranges of interest in the range of 100-200 MHz. The extragalactic foreground is primarily generated by the bright active active galactic nuclei (AGN), or in the sub-mJy range, by the supernova remnants in the star forming galaxies. The Galactic foreground, as the name suggests, originates from the Milky Way and is diffuse in nature. Various physical processes contribute to the foreground. The largest contribution is due the Galactic synchrotron radiation Shaver et al. [1999]. The AGNs also emit synchrotron radiation. The remainder of the foreground comes from the free-free (Bremsstrahlung)

emission. Many techniques are developed for the subtraction of the foregrounds with varying levels of accuracy, see, for example, Chapman et al. [2012], Morales et al. [2006].

The effects due to the ionosphere originate at the upper layers of the Earths atmosphere, which is ionized by the Sun. These effects manifest as the phase and amplitude fluctuations [Hewish, 1951, 1952] in the incoming electro-magnetic wavefront and are proportional to the frequency as $\propto \nu^{-2}$, therefore are significant for low-frequency radio astronomy. In addition, the large fields-of-view $(5-10^{\circ})$ of the LOFAR and SKA-class telescopes [Cohen and Röttgering, 2009] make the measurements more susceptible to the larger volumes of the ionosphere. The ionosphere effects attenuate the 21-cm signal through refraction and rotational polarization. The ionosphere effect results in a spatially varying point-spread response (beam) across the field of view [Koopmans, 2010]. The ionosphere effects are removed form the signal by ionosphere calibration. The 3D structure of the ionosphere is modeled and the calibration solution is applied to the measurements. Techniques such as A-Projection [Tasse et al., 2013] are implemented to mitigate the ionosphere and similar direction dependent effects.

The radio frequency interference (RFI) is another source of noise in low-frequency radio astronomy that limits the performance of the instrument. The primary sources of this noise are human applications (telecommunications, microwave, power grids) in the available and adjoining radio spectrum of interest. The RFI appear as correlated spurious data and therefore hard to remove. A wide variety of techniques, including fast data integration at nano- to milli-second scales [Baan et al., 2004, Bhat et al., 2005, Winkel et al., 2007], statistical variance [Fridman, 2008], fringe-stop pattern recognition [Athreya, 2009], and highly efficient post-correlation auto-flagging methods [Offringa et al., 2010a,b], have been implemented and used for the excision of the RFI. The recent results from LOFAR RFI pipeline indicate that the techniques developed by Offringa et al. [2010a] successfully excise the RFI from 95% of the data.

The signal is corrupted by the instrument itself. The source of this noise are thermal noise introduced by the receiver, pointing errors that manifest as gain errors, confusion noise due to multiple sources within synthesized beam, side-lobe noise from extended sources,

moving bright object, and deconvolution noise. All these errors either are additive or multiplicative in nature in the uv-plane. Most of these errors are week understood and are minimized through standard techniques such as calibration, increased integration time, and post processing.

As it is evident, the detection of 21-cm is a daunting task fraught with sources of errors. Therefore, in the absence of observational data, it is crucial to conduct studies employing realistic simulations. The output of the realistic simulations are expected datasets that include all known physical as well as instrumental effects. Thereafter, various data extraction techniques may be tested against the datasets by comparing the input model parameters with the recovered model parameters to further fine-tune for optimization. The simulation of realistic datasets requires developing real case parametric pipeline that will generate EoR simulations, together with foreground simulations, RFI, ionosphere and instrumental effects (i.e. polarization, directionally-dependent gain variations). The pipeline will help assess the optimal array configuration (*i.e.* uv-coverage), field-of-view (FoV), frequency range, etc. and quality of the recovered the parameters of interest. In addition, the pipeline will be able to explore systematics for variety of configurations of radio interferometers and search for global optimum for science cases within the large parametric phase-space. The following chapters focus on the development of such a simulation methodology and testing its efficacy by closely examining the propagation effects and techniques of extracting the redshifted 21-cm signal.

The final challenge is data rates. In brief, the larger telescopes are generating massive amounts of data that is breaking the traditional computational approaches. The biggest challenge is of keeping up with the rapidly changing computing industry. The next generation of compute architectures is introducing massive parallelism via manycores and accelerator based (graphics processing units (GPUs)) compute modules accessible only through newer programming models such as OpenMP, CUDA, OpenCL, and for multi-nodes, Message Passing Interface (MPI). The adoption of massively parallel computing is rife with challenges of its own. Note that the commercial market forces, video games, animation, etc., drive the computing industry, upon which the entire scientific computing depends. As a result scientific community is left to the constantly align with the changing

paradigm. If not designed judiciously, scientific computing projects run the risk of vendor-locking and short lifespan. For example, the advent of GPU computing in 2005-2006, AMD was the leader and introduced a relatively simple language named Brook and Brook+. Applications developed in Brook demonstrated never seen before speed-ups thereby changing the nature of the research. However, for reasons better known to AMD, they faded the language by 2007 leaving the applications to be rewritten in the next flavor of programming model. The scientific community pays a heavy price while playing catch-up and therefore it is imperative to architect standardized and modular software eco-systems that can sustain the market pressures and sudden upheavals. Form 2010 through 2014, I have conceived and led a National Science Foundation a first of its kind project entitled Infrastructure for Astrophysics Applications Computing (ISAAC), see Shukla [2010-2014], that explores the phase-space of high-performance computing (HPC) with these emerging architectures and programming models as applied to Astrophysics.

1.3 Numerical Simulations as the Third Pillar of Science

> *The simulacrum is never what hides the truth - it is truth that hides the fact that there is none. The simulacrum is true.*
>
> *- Ecclesiastes*
> *in Simulacra and Simulation by Jean Baurdillard*

The advancement in high-performance computing (HPC) has pushed the boundaries of simulations in science and engineering. From the simulations of the interactions of quarks and gluons using quantum chromodynamics (QCD) to the large-scale structures in the Universe, the simulations have enabled the scientific process and knowledge. Combined with experimental and observational data, simulations have helped in exploring reality in ways beyond the capacity of experiments.

With the advent of massively parallel computational architectures, the HPC has grown from terascale (10^{12}) to petascale (10^{15}) in just 15 years. The architectures of the processors have become massively parallel. The next logical milestone is the exascale (10^{18}). These milestones have enhanced the capabilities of scientific discovery by manifolds. However, the milestones also usher technological disruptions. Harnessing latest

technology leads to expensive and time-consuming rewrite of the established codebases. The introduction of accelerator based computing, while highly effective for massive parallelism, requires significant changes to the existing solutions. However, the new architectures also provide opportunities to implement novel solutions. For example, the new hierarchical memory and massive compute bandwidths of accelerators allow the development of otherwise prohibitive numerical techniques leading to a complete overhaul of applications. It is quite evident that there are serious pros and cons to be weighed when considering the adoption of the new technologies. While the cons seem to be the hurdle of rewrite and the steep learning curves for the new programming models, the benefits of the massively parallel systems are many. The commonly used algorithm such as the FFT when run on GPUs yields a performance gain of upto 10× for CUDA FFT (cuFFT) on NVIDA Tesla and Kepler class of GPUs. Similarly, cuBLAS performs 5× to 17× faster than the state-of-the-art. The growing support for scientific libraries and ease of use of the programming language is making CUDA a viable solution for parallel programming.

The combination of changing paradigm of the HPC has nudged the simulations into shouldering the scientific process as the third pillar after the observation and modeling. The sheer compute power allows accurate simulations to test models that best fit the observations. More importantly, however, the simulations are best used for making predictions. One of the most important aspect simulations is the freedom to reverse the direction of time. In cosmology, this is of significant value as it provide exploration of various initial conditions in the past that could lead to the present observational data. In scientific domains, where there is no past data or experimental recourse, for example climate science, various models provide insights into the complex physical processes as they evolve over time and lead to present day scenarios. Highly accurate simulations allow for rigorous testing before production. This procedure is extremely useful in case the production costs are steep. Simulations are used to optimizations, complex visualization, Monte Carlo instances, studying phenomenon beyond the scope of experiments, and the list goes on. The simulations have become far more advanced with the growth of computational power.

The next big change in the computational growth is the impending exascale milestone.

SKA-class telescopes are poised to generate data in the Exabyte range. The current tools for data acquisition, process, and archiving will require in depth reviews and overhaul. Scaling to exascale computing is a non-trivial task specially because the computation industry upon which the scientific communities depend is not fully prepared to meet the challenge. There are various roadmaps but none reach the goal without disruption. The primary challenge in the road to exascale is the power consumption of the compute devices. At the writing of this thesis, the state-of-the-art, ranked number 1 *greenest* supercomputer was the Tsuambe system at the Tokyo Institute of Technology, running at 4.38 GFLOPS/W. This is a homogeneous system running Intel Xeon and NVIDIA K20x processors. If we were to scale this system to reach exascale, it will require 2×10^8 Watts to run. That is equivalent to a small nuclear plant. This is cost prohibitive and impractical and therefore will require a new approach from the industry. The high-efficiency and low power architectures will emerge in the market place as needed. Even if the industry responds and develops architectures to meet the requirements, the underlying programming models will dictate a redesign of the software ecosystem. Until then we make the best use of the technologies available. The simulation codes used in this research are hybrid and employ OpenMP, MPI, and multi-threaded approach and run on large supercomputing clusters.

The supercomputing facilities used for this research are, University of Portsmouth (Sciama), University of Sussex, Texas Advanced Computing Center, and National Energy Research Supercomputing Center.

1.4 Thesis Overview

The goal of this research is to develop realistic simulations of the EoR models for a wide range of redshifts and study the simulated observational output using realistic radio telescope models including propagations effects. While we focus on the SKA-class telescope the LOFAR configuration is used for validation. This work develops the end-to-end pipeline to simulate the cosmological signal and models visibilities as observed with different radio telescope configurations. The propagation effects due to intervening cosmological & astrophysical phenomenon, ionosphere, and instrumentation are added to the path in the simulation. The end-to-end pipeline entitled, Simulation the Interferometry

Measurements (SIM), incorporates three primary codes, namely, CubeP^{3}M, C^2-Ray, and MeqTrees, stitching them together with additional middleware for seamless data flow. The details of SIM are discussed in the Part II of the thesis. Various studies are conducted with the telescope layout and results are discussed in Part III of the thesis. In addition, the effect of Lyman-Limit Systems to the EoR signal, and feasibility of extracting primordial non-Gaussianity with the 21-cm observations is also discussed in Part III. The research has completed the following,

(i) Build the end-to-end pipeline entitled SIM by consolidating CubeP^{3}M, C^2-Ray, and MeqTrees with a middleware.

(ii) To test the efficacy of the SIM and the visibility processing, defined three applications addressing instrumentation issues of SKA-class telescopes, examine the effects of Lyman-limit systems on the reionization epoch, and build a prototype methodology for extracting primordial non-Gaussianity parameter $f_{\rm NL}$ from the 21-cm observations.

(iii) The instrumentation effects explore the effects of the size of the array, quality of foreground sky-models for calibration, thermal noise limits with integration time, weighting schemes.

(iv) Developed a new image metric for measuring the performance geared for EoR research called Spherical Averaged Spatial Spectrum (SASS).

((v)) Simulated three separate models of $114{\rm h}^{-1}$ Mpc volume datasets to explore the morphology of the H II regions and the effects on the observable in the presence of the Lyman-limit systems.

(vi) Developed a prototype of extracting primordial non-Gaussianity with higher order statistics of bispectrum.

Chapter 2

Cosmology

In the past decade, cosmology has been referred to as "precision cosmology" because of its transition from the data starved to the data driven science. The abundance of the observational data has allowed for the constraining of parameters of the cosmological model, called the lambda cold dark matter model (ΛCDM) to a high level of accuracy. The ΛCDM model builds upon the inflationary cold dark matter Big Bang framework by incorporating the dark energy. The observational data from the satellite, high-altitude, and ground-based experiments, covering cosmic microwave background to the large-scale structures, have helped expand the understanding of the fundamental principles defining the early Universe and its evolution, while increasing the accuracy of the estimation of the model parameters. The ΛCDM model is defined by eight parameters, namely, age of the Universe, Hubble's constant, baryon density, dark matter density, dark energy density, scalar spectral index, density fluctuation at 8 h^{-1} Mpc , and the reionization optical depth. The most recent results for these parameters from the Planck satellite are shown in the Table 2.1.

This chapter gives an overview of cosmology relevant to this research. The chapter provides a review of the ΛCDM cosmology with basic formalism. Thereafter, the chapter explores the inflationary stage followed by the dark ages and the epoch of reionization.

2.1 The Cosmic Prelude

The introduction of general relativity in 1916 by Albert Einstein established a solid foundation upon which the future cosmology would be built. The theory redefined

Parameter	Symbol	Planck (2013) 1-σ
Age	t_0 [years]	$13.813 \times 10^9 \pm 0.058$
Hubble's constant	H_0 [km s^{-1}/Mpc]	67.4 ± 1.4
Physical baryon densityΩ	$_bh^2$	0.02207 ± 0.00033
Physical dark matter densityΩ	$_ch^2$	0.1196 ± 0.0031
Dark energy densityΩ	$_\Lambda$	0.686 ± 0.020
Density fluctuations at 8	σ_8[h^{-1} Mpc]	0.834 ± 0.027
Scalar spectral index	n_s	0.9616 ± 0.0094
Reionization optical depth	τ_{es}	0.097 ± 0.038

Table 2.1: Cosmological parameters from the Planck results, [Planck Collaboration et al., 2013].

gravity as a manifestation of the curving of space-time due to matter and/or energy. In 1927, a Belgian priest, Georges Lemaître, extended the rigorous mathematical framework of general relativity to the Universe and deduced that the Universe must be expanding, [Lemaître, 1927]. Later in 1931, Lemaître called this as the "primeval atom" or the "cosmic egg" from which the Universe bagan, [Lemaître, 1931]. The observational evidence for the expanding Universe was independently established in 1929 by Edwin P. Hubble, see [Hubble, 1929]. Using the redshifts of the galaxies, Hubble estimated the linear relationship of the receding velocities of the galaxies and their distances with the proportionality constant known after him as the Hubble's constant. This initial effort lay the foundation of the Big Bang model of the Universe.

In 1948, George Gamow estimated that the current temperature from such a Big Bang relic would be 50 K, which over the decade he readjusted to 6 K. The argument made was that the expansion of the Universe would lead to the cooling of the initial radiation to few Kelvins. Similar estimations were made by Gamow's student Ralph Alpher and Robert Herman. In 1965, Arno A. Penzias, and Robert W. Wilson measured an excess antenna temperature of 3 K attributed to the Big Bang relic, and termed as the cosmic background radiation (CMB), [Penzias and Wilson, 1965]. The radiation was thermal with a black body spectrum. This was the first proof for the fiery beginnings of the Universe. However, the homogeneity and the smooth nature of the CMB did not add up to the current inhomogeneity (planets, stars, galaxies) seen in the Universe. Rashid Sunyaev,

in 1978, estimated that the CMB must have anisotropies, due to quantum fluctuations in the primordial plasma, of the order of 10^{-4} - 10^{-5} to lead to the formation of the structure of the Universe, [Sunyaev, 1978]. These anisotropies were confirmed by COBE experiment in 1990 and over the last two decades have been mapped with very high resolution. Three primary unexplained problems in the Big Bang model continued to challenge it. The problems were termed as the horizon problem, the flatness problem, and the monopole problem. In the next section, these problems are discussed in detail. In essence, however, all these problems arose from the disconnect between the initial and the present state of the Universe. For the Universe to be at the current state, the initial conditions had to be extremely fine-tuned. In 1980, Alan Guth [Guth, 1981], proposed a radical theory that resolved all these problems. He proposed that the Universe went through an exponential growth, faster than the speed of light (space-time can expand faster than the speed of light without violating the postulates of the Special Relativity) when it was 10^{-36} s old to about when it was 10^{-32} s. He called this period as the cosmological inflation. The inflation smoothes out the anisotropies and flattens the space-time. The very first evidence for inflation was reported by the BICEP-2 experiment measuring the predicted polarization imprint in the CMB due to gravitational waves generated during the inflationary phase, [BICEP2 Collaboration et al., 2014]. These results have been challenged since and attributed to the Galactic dust, [Ade et al., 2015, Planck Collaboration et al., 2014]. However, this almost century long roadmap of relentless exploration and sporadic discoveries continues to define and hone the ΛCDM cosmological model.

In this well understood picture, the Universe goes through an exponential growth period and then continues to expand. At the age of 380,000 years, the Universe cools enough for the formation of atomic hydrogen and consequential release of the otherwise coupled CMB photons. This period is called the Recombination. The period between the Recombination and the formation of the first stars is unknown. It is assumed that during this period the scaffoldings of the baryonic large-scale structures were formed by the dark matter halos. The period up to 380 million years since the Big Bang is termed as the Dark Ages (DA) when no stars were formed. This period was dominated by the photons emitted from the CMB and the 21-cm neutral hydrogen hyperfine spectral line. The discovery of the most distant galaxy (at the writing of this thesis), UDFj-39546284, at 380 million years since

Big Bang puts the upper limit to the DA, [Bouwens et al., 2011]. Following the formation of the first sources, the neutral hydrogen in the inter pre-galactic medium started to ionize. This period continued for a billion years and is known as the Epoch of Reionization (EoR). The evidence of this reionization is seen in the Thomson scattering of the CMB photons with the free electrons in the inter-galactic medium and also in the Gunn-Peterson troughs visible in the quasar spectra.

2.2 Friedmann Lemaître Robertson Walker metric

There are various advanced resources that cover the derivations, proofs, and detailed explanations of general relativity and its applications to cosmology, see [Chow, 2008, Liddle, 2003, Misner et al., 1973, Schutz, 2009]. This section outlines the basic ideas relevant to this research without providing the proofs. The reader is referred to the cited literature for detailed review.

In the formalism of general relativity, the metric is the most fundamental property and it defines the distance between two points in a space-time of a certain geometry. In the case of Cartesian coordinates, for example, the nearby distance between two points located at (x_1, y_1) and (x_2, y_2) is given as,

$$\Delta s^2 = (x_2 - x_1)^2 + (y_2 - y_1)^2$$

For a uniformly expanding coordinate system the above equation could be decoupled from the time factor of expansion and represented in what is known as comoving coordinates given by,

$$\Delta s^2 = a^2(t)\ [(x_2 - x_1)^2 + (y_2 - y_1)^2]$$

where, $a(t)$ is called the *scale factor* that measures the expansion rate of the coordinate system and has the units of length.

The above description is extended to describe a 4-dimensional (3 spatial and 1 time coordinate) metric for space-time with curved geometry that allows for expansion or contraction of space with time. In addition, the metric is homogenous and isotropic. One such metric is the the Friedmann Lemaître Robertson Walker (FLRW) 4-dimensional

metric described in time and spherical coordinate (t, r, θ, ϕ) as following,

$$ds^2 = -c^2\ dt^2 + a^2(t)\ \left[\frac{dr^2}{1-kr^2} + r^2(d\theta^2 + \sin^2\theta\ d\ \phi^2)\right] \tag{2.1}$$

where, $a(t)$ is the scale factor of the Universe, k is the curvature and takes the value, $0, -1,$ or 1, for flat, closed, or open geometry of space-time respectively.

2.3 Einstein's equation

Einstein's equation describes how matter curves the space-time and is defined as,

$$R^\mu_\nu - \frac{1}{2} g^\mu_\nu\ \mathcal{R} + g^\mu_\nu \Lambda = \frac{8\pi G}{c^4}\ T^\mu_\nu \tag{2.2}$$

The Ricci tensor R^μ_ν and Ricci scalar $\mathcal{R}$ give the curvature of space-time. The metric is defined by g^μ_ν. The Ricci tensor, scalar, and the metric define the space-time structure. The energy-momentum tensor T^μ_ν defines the matter content. The cosmological constant Λ is akin to the intrinsic energy density of the vacuum; positive value of which drives the acceleration of the Universe commonly known as the Dark Energy. The constants, G and c are Newton's gravitational constant and the speed of light respectively.

The energy-momentum tensor (also known as the stress-tensor) T^μ_ν, in a simplified form, is defined as an ideal fluid without viscosity or heat conductivity,

$$T^\mu_\nu = -p\delta^\mu_\nu + (p + \rho)u^\mu u_\nu \tag{2.3}$$

where, p and ρ are the pressure and energy-density of the fluid respectively, and u_μ is the covariant 4-velocity of the fluid that satisfies $u_\mu u^\mu = 1$.

Combining the FLRW metric in equation 2.1 with Einstein's equation and the energy-momentum tensor, yields the evolution of the scale factor and its relation with the curvature of the space-time. Einstein's equation 2.2 has rank-2 tensors leading to total of 10 partial differential equations. There are two independent Einstein's equations for the

FLRW. For the time-time case it is,

$$\left(\frac{\dot{a}}{a}\right)^2 + \frac{kc^2}{a^2} - \frac{\Lambda}{3} = \frac{8\pi G}{3}\,\rho \tag{2.4}$$

and for the space-space case it is,

$$\frac{\ddot{a}}{a} = -\frac{4\pi G}{3}\left(\rho + \frac{3p}{c^2}\right) + \frac{\Lambda}{3} \tag{2.5}$$

The equations 2.4 and 2.5 are known as the Friedmann's dynamical equations. It should be noted here that the scale factor $a(t)$ is related to the Hubble's constant $H(t)$ as, $H(t) = \dot{a}(t)/a(t)$. Assuming $\Lambda = 0$, the equation 2.4 in terms of $H(t)$ can be reorganized as,

$$\frac{k}{a^2} = \frac{8\pi G}{3c^2}\left(\rho - H(t)^2\frac{3}{8\pi G}\right) \tag{2.6}$$

This implies that the curvature $k = 0$ (flat Universe) if the energy density ρ takes a critical value of $\rho_c = H(t)^2/8\pi G$. Or $k > 0$ (closed Universe) for $\rho > \rho_c$, and $k < 0$ (open Universe) for $\rho < \rho_c$. Furthermore, the equation 2.4 is rearranged in separate density components as,

$$1 = \Omega_m + \Omega_k + \Omega_\Lambda \tag{2.7}$$

where,$\Omega_{\ m} = \rho/\rho_c$ is the matter density,$\Omega_{\ k} = -k/a^2H^2$ is the spatial curvature density, and$\Omega_{\ \Lambda} = \Lambda/3H^2$ is the Dark Energy density.

For the measured value of the Hubble's constant for the present time, $H_0 \sim 70$ km/s/Mpc the critical density $\rho_c \sim 10^{-26}$ kg/m^3. This is very low density and amounts to five hydrogen atoms per cubic meter.

2.4 Problems With The Big Bang Model

In the previous section it was shown that the general relativity framework provided great insights into the interdependence of the energy-matter and space-time. It was shown that the fate of the Universe - whether it will continue to expand (flat, open), or eventually collapse (closed) - is closely related to the energy-matter density. However, a close look reveals that the very equations highlight some of the challenges in the model as discussed below.

2.4.1 The Flatness Problem

As shown above, the geometry of the Universe takes different forms for the different values of the density$\Omega_m(t) = \rho/\rho_c$ parameter. The Universe starts out with a certain total density (matter and radiation) which deviates considerable from its original value as the Universe expands. The matter density (due to non-relativistic and pressure less matter) reduces by a factor of $1/a^3$, while the density of the radiation diminishes as $1/a^4$.

Rearranging the equation 2.7 yields,

$$\Omega_m + \Omega_\Lambda - 1 = |\Omega_{\text{Tot}}(t) - 1| = \frac{|k|}{a^2\ H^2} \tag{2.8}$$

For a flat Universe, $k = 0$, the density parameterΩ_{Tot} has to be 1 or $|\Omega_{\text{Tot}}(t)$ - $1| = 0$. Various observations, including recent Planck's observations measure $|\Omega_{\text{Tot}}$- $1| = 0.02$ for the present epoch. In other words the Universe has a very flat (Eucledian) geometry. Herein lies the problem. IfΩ_{Tot} is almost one today and we know that the density rapidly evolves as the Universe expands thenΩ_{Tot} must have started out extremely close to the present value to have maintained the current value despite the expansion. It may be estimated as to how closeΩ_{Tot} has to be to equal the value of one at the early stages of the Universe to reach the value of 0.02 in the present day. Following are the values ofΩ_{Tot} to reach the present day ($t_0 \sim 4 \times 10^{17}$ sec) value of 0.02 for different timelines [Liddle, 2003],

Decoupling ($t \sim 10^{13}$ sec):	$\lvert\Omega_{\text{Tot}}(t)$ - $1\rvert \leq 10^{-5}$
Matter-radiation equality ($t \sim 10^{12}$ sec):	$\lvert\Omega_{\text{Tot}}(t)$ - $1\rvert \leq 10^{-6}$
Nucleosynthesis ($t \sim 10^{1}$ sec):	$\lvert\Omega_{\text{Tot}}(t)$ - $1\rvert \leq 10^{-18}$
Electro-weak symmetry breaking ($t \sim 10^{-12}$ sec):	$\lvert\Omega_{\text{Tot}}(t)$ - $1\rvert \leq 10^{-30}$

These values indicate extremely high level of precision and fine-tuning required for the initial density value; quite antithetical to the natural phenomenon. This problem is termed as the flatness problem

2.4.2 The Horizon Problem

Closely related to the flatness problem is the horizon problem. First pointed out by W. Rindler in 1956, the problem is associated with the isotropy of the cosmic background radiation. The initial observations of the CMB show that the deviation from the isotropy is 1 part in 10,000 indicating that during the time of decoupling, the release of CMB, the background radiation was significantly uniform. Such uniformity implies thermal equilibrium which is indicative of causal contact. In other words, for the observed CMB isotropy to be possible, all the regions of the Universe should have been in thermal equilibrium (causal contact) during the time of the release of CMB radiation. For this to happen, the physical distance, D_{CMB}, between the two opposite regions should have been at least equal to the horizon distance D_{H}. The horizon distance is the distance the information travels between the opposite regions without violating the speed of light. In other words, during the time of the CMB emission, t_e, the ratio $D_{\mathrm{CMB}}(t_e)/D_{\mathrm{H}}(t_e)$ should be ≤ 1.

The ratio of the separation distance and the horizon distance is written as, [Brawer, 1995],

$$\frac{D_{\mathrm{CMB}}(t_e)}{D_{\mathrm{H}}(t_e)} = \frac{2\int_{t_0}^{t_e} \frac{c\ dt}{a(t)}}{\int_{0}^{t_e} \frac{c\ dt}{a(t)}} = 2\left(\left(\frac{t_o}{t_e}\right)^{1/3} - 1\right) \tag{2.9}$$

In terms of redshift the above is written as,

$$\frac{D_{\mathrm{CMB}}(t_e)}{D_{\mathrm{H}}(t_e)} = 2(\sqrt{(1+z)} - 1) \tag{2.10}$$

For the redshift when the CMB was released, $z = 1500$ the ratio is ~ 75. The physical size was much larger for the signal to have travelled to create the visible uniformity. This is known as the horizon problem.

2.4.3 The Magnetic Monopole Problem

While the hot Big Bang model is highly efficient in explaining the nucleosynthesis and abundances of the light elements, it fails to explain the various products that appear within the same framework at the stage of phase transition during spontaneous symmetry breaking [Albrecht and Steinhardt, 1982]. The theory predicts the creation of magnetic monopoles, domain wall, cosmic strings, textures etc. In fact, the superheavy monopoles,

should they exist, would constitute a major part of the energy density. However, none of these objects or topological defects have been observed. This is termed as the magnetic monopole problem.

2.5 Inflation

In 1981, in his attempt to solve the problem of the missing superheavy magnetic monopoles, Alan Guth was led to the theory of cosmological inflation. The inflationary hypothesis proposes that at the very early stages, from 10^{-36} s to 10^{-32} s, the Universe goes through exponential expansion. This expansion is superluminal (faster than the speed of light) and does not violate the light speed law as it is the space-time that expands. The rapid and massive expansion explains the big bang problems effectively. The initial curvature is flattened out due to expansion therefore negating the need for any fine-tuning forΩ_{Tot}. The sudden expansion also explains that the regions in causal contact were stretched farther apart creating the observed isotropy. The rapid expansion also dilutes the magnetic monopoles and thereby explains the absence of any observations. In addition, inflation also generates small density perturbations that over time lead to clumping of matter into large-scale structures of galaxies. The initial theory of inflation by Alan Guth (Guth [1981]) was further developed by Andre Linde (Linde [1982]). One of the predictions from Linde was that the inflation would generate gravitational waves that would impinge a signal in the polarization of the CMB.

Following is the brief development of the inflationary theory as taught by Leonard Susskind in the Stanford University Cosmology lecture series available online and Cosmology notes by A. Lewis [2012] of the University of Sussex.

The stress-energy tensor, see Equation 2.3, for a scalar field ϕ and potential $V(\phi)$, in its complete from, is written as,

$$T^{\mu}_{\nu} = g^{\mu\rho}\partial_{\rho}\phi\partial_{\nu}\phi - \delta^{\mu}_{\nu}\left(\frac{1}{2}\partial_{\rho}\phi\partial^{\rho}\phi - V\right) \tag{2.11}$$

For an isotropic and homogeneous Universe, the density, ρ, and pressure, P, are estimated from the stress-energy equations as,

$$T_0^0 = \rho \tag{2.12}$$

$$T_j^i = -P\delta_j^i, \qquad \text{where, } i, j = 1, ...3. \tag{2.13}$$

The stress-energy tensor encapsulates the matter in the Universe including radiation. The tensor in its matrix form is written as,

$$T_\nu^\mu = \begin{pmatrix} \rho & 0 & 0 & 0 \\ 0 & P & 0 & 0 \\ 0 & 0 & P & 0 \\ 0 & 0 & 0 & P \end{pmatrix} \tag{2.14}$$

We start out with the assumption that an FRW Universe, filled with a uniform scalar field ϕ, has the energy density per unit volume ρ defined as,

$$\rho = \frac{\dot{\phi}^2}{2} + V(\phi) \tag{2.15}$$

where $V(\phi)$ is the field potential energy and $\dot{\phi}^2/2$ is the field kinetic energy. The kinetic energy is the component associated with time. To estimate the equations of motion for the field of given energy density we apply the Euler-Lagrangian equation. The Lagrangian is defined as,

$$\mathcal{L} = \frac{\dot{\phi}^2}{2} - V(\phi) \tag{2.16}$$

and the energy density and pressure from the stress-tensor equation 2.11 are determined as,

$$\rho_\phi = \frac{1}{2}\dot{\phi}^2 + V(\phi) \tag{2.17}$$

$$P_\phi = \frac{1}{2}\dot{\phi}^2 - V(\phi) \tag{2.18}$$

For the time-invariant scalar field, the above relation is similar to the equations of dynamics for an ideal fluid with negative pressure,

$$\rho = -P \tag{2.19}$$

There are many potentials that could be used to define the scalar field. A simplest approach is used by defining a damped harmonic oscillator potential. This, in the literature, is widely referred to as a ball slowly rolling down the hill with friction. Inflation occurs when the field rolls extremely slowly. This potential is called the *slow-roll* inflation potential. The Figure 2.1 shows the schematic of the slow-roll inflationary model. During the time of the slow-roll for the field, the inflation occurs. The axes are exaggerated and are not to scale. Note that at 10^{-34} s the radius of the Universe is ~ 30 cm.

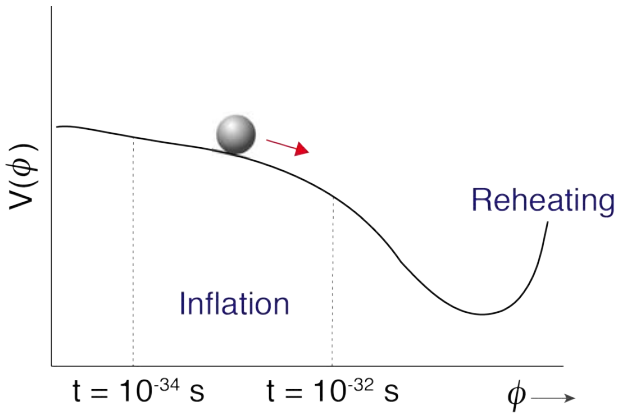

Figure 2.1: The schematic of the slow-roll inflation potential.

Recall that the Euler-Lagrangian equation is defined as,

$$\frac{\partial \mathcal{L}}{\partial \theta} = \frac{d}{dt}\frac{\partial \mathcal{L}}{\partial \dot{\theta}}$$

This implies that the Lagrangian for the field ϕ after differentiation is given as,

$$\ddot{\phi} = -\frac{\partial V(\phi)}{\partial \phi} = F(\phi) \tag{2.20}$$

where $F(\phi)$ is the force.

Now the total energy in the volume is E times the volume. For an expanding volume, like in the case of the Universe, the volume is defined by the scale factor $a(t)^3$. Thus, the

energy and the Lagrangian are defined as,

$$\rho = \left(\frac{\dot{\phi}^2}{2} + V(\phi) \right) a(t)^3 \tag{2.21}$$

$$\mathcal{L} = \left(\frac{\dot{\phi}^2}{2} - V(\phi) \right) a(t)^3 \tag{2.22}$$

The equations (2.21) and (2.22) define the mechanics of the scalar field ϕ. In terms of the scalar field the Lagrangian can be written as,

$$\begin{aligned} \frac{d}{dt} a(t)^3 \dot{\phi} &= -a(t)^3 \ \frac{\partial V(\phi)}{\partial \phi} \\ \implies a(t)^3 \ \ddot{\phi} + 3a(t)^2 \dot{a(t)} \ \dot{\phi} &= -a(t)^3 \ \frac{\partial V(\phi)}{\partial \phi} \\ \implies \ddot{\phi} + 3\dot{\phi} \ \frac{\dot{a}(t)}{a(t)} &= -\frac{\partial V(\phi)}{\partial \phi} \end{aligned} \tag{2.23}$$

where, $\dot{a}(t)/a(t)$ is H, the Hubble's constant. Using the equation (2.20) the above equation is then written as,

$$\ddot{\phi} + 3\dot{\phi} \ H(t) = F(\phi) \tag{2.24}$$

This equation is similar to the viscosity equation where the term $3\dot{\phi} \ H(t)$ is equivalent to the viscous force and is independent of the velocity. We may recall that the viscosity forces are zero on stationary objects and increase with the velocity. As we can see from the above relation, as the viscosity term $3\dot{\phi} \ H(t)$ increases and becomes equal to the force $F(\phi)$, the acceleration term $\ddot{\phi}$ becomes zero. In other words, there is no more acceleration. This implies that the terminal velocity is defined as,

$$\dot{\phi} = \frac{F(\phi)}{3H(t)} \tag{2.25}$$

This implies that the Hubble's constant term acts as a viscous force in the dynamics of the expanding Universe.

Now, let us recall the Friedmann's equation,

$$H^2 = \left(\frac{\dot{a}}{a} \right)^2 = \frac{8\pi G}{3} \rho \tag{2.26}$$

where, G is Newton's gravitational constant and ρ is the energy density. Using the equation (2.21) we can rewrite the Friedmann's equation as,

$$\left(\frac{\dot{a}}{a}\right)^2 = \frac{8\pi G}{3}\left(\frac{\dot{\phi}^2}{2} + V(\phi)\right) \tag{2.27}$$

Assuming a slowly decreasing potential with a very high potential energy, see figure 2.1, this is an assumption based on the premise that the viscous drag on the field is designed to keep the value of the field constant - the $\dot{\phi}$ term becomes very small (an analogous scenario is an object falling through an extremely dense liquid) - the Friedmann's equation is written as,

$$\left(\frac{\dot{a}}{a}\right)^2 = \frac{8\pi G}{3}\, V(\phi) \tag{2.28}$$

Since $V(\phi)$ is very slowly evolving, H becomes relatively constant. In other words,

$$\begin{aligned} \frac{\dot{a}}{a} &= H \\ \frac{da}{dt} &= Ha \\ a &= e^{Ht} \end{aligned} \tag{2.29}$$

That is, $t = H^{-1}$ is the time it takes for the Universe to expand e-folds. For the slow-roll potential it is estimated that the total number of e-folds are at least of the order of 60. For in depth estimation see, Peacock [1999].

It is important to note that while inflation explains the flatness, horizon, and magnetic monopole problems, it raises issues that threaten to render it ineffective. For example, the unique initial conditions that the inflation requires make it a far more unlikely scenario to occur. For detailed expert discussions see, Penrose [1989], Steinhardt et al. [2008], and Gibbons and Turok [2008]. In addition, there are alternatives to inflationary theory proposed such as by Linde [2003], Popławski [2010], and references therein.

2.6 Primordial Non-Gaussianity

As seen in the previous section, inflation adds to the hot Big Bang model by explaining the aforementioned problems. Especially, the large-scale structure formation that originated from the growth of the quantum fluctuations. The inflationary theory predicts that the

density perturbations are primordial, scale invariant, and Gaussian. The Gaussian nature of the perturbations is attributed to the single-field slow-roll inflation, as derived in the previous section. The Gaussian statistics is studied using the power spectrum of the CMB anisotropies, the primary source of data to study the physical processes in the early Universe. A wide range of inflationary models explain the same processes. The presence of any primordial non-Gaussianity will eliminate a large number of inflationary models. As the current observations indicate, the initial fluctuations were very close to Gaussian. Any non-Gaussianity will appear in the higher order statistics of the bispectrum and trispectrum that represent the skewness and kurtosis of the primordial perturbations.

The three statistical measures are defined as the Fourier transforms of the correlation functions. The Fourier transform of the two-point correlation function yields the power spectra, while the transform of the three- and four-point correlators provide the bi-and trispectra respectively.

For any field, for example a field of density fluctuations, $\delta(\mathbf{x}) = \delta\rho(\mathbf{x})/\bar{\rho}$, the Fourier transform as a function of the wave-number $\mathbf{k}$ is given as,

$$\delta(\mathbf{k}) = \int \delta(\mathbf{x})\ e^{-i\mathbf{k}\cdot\mathbf{x}}\ \mathrm{d}^3\mathbf{x} \tag{2.30}$$

The power spectrum, $P(\mathbf{k})$, is the square of the Fourier transform,

$$\langle\delta(k_1)\delta(k_2)\rangle = (2\pi)^3\delta^{\mathrm{D}}(k_1 - k_2)P(\mathbf{k}) \tag{2.31}$$

where, δ^{D} is the Dirac delta function. The power spectrum is also related to the two-point correlation function as,

$$\xi(\mathbf{x}) = \langle\delta(x_1)\delta(x_2)\rangle = \int \frac{\mathrm{d}^3\mathbf{k}}{(2\pi)^3}\ e^{i\mathbf{k}\cdot\mathbf{x}}P(\mathbf{k}) \tag{2.32}$$

where, $\mathbf{x} = x_2 - x_1$. Extending the definition of the power spectrum in 2.31 for the bi- and trispectrum we get the following relations,

$$\begin{aligned}
&\text{Power Spectrum} && \langle \delta\phi(\mathbf{k}_1)\delta\phi(\mathbf{k}_2)\rangle = (2\pi)^3\delta^{\mathrm{D}}(\mathbf{k}_1+\mathbf{k}_2)P_{\delta\phi}(k)\\
&\text{Bispectrum} && \langle \Phi(\mathbf{k}_1)\Phi(\mathbf{k}_2)\Phi(\mathbf{k}_3)\rangle = (2\pi)^3\delta^{\mathrm{D}}(\mathbf{k}_1+\mathbf{k}_2+\mathbf{k}_3)B_{\Phi}(k_1,k_2,k_3)\\
&\text{Trispectrum} && \langle \Phi(\mathbf{k}_1)\Phi(\mathbf{k}_2)\Phi(\mathbf{k}_3)\Phi(\mathbf{k}_4)\rangle = (2\pi)^3\delta^{\mathrm{D}}(\mathbf{k}_1+\mathbf{k}_2+\mathbf{k}_3+\mathbf{k}_4)T_{\Phi}(\mathbf{k}_1,\mathbf{k}_2,\mathbf{k}_3,\mathbf{k}_4)
\end{aligned} \tag{2.33}$$

Qualitatively, the power spectrum is the measure of the fluctuations (variance) of the field at different scales (spatial frequencies) per d$ln(k)$. The power spectrum provides the amplitudes at different Fourier components (spatial frequencies). However, there is no information of the phase which appears due to nonlinear processes. Higher order statistical methods such as the bispectrum easily capture that. The bispectrum measures the underlying nonlinearity in the form of the statistical dependence (coherent phase) between the three wave-numbers, [MacDonald, 1989].

In the homogeneous and isotropic model of the Universe, the wave-vectors representing the non-Gaussian component of the nonlinearity must satisfy the condition of the sum to be zero [Komatsu et al., 2009, Lewis, 2011]. This is evident in the definition of the bispectrum in the Equation 2.33. The delta-function ensures non-zero values for the bispectrum only when the sum of the wave-vectors is zero. This results in the vectors closing the loop and in flat space forming a triangular relationship. A pedagogical description of the triangles and their physical interpretation is give in Lewis [2011]. We describe the basic concept in the following paragraphs.

The three wave-vectors combine in three configurations, namely, equilateral ($k_1 = k_2 = k_3$), flattened ($k_1 = k_2 = k_3/2$), and squeezed ($k_2, k_3 \geq k_1$), see the Figure 2.2. Note that in all the three configurations for non-Gaussianity, the vector sum total is equal to zero. The sign of the bispectrum are indicative of the small regions of overdensity, if positive ($b > 0$), and underdensity, if negative ($b < 0$). In the physical world, the nonlinear density field of the large-scale structure will have a large component of the

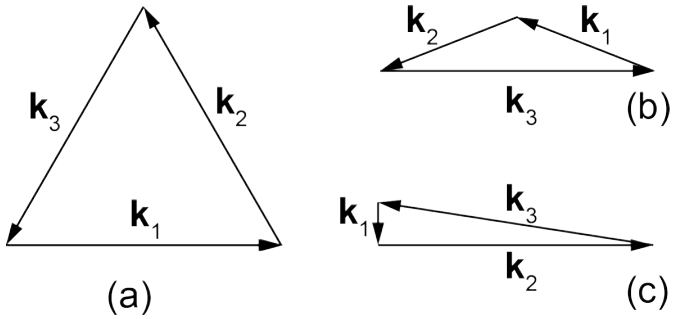

Figure 2.2: The wave-vectors for different shapes, (a) Equilateral, (b) Flattened, and (c) Squeezed.

equilateral configuration in its bispectrum. In addition, the nonlinear processes that cause the equilateral components imply that all the three components, being almost equal, must have left the horizon during same time. Similarly, a positive squeezed bispectrum implies that for the overdense large-scale structure there exists more corresponding small-scale structures and for underdense large-scale structure less small-scale structure. In 3D space, the three wave-vectors represent planes and define the bispectrum.

For the slow-roll inflation, the gravitational potential in real-space is Taylor expanded as [Komatsu et al., 2009],

$$\Phi(\mathbf{x}) = \Phi_{\rm G}(\mathbf{x}) + f_{\rm NL}(\Phi^2_{\rm G}(\mathbf{x}) - \langle\Phi_{\rm G}(\mathbf{x})\rangle^2) + ... \tag{2.34}$$

where, the parameter $f_{\rm NL}$ is the measure of the non-Gaussianity in the bispectrum and

$$\langle\Phi_{\rm G}(\mathbf{x})\rangle = \int \frac{{\rm d}^3k}{(2\pi)^3} P_\Phi(k)$$

and,

$$\Phi_{\rm NG}(\mathbf{x}) = \Phi^2_{\rm G}(\mathbf{x}) - \langle\Phi_{\rm G}(\mathbf{x})\rangle^2$$

The Equation 2.34 written in Fourier space is given as,

$$\Phi(\mathbf{k}) = \Phi_{\rm G}(\mathbf{k}) + f_{\rm NL}\ \Phi_{\rm NG}(\mathbf{k}) + ... \tag{2.35}$$

where,

$$\Phi_{\rm NG}(\mathbf{k}) = \int \frac{{\rm d}^3p}{(2\pi)^3}\ \Phi_{\rm G}(\mathbf{k}+\mathbf{p})\ \Phi^\star_{\rm G}(\mathbf{p}) - (2\pi)^3\delta(\mathbf{k})\langle\Phi_{\rm G}(\mathbf{x})\rangle^2 \tag{2.36}$$

Now, the primordial bispectrum is estimated as,

$$\begin{aligned}\langle\Phi_{\rm G}(\mathbf{k}_1)\Phi_{\rm G}(\mathbf{k}_2)\Phi_{\rm NG}(\mathbf{k}_3)\rangle = &\int \frac{{\rm d}^3k}{(2\pi)^3}\langle\Phi_{\rm G}(\mathbf{k}_1)\Phi_{\rm G}(\mathbf{k}_2)\rangle\langle\Phi_{\rm G}(\mathbf{k}_3+\mathbf{p})\Phi^{\star}_{\rm G}(\mathbf{p})\rangle \\ &+ \int \frac{{\rm d}^3k}{(2\pi)^3}\langle\Phi_{\rm G}(\mathbf{k}_1)\Phi^{\star}_{\rm G}(\mathbf{p})\rangle\langle\Phi_{\rm G}(\mathbf{k}_2)\Phi_{\rm G}(\mathbf{k}_3+\mathbf{p})\rangle \\ &+ \int \frac{{\rm d}^3k}{(2\pi)^3}\langle\Phi_{\rm G}(\mathbf{k}_1)\Phi_{\rm G}(\mathbf{k}_3+\mathbf{p})\rangle\langle\Phi_{\rm G}(\mathbf{k}_2)\Phi^{\star}_{\rm G}(\mathbf{p})\rangle \\ &- (2\pi)^3\delta(\mathbf{k}_3)\langle\Phi_{\rm G}(\mathbf{k}_1)\Phi_{\rm G}(\mathbf{k}_2)\rangle\langle\Phi^2_{\rm G}(\mathbf{x})\rangle\end{aligned} \tag{2.37}$$

The above equation is rearranged as the local bispectrum and yields,

$$B_\Phi(k_1,k_2,k_3) = 2f_{\rm NL}(P_\Phi(k_1)P_\Phi(k_2)+P_\Phi(k_1)P_\Phi(k_3)+P_\Phi(k_2)P_\Phi(k_3)) \tag{2.38}$$

where, a more general definition if $f_{\rm NL}$ is given as,

$$f_{\rm NL} = \frac{B_\Phi(k,k,k)}{6P_\Phi(k)^2} \tag{2.39}$$

Estimating $f_{\rm NL}$ in turn is the amplitude of the bispectrum.

2.6.1 Estimating the bispectrum

As mentioned above, the bispectrum is the three-point correlator of the underlying field and measures the higher order statistics of skewness. There are various estimators that may be used to estimate the bispectrum. In this section, we describe the method developed by Regan [2011] to estimate the bispectrum. This method is used in this thesis and described below.

The bispectrum, B_Φ, of a given field Φ (this field could ionization field or the brightness temperature), is given as following,

$$\langle\Phi(\mathbf{k}_1)\Phi(\mathbf{k}_2)\Phi(\mathbf{k}_3)\rangle = (2\pi)^3\delta^{\rm D}(\mathbf{k}_1+\mathbf{k}_2+\mathbf{k}_3)B_\Phi(k_1,k_2,k_3) \tag{2.40}$$

where, $\delta^{\rm D}$ is the Dirac delta function and $\mathbf{k}_1,\mathbf{k}_2,$ and $\mathbf{k}_3$ are the Fourier modes (wave-vectors) and k_1,k_2,k_3 are their amplitudes. The $\langle\rangle$ indicate the averaging over many realizations but for this case we only have one simulation as is the case with the real world measurements. This manifests as cosmic variance.

The bispectrum is represented as a sum of a basis given as,

$$w(k_1, k_2, k_3)B(k_1, k_2, k_3) = \sum_n \alpha_n Q_n(k_1, k_2, k_3) \tag{2.41}$$

where, $w(k_1, k_2, k_3)$ is the weight, Q_n are the basis spectra and α_n are the associated coefficients. Etimating the values of the coefficients then yields the shape and the amplitude of the bispectrum. We define, the bisepctrum, $\hat{B}$, as the original bispectrum of the Universe, while, B is the theoretical value, averaged over many instantiations. In the following study, we only have one simulation set and therefore are variance limited. The approach is to find the overlap of the estimated bispectrum with the one we have injected in the simulation ($f_{\rm NL} = 50$).

We define a measure of the overlap of two arbitrary functions f and g, similar to the Fisher matrix measure for CMB defined by Regan et al. [2013], as following, (note that the variance of the bispectrum is given by $P(k_1)P(k_2)P(k_3)$, so the following may be considered an inverse variance measure)

$$\begin{aligned}\langle f|g\rangle &\equiv \int \frac{\mathrm{d}^3\mathbf{k}_1\ \mathrm{d}^3\mathbf{k}_2\ \mathrm{d}^3\mathbf{k}_3}{(2\pi)^9}\ (2\pi)^3\ \delta\left(\sum \mathbf{k}_i\right)\ \frac{f(\mathbf{k}_1, \mathbf{k}_2, \mathbf{k}_3)\ g(\mathbf{k}_1, \mathbf{k}_2, \mathbf{k}_3)}{P(k_1)\ P(k_2)\ P(k_3)} \\ &= \int \frac{\mathrm{d}^3\mathbf{k}_1\ \mathrm{d}^3\mathbf{k}_2\ \mathrm{d}^3\mathbf{k}_3}{(2\pi)^9}\ \mathrm{d}^3\mathbf{x}\ e^{i\sum_j \mathbf{k}_j\cdot\mathbf{x}}\ \frac{f(\mathbf{k}_1, \mathbf{k}_2, \mathbf{k}_3)\ g(\mathbf{k}_1, \mathbf{k}_2, \mathbf{k}_3)}{P(k_1)\ P(k_2)\ P(k_3)}\end{aligned} \tag{2.42}$$

Now suppose, f, and g do not have angular dependence, that is, $f = f(k_1, k_2, k_3)$, then this implies,

$$\begin{aligned}\langle f|g\rangle = \int \frac{(xk_1k_2k_3)^2\ \mathrm{d}^3\mathbf{k}_1\ \mathrm{d}^3\mathbf{k}_2\ \mathrm{d}^3\mathbf{k}_3}{(2\pi)^9}\ \int \left(\mathrm{d}\hat{\mathbf{x}}\ \mathrm{d}\hat{\mathbf{k}}_1\ \mathrm{d}\hat{\mathbf{k}}_2\ \mathrm{d}\hat{\mathbf{k}}_3\ e^{i\sum_j \mathbf{k}_j\cdot\mathbf{x}}\right) \\ \times\ \frac{f(k_1, k_2, k_3)\ g(k_1, k_2, k_3)}{P(k_1)\ P(k_2)\ P(k_3)}\end{aligned} \tag{2.43}$$

Recall, that the plane wave is written as the sum of spherical waves expressed in Legendre polynomials as,

$$e^{i\mathbf{k}\cdot\mathbf{x}} = \sum_l i^l(2l+1)j_l(kx)P_l(\hat{\mathbf{k}}\cdot\hat{\mathbf{x}}) \tag{2.44}$$

or, in spherical coordinates the above equation is written as,

$$e^{i\mathbf{k}\cdot\mathbf{x}} = 4\pi \sum_{lm} i^l j_l(kx) Y_{lm}(\hat{\mathbf{k}}) Y^\star_{lm}(\hat{\mathbf{x}}) \tag{2.45}$$

where, Y_{lm} are the spherical harmonics in the multipole space l_i and j_l are the Bessel functions.

$$\implies e^{i\sum_j \mathbf{k}_j\cdot\mathbf{x}} = (4\pi)^3 \prod_j \sum_{l_j m_j} i^{l_j} j_{l_j}(k_j x) Y_{lm}(\hat{\mathbf{k}}) Y^\star_{lm}(\hat{\mathbf{x}}) \tag{2.46}$$

Thus, the middle term in the Equation 2.43 is rewritten as,

$$\begin{aligned}\int \left(\mathrm{d}\hat{\mathbf{x}}\ \mathrm{d}\hat{\mathbf{k}}_1\ \mathrm{d}\hat{\mathbf{k}}_2\ \mathrm{d}\hat{\mathbf{k}}_3\ e^{i\sum_j \mathbf{k}_j\cdot\mathbf{x}}\right) &= (4\pi)^3 i^{\sum_j l_j}\ j_{l_1}(k_1x)\ j_{l_2}(k_2x)\ j_{l_3}(k_3x) \\ &\int \mathrm{d}\hat{\mathbf{k}}_1\ \mathrm{d}\hat{\mathbf{k}}_2\ \mathrm{d}\hat{\mathbf{k}}_3\ Y_{l_1m_1}(\hat{\mathbf{k}}_1)\ Y_{l_2m_2}(\hat{\mathbf{k}}_2)\ Y_{l_3m_3}(\hat{\mathbf{k}}_3) \\ &\int \mathrm{d}\hat{\mathbf{x}}\ Y^\star_{l_1m_1}(\hat{\mathbf{x}})\ Y^\star_{l_2m_2}(\hat{\mathbf{x}})\ Y^\star_{l_3m_3}(\hat{\mathbf{x}})\end{aligned} \tag{2.47}$$

Now substituting,

$$\int \mathrm{d}\hat{\mathbf{k}}_1\ Y_{l_1m_1}(\hat{\mathbf{k}}_1) = \sqrt{4\pi}\delta_{l_10}\delta_{m_10}$$

and,

$$\int \mathrm{d}\hat{\mathbf{x}}\ Y^\star_{00}(\hat{\mathbf{x}})\ Y^\star_{00}(\hat{\mathbf{x}})\ Y^\star_{00}(\hat{\mathbf{x}}) = \frac{4\pi}{(4\pi)^3}$$

$$\implies \int \left(\mathrm{d}\hat{\mathbf{x}}\ \mathrm{d}\hat{\mathbf{k}}_1\ \mathrm{d}\hat{\mathbf{k}}_2\ \mathrm{d}\hat{\mathbf{k}}_3\ e^{i\sum_j \mathbf{k}_j\cdot\mathbf{x}}\right) = (4\pi)^4 j_0(k_1x)\ j_0(k_2x)\ j_0(k_3x) \tag{2.48}$$

Furthermore,

$$\int x^2\ j_0(k_1x)\ j_0(k_2x)\ j_0(k_3x)\ \mathrm{d}x = \frac{\pi}{4k_1k_2k_3} \tag{2.49}$$

$$\begin{aligned}\implies \langle f|g\rangle &= \frac{(4\pi)^4\pi}{4(2\pi)^9} \int \mathrm{d}k_1\ \mathrm{d}k_2\ \mathrm{d}k_3\ \frac{k_1k_2k_3}{P(k_1)P(k_2)P(k_3)}\ f(k_1,k_2,k_3)g(k_1,k_2,k_3) \\ &= \frac{1}{\pi(2\pi)^3} \int \mathrm{d}k_1\ \mathrm{d}k_2\ \mathrm{d}k_3\ [wf](k_1,k_2,k_3)[wg](k_1,k_2,k_3)\end{aligned} \tag{2.50}$$

where, the weight,

$$w = \sqrt{\frac{k_1k_2k_3}{P(k_1)P(k_2)P(k_3)}}\quad ,$$

and the bispectrum is expanded in a basis, see Equation 2.41, as $wB = \sum_n \alpha_n Q_n$.

$$\implies \langle f|g\rangle = \sum_{nm} \alpha_n \alpha_m \Big\langle \frac{Q_n}{w}, \frac{Q_m}{w} \Big\rangle \tag{2.51}$$

where,

$$\Big\langle \frac{Q_n}{w}, \frac{Q_m}{w} \Big\rangle = \frac{1}{\pi(2\pi)^3} \int \mathrm{d}k_1 \ \mathrm{d}k_2 \ \mathrm{d}k_3 \ Q_n(k_1, k_2, k_3) Q_m(k_1, k_2, k_3)$$
$$\equiv \gamma_{nm}$$

$$\implies \langle f|g\rangle = \sum_{nm} \alpha_n \alpha_m \gamma_{nm} \tag{2.52}$$

Now let us substitute bispectrum for the functions f and g as,

$$f = \hat{B} = \frac{\delta_{\mathbf{k}_1} \delta_{\mathbf{k}_2} \delta_{\mathbf{k}_3}}{V},$$
$$g = B = \frac{\sum_n \alpha_n Q_n}{w}$$

$$\implies \langle \hat{B}|B\rangle = \int \mathrm{d}^3\mathbf{x} \ \frac{\mathrm{d}^3\mathbf{k}_1 \ \mathrm{d}^3\mathbf{k}_2 \ \mathrm{d}^3\mathbf{k}_3}{(2\pi)^9} \ \frac{e^{i\sum_j \mathbf{k}_j \cdot \mathbf{x}}}{P(k_1)P(k_2)P(k_3)} \times \frac{\delta_{\mathbf{k}_1} \delta_{\mathbf{k}_2} \delta_{\mathbf{k}_3}}{V} \ \frac{\sum_n \alpha_n Q_n(k_1, k_2, k_3)}{w(k_1, k_2, k_3)} \tag{2.53}$$

Substituting,

$$P(k_1)P(k_2)P(k_3) \ w = \sqrt{k_1 P(k_1) k_2 P(k_2) k_3 P(k_3)}$$

in the Equation 2.53 above gives,

$$\langle \hat{B}|B\rangle = \int \mathrm{d}^3\mathbf{x} \ \frac{\mathrm{d}^3\mathbf{k}_1 \ \mathrm{d}^3\mathbf{k}_2 \ \mathrm{d}^3\mathbf{k}_3}{(2\pi)^9} \ \frac{e^{i\sum_j \mathbf{k}_j \cdot \mathbf{x}}}{\sqrt{k_1 P(k_1) k_2 P(k_2) k_3 P(k_3)}} \ \frac{\delta_{\mathbf{k}_1} \delta_{\mathbf{k}_2} \delta_{\mathbf{k}_3}}{V} \ \sum_n \alpha_n Q_n \tag{2.54}$$

where, V is the simulation volume and the quantity $Q_n = q_n(j_1) q_n(j_2) q_n(j_3)$, thus,

$$\langle \hat{B}|B\rangle = \frac{\sum_n \alpha_n}{V} \int \mathrm{d}^3\mathbf{x} N_{n_1}(\mathbf{x}) N_{n_2}(\mathbf{x}) N_{n_3}(\mathbf{x}) \tag{2.55}$$

where,

$$N_{n_1}(\mathbf{x}) = \int \frac{\mathrm{d}^3\mathbf{k}_1}{(2\pi)^3} \ \frac{\delta_{\mathbf{k}_1} q_{n_1}(k_1)}{\sqrt{k_1 P(k_1)}} \ e^{i\mathbf{k}_1 \cdot \mathbf{x}}$$

or further simplified,

$$\langle \hat{B}|B\rangle = \sum_n \alpha_n \beta_n \tag{2.56}$$

where,

$$\beta_n = \frac{1}{V}\int \mathrm{d}^3\mathbf{x} N_{n_1}(\mathbf{x}) N_{n_2}(\mathbf{x}) N_{n_3}(\mathbf{x})$$

Note that for $\hat{B} \equiv B$, and from equation 2.52, we get,

$$\beta_n = \sum_m \alpha_m \gamma_{nm} \tag{2.57}$$

$$\implies \alpha_n = \sum_m \gamma^{-1}_{nm}\ \beta_m \tag{2.58}$$

Recall from Equation 2.41, α_n are the coefficients for the polynomials that construct the bispectrum.

Now, for the amplitude of the bispectrum we will define the measure for the Fisher matrix as, recall Equation 2.39,

$$\mathbf{F} = \frac{\langle B|B\rangle}{6} \tag{2.59}$$

Assuming that the bispectrum is linear in f_{NL}, the error on the bispectrum amplitude f_{NL} is given as,

$$\Delta f_{\mathrm{NL}} = \frac{1}{\sqrt{\mathbf{F}}} \tag{2.60}$$

The signal for the bispectrum is detectable in the limit that $\mathbf{F} \geq 1$.

To recap, α_n gives us the bispectrum andΔ f_{NL} gives us the error in the estimated amplitude.

In this approach, we are exploring the basic premise that over time the primordial non-Gaussianity is dissipated and subsumed by additional nonlinear processes. Therefore, in searching for the primordial non-Gaussianity the CMB is the earliest epoch that will preserve any underlying nonlinearities. The next best epoch for searching non-Gaussianity would be the 21-cm era, especially more during the Dark Ages than the EoR. More importantly, the evolution of the nonlinearities will be more evident in 21-cm data, due to tomography, as compared to the CMB data. We examine the concept of extracting the

bispectrum information from the 21-cm data using the upcoming radio telescopes.

Chapter 3

The EoR and the Dark Ages

In this chapter we will briefly review the physics of the redshifted 21-cm hyperfine hydrogen line and its detectability. We will review the observational evidence for the reionization. We will also discuss the presence of the high-density absorbers, specifically, the Lyman-limit Systems (LLS). In Part III of the thesis, we examine in detail the effects of these absorbers on the process of reionization.

3.1 The 21-cm Physics

The redshifted 21-cm hyperfine hydrogen line has been successfully used to probe the gas dynamics as captured by the neutral hydrogen in the Milky Way and other galaxies. The hydrogen line is observed both in emission and absorption. For high-redshift and cosmological studies the redshifted 21-cm is observed against the bright sources (quasars) in absorption, highlighting the neutral hydrogen densities along the line of sight.

The 21-cm transition is the change of hyperfine energy states at the ground level, denoted by the quantum number $n = 1$. The total spin angular momentum of the hydrogen atom is the sum of the spins of the electron and the proton, $F = S + I$. Since the values of S and I are $\pm 1/2$, in the units of $\hbar$, the value of F is 0 or 1. This manifests as the splitting of the ground level. In the presence of a magnetic field, the $F = 1$ state is further split into three levels and is called the triplet state, while F = 0 is termed the singlet state. The energy gap between the triplet and singlet is 5.874 μeV. This corresponds to the $h\nu_{10}$ transition of a 21.106 cm (1420.405 MHz) photon.

The observability of the redshifted 21-cm is defined as the differential brightness temperature with respect to the background source with brightness temperature $T_{\rm B}$ and defined as, [Field, 1959],

$$\delta T_{\rm b} = T_{\rm S}(1 - e^{-\tau_\nu}) + T_{\rm B}\ e^{-\tau_\nu} - T_{\rm B} \tag{3.1}$$

$\delta T_{\rm b}$ is the differential brightness temperature as sensed by the antenna, the first term on the right hand side of the equation is the self-absorbed cloud radiation, the second term is the diminished radiation from the background source, and the last term is the true source brightness. The optical depth along the line of sight is $\tau(\nu) = \int {\rm d}s\ \alpha_\nu(s)$, where α_ν is the absorption coefficient. $T_{\rm S}$ is the spin temperature and is defined as the ratio of the populations of the triplet and singlet states of an ensemble of neutral hydrogen atoms. Assuming thermodynamical equilibrium, according to Boltzmann's distribution, the spin temperature is defined as,

$$\frac{g_0 n_1}{g_1 n_0} = \exp\left(\frac{-h\nu_{10}}{kT_{\rm S}}\right) \equiv \exp\left(\frac{-T_\star}{T_{\rm S}}\right) \tag{3.2}$$

where, the statistical degeneracy factors $g_1/g_0 = 3$, and for 21-cm, $T_\star \equiv hc/k\lambda_{\text{21-cm}} = 0.068$ K.

The spin temperature of the neutral hydrogen is determined by the absorption and emission of the 21-cm photons with the temperature $T_{\rm CMB}$. In the early Universe these photons are from the CMB continuum. The spin temperature also depends on the collisions of hydrogen atoms and other electrons leading to the kinetic temperature $T_{\rm K}$. In addition, the temperature due to the scattering of Lyα photons, $T_{\rm L}$, also affects the spin temperature, [Field, 1959, Pritchard and Loeb, 2012]. All these effects collectively define the spin temperature as the weighted mean,

$$T_{\rm S} = \frac{T_{\rm CMB} + y_{\rm C}T_{\rm K} + y_{\rm L}T_{\rm L}}{1 + y_{\rm C} + y_{\rm L}} \tag{3.3}$$

where, $y_{\rm C}$ and $y_{\rm L}$ are the normalized probabilities of the collisions and Lyα scattering respectively.

Now we can rewrite the Equation 3.1 as the differential brightness temperature of the redshifted 21-cm with respect to the CMB and the spin temperature T_S of the neutral hydrogen with density ρ_{HI} as,

$$\begin{aligned}\delta T_b &= \frac{T_S - T_{CMB}}{1+z}\,(1-e^{-\tau}) \\ &\approx \frac{T_S - T_{CMB}}{1+z}\,\frac{3\lambda_0^3 A_{10} T_\star n_{HI}(z)}{32\pi T_S H(z)} \\ &= 28.5\left(\frac{1+z}{10}\right)^{1/2}(1+\delta)\left(\frac{\Omega_b}{0.042}\frac{h}{0.73}\right)\left(\frac{0.24}{\Omega_m}\right)^{1/2} \quad [\mathrm{mK}] \end{aligned} \tag{3.4}$$

where, the quantity $1+\delta$ is the mean number density of the neutral hydrogen. During reionization, the temperature of the hydrogen is same as the collisional temperature and $T_S \approx T_K \gg T_{CMB}$. As a result the ratio $(T_S - T_{CMB})/T_S$ is cancelled and the differential brightness is only the function of the density and the redshift, as shown. In addition, this formalism could be interpreted to be true in real space. For redshift space a multiplicative factor of, $1 - [(1+z)/H(z)][\partial v_\parallel]$ is applied, where, $\partial v_\parallel$ is the velocity gradient along the line of sight.

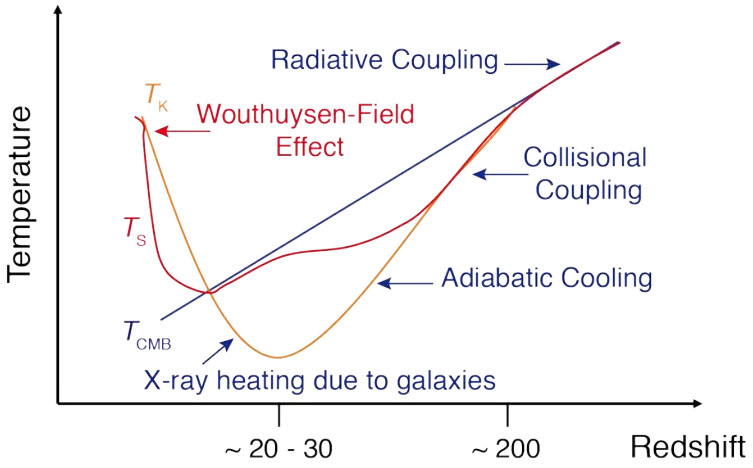

Figure 3.1: The exaggerated schematic of the relation of the spin temperature (T_S) to the CMB (T_{CMB}) and collisional (T_K) temperatures. [Loeb, 2006]

From the second line in the Equation 3.4, it is evident that the brightness temperature depends on the spin temeprature. In the case, $T_S \gg T_{CMB}$, the brightness temperature saturates above the CMB. While for the scenario, $T_S \ll T_{CMB}$, the temperature becomes negative. As we saw above, there are three competing processes defining the spin temperature. These processes evolve in time and consequently affect the spin temperature. A simple schematic in the Figure 3.1 shows the effects of the CMB and collisional

(kinematic) temperatures on the spin temperature as a function of redshift. This is an approximation only to illustrate the trends. The CMB temperature is $\propto (1+z)$. The collisional temperature of the gas tracks the CMB temperature upto $z \sim 200$, after which the collisional temperature cools as $T_{\rm K} \propto (1+z)^2$. With the formation of the first X-ray sources around $z \sim 20-30$ the collisional temperature start to rise well above the CMB. These two processes drive the spin temperature shown in red in the figure. In the early times the spin temperature traces the neutral hydrogen temperature through radiative coupling. The radiative coupling is diminished but picks up again at low redshifts with the increase in star formation. The coupling is facilitated by the newly generated Lyα photons. This process affects the spin temperature and is called the Wouthuysen-Field effect and is discussed in the next section [Field, 1958, Wouthuysen, 1952].

3.1.1 Wouthuysen-Field Effect

With the formation of new Lyα photons sources, the neutral hydrogen absorbs and emits the 10.2 eV Lyα photon and returns to either of the hyperfine spin states. This shuffling results in the coupling of the neutral hydrogen with the Lyα radiation and the process is named after Wouthuysen [1952] and Field [1958], the scientists who proposed it.

(As an aside, as per my Dutch friends, Wouthuysen is pronounced as - *Vowt* · *hi* · *son*.)

The Figure 3.2 illustrates the Wouthuysen-Field effect. The principal quantum states $n = 1, \text{and } 2$ and their respective orbitals, S and P, are shown. Also shown are the hyperfine splits of the orbitals. The notation used to denote the energy levels in $n_F L_J$, where L, J, and F are orbital or the azimuthal quantum number, angular momentum of the electron, and total angular momentum of the atom. Now assuming that a neutral hydrogen atom with all these levels absorbs a Lyα (or a Lyn) photon. This will result in the atom to excite to any of the allowed 2P hyperfine states. As per the electric dipole selection rules,$\Delta\ F = 0, 1$ and $F \not\to 0$. Consequently, the spontaneous emission of the Lyα photon will return the atom to either of the hyperfine ground states. The spin-flip occurs if the atom returns to the hyperfine triplet state. In other words, scattering a Lyα photon generates spin-flip in the population of the hydrogen atom thus coupling the two. The scattering rate depends on a variety of parameters and therefore affects the coupling [Furlanetto et al., 2006, Pritchard and Loeb, 2012] resulting in 21-cm signal variation at $\sim 10\%$ level.

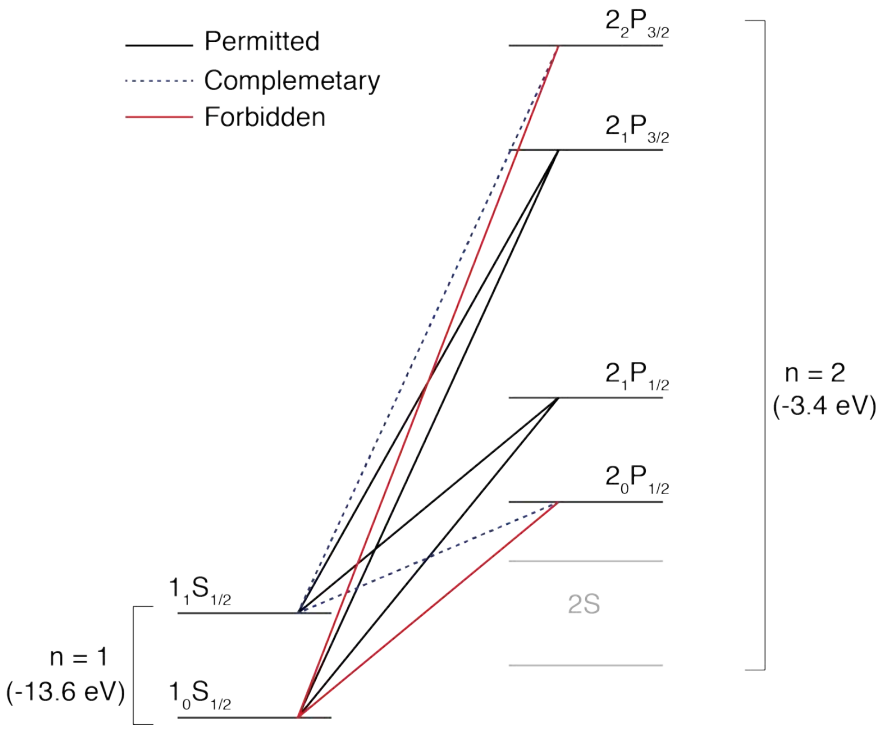

Figure 3.2: The schematic depicting the Wouthuysen-Field effect. The figure shows the hyperfine splittings of the 1S and 2P levels of the hydrogen atom. The black solid line transitions are permitted and allow spin flips resulting in the 21-cm radiation. The black dashed transitions are permitted but do not contribute to spin flips. The red transitions are not permitted.

The effects of the competing processes driving the evolution of the spin temperature and consequently the brightness temperature (the observable) are depicted in the Figure 3.3 from Pritchard and Loeb [2012]. For a detailed and pedagogical review of the thermal history refer to Furlanetto et al. [2006], Loeb [2006], Pritchard and Loeb [2012]. In summary, the combination of the Figures 3.1 and 3.3 highlights the epochs in the evolution of the 21-cm brightness temperature. Immediately after the recombination, the residual free electron population facilitates the thermal coupling of the neutral hydrogen with the CMB via Compton scattering. This sets the $T_{\rm S} = T_{\rm CMB}$. Consequently, $\delta\bar{T}_{\rm b} = 0$, therefore, no detectable 21-cm signal. However, as the adiabatic cooling of the gas begins around $z \sim 200$, the collisional temperature starts to fall as $T_{\rm K} \propto (1+z)^2$. This leads to $T_{\rm S} < T_{\rm CMB}$. This condition results in $\delta\bar{T}_{\rm b} < 0$. That is, the first 21-cm absorption signal emerges. This process continues until around $z = 40$ when the gas density decreases. Once again the $T_{\rm S} = T_{\rm CMB}$ and the 21-cm brightness temperature is no longer visible. It is only when the first stars are formed that the Lyα and X-ray photons are injected into the gas, that the spin temperature $T_{\rm S}$ starts to climb. As the ionization of the neutral hydrogen

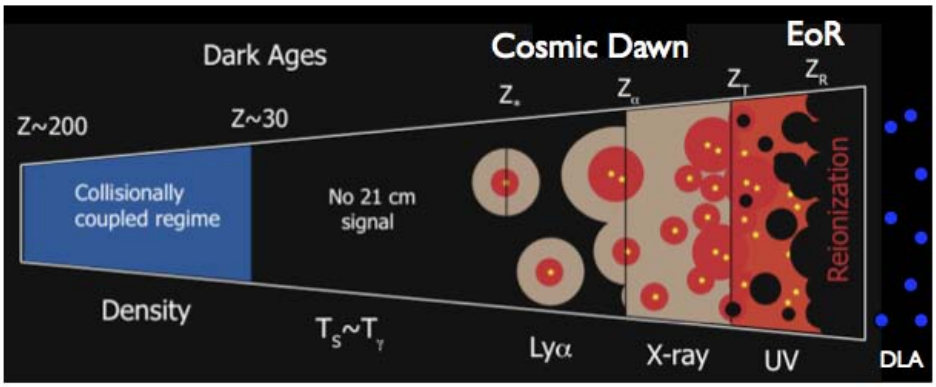

Figure 3.3: *"Cartoon of the different phases of the 21 cm signal. The signal transitions from an early phase of collisional coupling to a later phase of Lyα coupling through a short period where there is little signal. Fluctuations after this phase are dominated successively by spatial variation in the Lyα , X-ray, and ionizing UV radiation backgrounds. After reionization is complete there is a residual signal from neutral hydrogen in galaxies."* Figure and caption from Pritchard and Loeb [2012]

initiates, $T_{\rm S} \sim T_{\rm K} \gg T_{\rm CMB}$, the brightness temperature fluctuations are manifested as a combination of the fluctuation in the ionization, gas density, and temperature. Eventually, the continued heating of the gas renders the temperature fluctuations irrelevant and the dependence on the spin temperature is ignored. This is when the 21-cm signal is dominated by the ionization fluctuations. At the end of the reionization the left over neutral hydrogen is observed in 21-cm in isolated gravity potentials such as galaxies.

3.2 Observational Evidence for the Epoch of Reionization

The observational evidence for the epoch of reionization appears in variety of different studies. However, none the observations provide strong constraints on the evolution of the epoch of reionization. Below we highlight the observations that lend to the evidence of reionization.

3.2.1 Gunn-Peterson Troughs

Gunn and Peterson [1965] predicted that the intervening neutral hydrogen between a quasar and an observer should suppress the emission lines at higher frequencies than that of the Ly-α line (in the rest frame) of the quasar. In the expanding Universe model, the UV photons are absorbed by the neutral hydrogen resonance line at 1215.67Å. This suppression traces the intervening neutral hydrogen and appears as a trough in the quasar spectrum. In 2001 the first evidence of the trough was observed in the spectrum of a quasar at $z = 6.28$ [Becker et al., 2001]. This put an upper limit on the neutral hydrogen

ionization fraction at > 0.001. This discovery when combined with the absence of Gunn-Peterson trough in the spectra of quasars at $z < 6$ thus weakly constraints the ending of the reionization.

3.2.2 Thomson Scattering of CMB

Thomson scattering of the CMB is another tracer of the reionization and is discussed in detail in, for example, [Bond and Efstathiou, 1984, Peebles and Yu, 1970, Sunyaev and Zeldovich, 1972]. The brief review as discussed here is that the CMB photons provide information relevant to the history of reionization. The CMB photons are scattered by the intervening reionized hydrogen (free electrons) resulting in the suppression of the temperature fluctuations proportional to $1-e^{-\tau}$, [Zaldarriaga, 1997], where τ is the optical depth. This scattering signature is imprinted as secondary anisotropies in the CMB power spectrum. The observed value of τ in the Planck data [Planck Collaboration et al., 2013] is $\tau_{\rm es} = 0.089 \pm 0.032$ (68%; Planck + lensing). This value of the optical depth favors the evolutionary reionization over the spontaneous reionization model.

Another probe using the CMB is the polarization spectrum of the CMB. The primordial fluctuations set the largest quadrupole anisotropies to an angular size of 1°, [Sugiyama, 1995]. Any anisotropies introduced later in the cosmological evolution, say due to Thomson scattering during reionization, are observed as larger than the primordial anisotropy.

3.2.3 Other Observational Evidence an Probes

The other observational probes that may provide evidence for reionization and put constraints include, directly studying the high redshift IGM. These observations include, the thermal evolution of the IGM, see [Bolton et al., 2010] and references therein, the estimation of the ionizing photons per baryon, see [Bolton and Haehnelt, 2007]. In addition, the kinetic Sunyaev-Zeldovich effect, see [Park et al., 2013], on the CMB due to reionization is also a probe to study the history of reionization. Other probes include Lyman-α emitters, high redshift QSOs/GRBs, and metal abundance at high redshift as discussed in Zaroubi [2013].

3.3 The Lyman-Limit Systems

The brightness temperature of the neutral hydrogen is affected by other features. This section explores the observational evidence of the H I absorbers called the Lyman-limit systems (LLS) and their effect on the ionization and thereby the brightness temperature. The observational models are used to develop numerical simulations and study the effects on the observables.

3.3.1 Introduction

After the decoupling of the CMB radiation from the ordinary matter at the surface of last scattering (at redshift $z \sim 1100$), the pre-galactic medium (PGM), primarily composed of atomic hydrogen, remained largely neutral until the first stars formed, likely at $z > 30$. This is the period when the small density fluctuations reflected in the CMB anisotropies grew gravitationally and gave rise to the foundations of the large-scale structures. The diffuse photon population was dominated by the CMB and the 21.10 cm (1420.40 MHz) emission from the hyperfine line of the neutral hydrogen. Recall that the period between the release of the CMB and the formation of the first stars is termed as the "Dark Ages" [Sargent, 1986]. The reionization of the neutral hydrogen in the PGM began soon after the first luminous sources producing the ionizing UV radiation were formed. This era is commonly referred to as the "Epoch of Reionization" (EoR). By redshift $z \sim 6$ (roughly a billion years after the big bang), save for some dense regions, the neutral hydrogen in the PGM was fully ionized.

There are many compelling reasons for studying these epochs of the Universe. The process of reionization completely transformed the Universe and had significant effects on subsequent galaxy and star formation. However, at present there is not much direct observational data available from these epochs. The study of the redshifted 21-cm from neutral hydrogen has the potential to provide the understanding of a wide range of cosmological and astrophysical phenomena. For example,

(i) The ionization history provides indirect insight into the early ionizing sources such as the first galaxies. Very little is known about such galaxies, of which the farthest observed is at redshift range of $z \sim$ 8-10 with V magnitude of about 29 [Bouwens

et al., 2011, Lorenzoni, 2011]. The reionization history provides constraints on sources that can cause a global transition of the Universe from a cold neutral to a warm almost fully ionized state. Furthermore, the star formation history, escape fraction of ionization photons, masses, H II region morphologies etc. put constraints on early type galaxies.

(ii) The concordant cosmological model is largely derived from the CMB data at $z \sim 1100$ and the large-scale structure data at lower redshifts. The observations of the redshifted 21-cm complements these by providing much richer volumetric (tomography) data spanning several redshifts, thereby, directly accessing the evolutionary history of the Universe. In addition, the three-dimensional power spectrum and its first moment may allow constraining the non-Gaussianity in the primordial scalar field.

An exhaustive list of science drivers for studying the Dark Ages and EoR is provided in [Mellema et al., 2013] and references therein.

The observational evidence and constraints for the reionization is made available from two primary sources, one, from the linear polarization of the CMB due to Thomson scattering of CMB photons by free electrons, and two, from the **?** troughs in the quasar spectrum. The recent Planck results [Planck Collaboration et al., 2013] place a 1-σ lower limit on the scattering optical depth $\tau_{\rm es} = 0.089 \pm 0.032$ (Planck + lensing). This value is higher than the value for instantaneous reionization at $z = 6$, thus supporting an extended reionization scenario.

Reionization is a complex process further complicated by feedback and recombinations. While the emerging sources inject the ionizing photons into the intergalactic medium (IGM) creating growing H II regions, the dense neutral hydrogen regions with H I column densities of $10^{17}{\rm cm}^{-2} < {\rm N_{H\,I}} < 10^{20}{\rm cm}^{-2}$ and continuum optical depths of order the 1, called Lyman-limit systems (LLSs), absorb the ionizing photons thereby slowing the ionization front and extending the ionization process [Ciardi, 2006, Finlator et al., 2012, Kaurov and Gnedin, 2013, McQuinn et al., 2007, Miralda-Escudé, 2003, Sobacchi and Mesinger, 2014]. The LLSs, assumed to be located at the outer regions of the halos, are

among the most prolific Lyman-α absorbers [Furlanetto et al., 2006].

As the current and future experiments - Giant Metre-wave Radio Telescope (GMRT) [Paciga et al., 2011], Low Frequency Array (LOFAR) [Harker et al., 2010], Murchison Widefield Array (MWA) [Lonsdale et al., 2009], PAPER [Parsons et al., 2010], Square Kilometre Array (SKA) [Schilizzi, 2004] etc. - designed to study the EoR and Dark Ages, define their optimal observational strategies, the parametric simulations continue to constraint the observable phase space. The first generation of radio telescopes will measure statistical properties of the 21-cm ionization fields in the form of power spectra which is tightly coupled with the evolution of the sizes of the H II regions. This study focuses on the effects of the Lyman continuum absorbers, especially the LLSs, on the ionization field and the consequent observables. Similar studies with photon sinks such as minhalos [Iliev et al., 2005, 2007] and clumping factors due to simulation resolution limits, have been done [Mellema et al., 2006b]. While in the real world scenarios all the factors contribute to the complex ionization process, it is imperative to closely study the effects in isolation.

3.3.2 Definition of Lyman-limit Systems

The H I column densities, estimated by the absorption lines of the intervening hydrogen observed in quasar spectra, are used to categorize the hydrogen absorption systems into three overlapping states, *viz.*, Lyman-α forest (for H I column densities $N_{\rm HI} < 10^{17}{\rm cm}^{-2}$), Lyman-limit systems (LLSs, $10^{17}{\rm cm}^{-2} < N_{\rm HI} < 10^{20}{\rm cm}^{-2}$), and damped Ly-$\alpha$ systems (DLAs, $N_{\rm HI} > 10^{20}{\rm cm}^{-2}$). The Ly-$\alpha$ forest consists of low density and highly ionized structures, in contrast to DLAs that are high density and partly neutral, thus exhibiting a strong damping wing of the Ly-α line. The studies of these systems have enabled precise measurements of the $N_{\rm HI}$ values leading to high precision constraining of observables ranging from primordial power spectrum to the tracing of neutral hydrogen that forms the first stars and prototype galaxies. The Lyman-α forest and DLAs do not affect the reionization process significantly due to their low optical depth (forest) and relative rarity (DLAs). In contrast, LLSs have both a relatively high optical depth and abundance, and thus the potential to considerably influence the later stages of the reionization, [Alvarez and Abel, 2012].

First observed as quasar absorption lines in surveys [Tytler, 1982], the Lyman-limit systems appear as abrupt discontinuities in the quasar absorption line spectra at the rest-frame Lyman limit at wavelength $\lambda \sim 912$ Å. Prochaska et al. [2010] define LLS as regions with Lyman continuum optical depth of $\tau_{\rm LLS} \geq 2$, *i.e.*, $N_{\rm HI} \geq 10^{17.5}$ cm^{-2}. The LLSs are assumed to be located in and around galactic halos. These systems are relatively easily identifiable even with low resolution and poor signal-to-noise. However, unlike the Lyα forest and DLAs, the LLSs are poorly understood as they are hard to constrain largely because $N_{\rm HI}$ estimations require complete spectral coverage of the Lyα line and the Lyman break. At lower redshifts ($z < 2.6$) the Lyman limit is shifted into the UV spectrum and thus is unobservable from the ground. High redshift surveys [Prochaska et al., 2010, Songaila and Cowie, 2010] present measurements and models of the number density function of the LLS. Another recent survey [Ribaudo et al., 2011] with Hubble Space Telescope archival data identifies 206 LLSs for $z < 2.6$.

All these surveys identify the LLSs in the absorption line spectra and estimate the number of LLSs per unit redshift per H I column ($N_{\rm HI}$) density function - $f(N_{\rm HI}, z) \propto \partial^2\mathcal{N}/\partial z \partial N_{\rm HI}$. The best fit power-law index, β, to this function constraints the column densities of the LLSs. In addition, the earlier simulation studies [Kohler and Gnedin, 2007, McQuinn et al., 2011, Sobacchi and Mesinger, 2014] of the LLS abundances and the mean free path (mfp) of the ionizing photons agree reasonably well with the observations. Using the parametric values of the distribution function from the observations [Songaila and Cowie, 2010] and simulation model [McQuinn et al., 2011] we define two simulation models, LLS1 and LLS2 respectively (see § 5.1.3 and Table 5.3 for details).

The general effect of the LLSs is to constrain the mfp and consequently impede the evolution and merging of the H II regions. In early times, the neutral patches dominate the optical depth thus regulating the ionizing front. Whereas, towards the end of the reionization, the H II regions grow really large leading to increased mfp. In between these two ionized stages the mfp of the photons increases enough to allow them to reach distances where the LLSs contributions start to matter. This is the stage where the LLSs begin to regulate the ionization history. At late times, there are many groups of local ionizing sources that add to the ionization fronts further complicating the morphological evolution

of the ionized regions. The simulations discussed herein attempt to quantify the effects of the LLSs on the reionization history, with the caveat that the lack of high redshift observational data leads to an ad hoc implementation of the LLS models at early times. The extrapolation of mfp from observed low redshifts to early times as far as $z = 20$ clearly yields unrealistic values, see Figure 5.1. However, as discussed below, LLSs start to affect the simulations much later at $z = 15.96$ (LLS1) and $z = 13.30$ (LLS2) with mfp value of 0.1 Mpc in proper units. More accurate effects of LLS at higher redshifts could only be modeled based upon the actual distribution of the high redshift LLSs. However, the very first numerical simulations of a large volume and higher dynamic range presented here, elucidates various useful insights beneficial for future research in the field. This study is similar to other ionization photon sinks affecting EoR that have been examined in prior studies, such as, self-shielding, mini haloes, and clumping factor.

Chapter 4

Radio Interferometry

This chapter is a basic introduction to the fundamentals of radio interferometry. For an in-depth mathematical treatise there are many references elucidating the subject, *viz.*, Taylor et al. [1999], Thompson et al. [2001], Wilson et al. [2013]. This chapter, however, circumvents most of the pedagogical approach and explores the radio interferometry from an intuitive perspective. Thereafter, the chapter refreshes upon the basic mathematical formalism, and finally reviews the relatively new framework entitled the radio interferometry measurement equation introduced in Hamaker [2000], Hamaker and Bregman [1996], Hamaker et al. [1996], Sault et al. [1996], Smirnov [2011a,b,c,d].

4.1 An Intuitive Perspective

There are many physical phenomena that generate the radiation in the radio part of the electromagnetic spectrum raging roughly in the wavelengths λ = 0.3mm - 30m. These arbitrary demarcations are largely driven by the techniques used for the detection of the radiation. The radiation generation processes are classified into two broad categories, namely, thermal and non-thermal. The cumulative power of the photons generated by thermal processes is proportional to the fourth power of the temperature of the body. This is the Stephan's-Boltzmann's law, $P = A\epsilon\sigma T^4$, where P is total power radiated by the body, A is the surface area of the radiating body, ϵ is the emissivity efficiency, σ is the Stefan-Boltzmann's constant, and T is the temperature. The thermal radiation is further categorized into the three subtypes, blackbody, free-free (Bremsstrahlung), and spectral line thermal radiation. The non-thermal radiation does not follow the $\propto T^4$ relationship. Instead, the non-thermal radiation is proportional to the increasing wavelength. The

subtypes of the non-thermal radiation are, synchrotron and maser.

The radiation in the radio domain is detected as waves. The radio telescopes are designed as curved surfaces to focus the incident waves to a receiver. The focused waves, mostly the time varying electric field, $E(t)$, generate a voltage at the receiver, the square of which is directly proportional to the power of the radiating body. The incident signal is a statistical ensemble of many radiating atoms/molecules, in some cases at different frequencies, of the radiating body.

In the optical domain the properties of the glass and/or mirror allow for the formation of the image. This is mathematically equivalent to the Fourier transform of the optical phase difference at the exit pupil of an optical system, see Born and Wolf [1999], Goodman [2005], Hecht [2001]. Same principles apply in the radio domain. The only challenge is that the significantly lower spatial resolution ($\sim \lambda/D$) of radio telescopes makes it harder to get similar imaging as the optical counterparts. The option of increasing the diameter of the radio telescope hits the engineering limits at about 300 feet. The large dishes are not only difficult to maneuver but also tend to deform due to gravity. A workaround is to build a very large dish supported by a crater/valley and observe the universe as the Earth rotates. Arecibo radio telescope in Puerto Rico is one such telescope.

Another rather clever technique of increasing the spatial resolution and the sensitivity (proportional to the collecting area) of a telescope is to build an array of many smaller or average sized dishes, collectively representing an extremely large dish. This is akin to segmented mirrors in optical astronomy where small separate hexagonal mirrors collectively form a larger mirror. The signal from all the smaller dishes is "collected" to form the image. This technique is known as radio interferometry sometimes also referred to as aperture synthesis imaging since the smaller antennas are collectively synthesizing an aperture of a much larger antenna. It is useful to note that the larger number of smaller antennas the more complete (filled) the synthesized aperture. The concept of "collecting" the signal from all the antennas is the key to radio interferometry. The "collection" process is intricate and does not amount to simply accumulating signals from each antenna and stacking them. Instead, the "collection" process involves correlating the data from all

the possible pairs of antennas. This is where the physical phenomenon of interferometry comes to bear in the synthesis imaging. The correlation of signals from pairs of antennas is very similar to the Young's double-slit experiment where each antenna forms a slit. The assumption is that the objects of interest are in the far-field and the waves incident on the slits are planar and coherent. Recall that in the Young's double-slit experiment, the plane waves generate Huygens' spherical wavelets at the slits, which in turn interfere with each other and produce an interference pattern. To generate similar interference pattern with radio dishes requires electronics and mathematical modeling. Since this is the intuitive section, we will further explore interference by electronics methodology without the equations.

To generate an interference pattern from a pair of radio telescopes, the signal is correlated (voltages are multiplied pairwise and added) over certain time window, termed as the integration time. The degree of the interference achieved is defined by the level of the coherence of the incoming wave. Many radiators generating waves far away lead to a collective planar wave at infinity. This property is mathematically derived as the van Cittert-Zernike theorem, see Born and Wolf [1999], Thompson et al. [2001]. The best explanation of which is demonstrated by Rouen ducks in a video on YouTube (search for Thirteen Rouen Ducks Create Coherent Waves). In case, this thesis survived the travails of time and is read way in the future then a lot has changed and you need not worry about YouTube. The thirteen ducks jump in the perfectly still pond at different times generating their own different waves that collectively form a coherent wave at a distance. With these conditions satisfied, each pair of antennas - there are $N(N-1)/2$ pairs for N antennas - generates fringes and a collective interference pattern is obtained. The Fourier transform of this pattern yields the map of the sky. This is a relationship mathematically derived as Wiener-Khinchin theorem, see Goodman [1985]. The map has the spatial resolution equivalent to the largest distance of antenna pairs termed baseline. The field of view of such an array is equivalent to the spatial resolution of the signal dish, assuming all the dishes have same diameter. In case of a heterogeneous array, the smallest dish defines the field of view.

The cross-correlation of the voltages from two antennas yields the interference pattern

also known as the visibility function. The effect of the correlation could be perceived as following, the moment the wavefront from the sky incident on the two antennas is correlated, the sky turns into its own Fourier transform. The antenna pair, based upon their location coordinates relative to the position on the sky, then samples a specific portion of this Fourier transform plane. Many baselines, in turn sample different location thereby covering more of the Fourier transformed sky. Furthermore, the rotation of the earth is used to track loci of all the baselines on the Fourier sky to obtain maximum coverage. These tracks are called uv-coverage or the visibility sampling function. The sampled Fourier sky is the visibility map. The Fourier transform of the visibility map yields the map of the sky with the spatial resolution of the longest baseline. This is the basic essence of radio interferometry. The entire process is an attempt to synthesize the image of the sky using a connected array and interleaving electronics. In other words, what a lens performs through internal reflections and refractions as the photons pass through the material is mimicked by radio antennas arrays. However, like everything else, the details are gritty and lead to further challenges.

For example, the above description assumes no frequency dependence of the incoming signal. The incident signal, however, has a certain bandwidth made of a continuum of frequencies. In the Fourier sky explanation mentioned above this amounts to Fourier transforms of the sky for each of those frequencies. Since the baseline projection on the Fourier sky is also a function of the observed frequency, the same baseline observes a slightly different part of the Fourier sky for the different frequencies in the bandwidth. This leads to the smearing of the region of the Fourier sky sampled by the same baseline. This is called bandwidth smearing. In addition, the samples of the Fourier sky are averaged over a time interval - in practice in the range of 10-30 seconds - termed as exposure or integration time. During the integration period the earth rotates and the baseline position shifts generating yet another smearing due to the length of the integration time. To avoid the two effects shorter integration time and smaller bandwidths are preferred. However, due to various real world tradeoffs such effects remain and affect the overall quality of the data. A point to note here is that even though the techniques of synthesis imaging are trying to mimc the natural process of the lens, the artificial techniques cannot circumvent the natural laws. Bandwidth smearing is nothing but chromatic aberration as seen by the

optical devices. This is a profound reminder that simulating the natural process invokes underlying laws and effects.

4.2 Mathematical Formalism

In this section we will review and build upon the fundamental mathematical foundations of radio interferometry.

4.2.1 van Cittert-Zernike Theorem

The foundation of radio interferometry is defined by the van Cittert-Zernike theorem. The theorem states that, at large distances the combined wavefront of incoherent sources will appear coherent and is the Fourier equivalent of the intensity of the source. In addition, this mutual coherency is equivalent to the correlation function or the complex visibility measured by a pair of antennas. Thus, it is because of this equivalence of the mutual coherence function to the measured complex visibilities that the Fourier transform of the measured visibilities is equivalent to the intensity map of the sky. This relationship is represented as following,

$$\Gamma_{12}(u, v, \tau = 0) = \int\int_{source} I(l, m)\ e^{-j2\pi(ul+vm)} \mathrm{d}l\ \mathrm{d}m = \mathcal{V}(u, v) \tag{4.1}$$

where,$\Gamma_{12}(u, v, 0)$ is the mutual coherence function, measured at two point 1 and 2, in the u, v coordinates expressed in the units of wavelength, and time offset τ is zero, $I(l, m)$ is the averaged time intensity of the source, in the direction cosines coordinates l, m, and $\mathcal{V}(u, v)$ is the complex visibility as measured by the two antennas. Note that the Equation 4.1 is true only if two conditions are met. One, that the observations are on the uv plane and the w coordinate, see Figure 4.1, is equal to 0. This leads to the measurement of the modified visibility given as $I(l, m)/\sqrt{1 - l^2 - m^2}$. Two, the sky sampled is in a small area. This leads to the third direction cosine $n = \sqrt{1 - l^2 - m^2} \sim 1$.

4.2.2 Coordinate Systems

The coordinate transformation of the antenna array onto the sky defines the visibility sampling function. There are three coordinate systems that specify this transformation process. See the Figure 4.1. The antennas on earth are located on a right-handed Cartesian coordinate system XYZ. The axes X and Y are parallel to the plane of the equator of earth

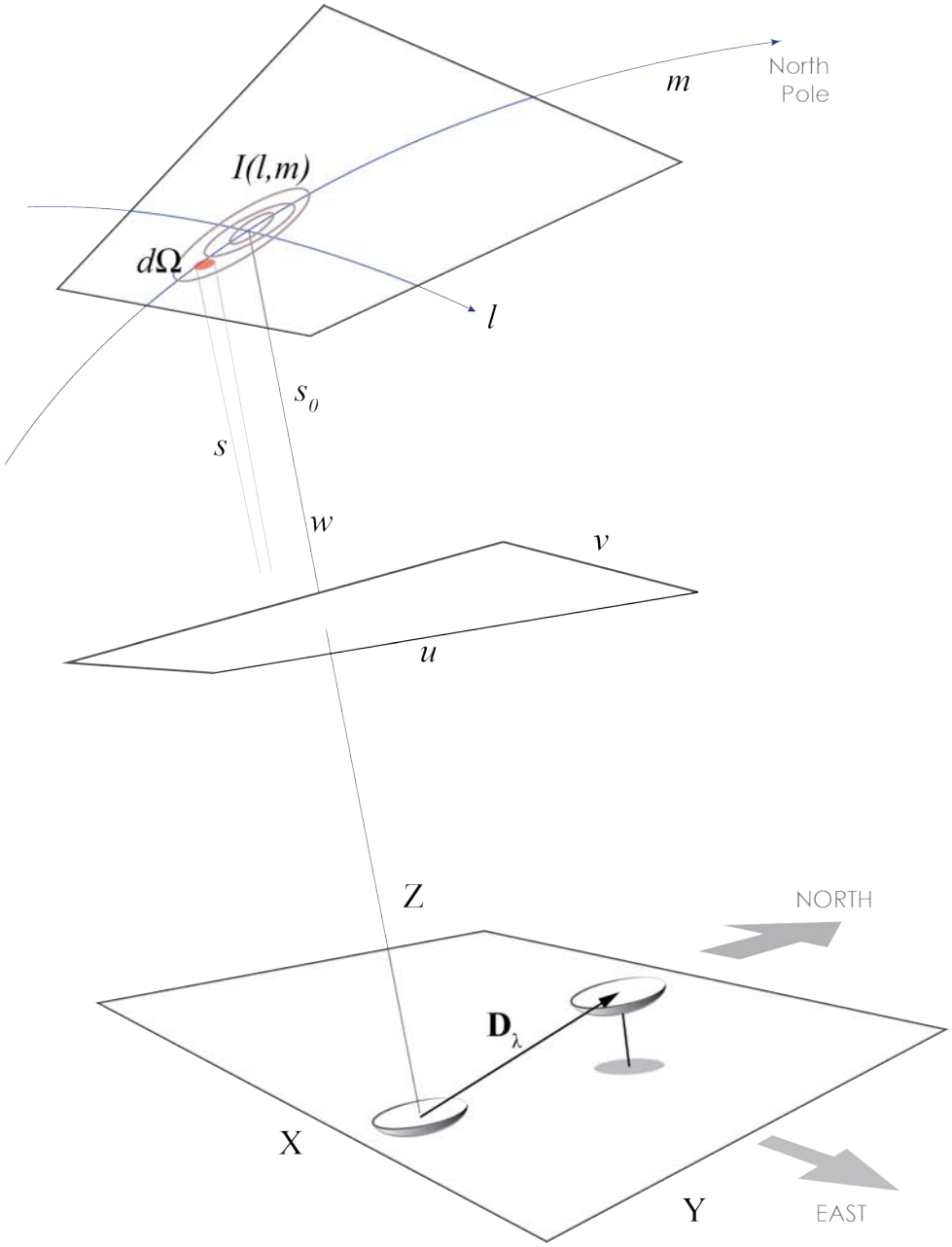

Figure 4.1: The schematic of the Earth, Fourier plane, and sky coordinate systems as used in radio interferometry.

and Z is perpendicular. The X coordinate is measured in the meridian plane (great circle passing through the north and the south poles), the Y coordinate is measured towards the east, and the Z coordinate is measured towards the north pole. The projection of the baselines (vector between a pair of antennas) on the u, v, w plane is given by the relation,

$$\begin{bmatrix} u \\ v \\ w \end{bmatrix} = \begin{bmatrix} \sin H & \cos H & 0 \\ \text{-}\sin\delta\ \cos H & \sin\delta\ \sin H & \cos\delta \\ \cos\delta\ \cos H & \text{-}\cos\delta\ \sin H & \sin\delta \end{bmatrix} \begin{bmatrix} X_\lambda \\ Y_\lambda \\ Z_\lambda \end{bmatrix} \tag{4.2}$$

where, H is the hour angle and δ is the declination of the source, $X_\lambda, Y_\lambda, Z_\lambda$ are measured in wavelength units λ. The intensity $I(l, m, n)$ of the source is measured in direction cosines l, m estimated with respect to the u, v, w coordinates.

4.2.3 Flux Density and Brightness Temperature

The measurements of the electromagnetic radiation in the different parts of the spectrum employ different techniques. For example, in the case of extremely high-energy radiation such as in gamma rays ($> 10^{19}$ Hz), the radiation ionizes the detector material proportionally and consequently is directly/indirectly measured. However, in the low-energy regime of the radio window (3×10^3 to 3×10^{11} Hz) of the electromagnetic spectrum, the wave nature of the radiation is measured. The large collecting metal surfaces focus the incident radiation on the receivers generating proportional voltages.

The radiation from the radio sources are measured in the units of Jansky (Jy), where 1 Jy = 10^{-26} W/m^2/Hz. In other words, for a 1 Jy source the energy per unit frequency (Hz) passing perpendicular through an area of unit square (m^2) is measured at 10^{-26} Watts. The radio sources are usually very weak and therefore a factor of 10^{-26} is utilized for convenience.

While the source intensity may have wide bandwidth, often measured in W/m^2, the radio receivers only detect a fraction of the bandwidth. Therefore, the true measure of the source intensity is per unit frequency, termed as *flux density*, measured in W/m^2/Hz. The *flux density* is a measure of unresolved sources, *i.e.*, the sources with angular sizes smaller than the half-power beamwidth (HPBW) of the radio beam. For the extended

sources the direction and therefore the solid angle subtended by the source (*steradian*) of the radiation becomes important. The measure of the extended source is called *surface brightness*, measured in W/m^2/Hz/sr or flux density per solid angle.

The Planck's black body spectrum relation is given as,

$$B_\nu(T) = \frac{2h\nu^3}{c^2}\frac{1}{e^{h\nu/kT}-1} \qquad \text{W/m}^2\text{/Hz/sr} \tag{4.3}$$

For radio frequencies (very long wavelengths) the exponential term $h\nu/kT$ is very small and therefore is Taylor expanded as,

$$e^{h\nu/kT} \approx 1 + h\nu/kT + ... \tag{4.4}$$

This is know as Rayleigh-Jeans approximation. This approximation relates the black body temperature with the brightness as,

$$B_\nu(T) \simeq \frac{2\nu^2}{c^2}kT = \frac{2kT}{\lambda^2} \tag{4.5}$$

The interpretation of the equation is that for a given source the brightness, $B_\nu(T)$, is proportional to the temperature, T, of a black body at that temperature. However, if the radiation emission mechanism is not black body (thermal) then the temperature will not be the same as the temperature of the source.

4.3 Radio Interferometer Measurement Equation

This section covers the essentials of the mathematical framework called the radio interferometer measurement equation (RIME). The framework was originally proposed by Hamaker et al. [1996] and later expanded by Smirnov [2011a]. The framework employs the 2×2 Jones' matrices [Hurwitz and Jones, 1941, Jones, 1941a,b] to define the complex visibilities from the correlator multiplied by the propagation effects, each represented by their own 2×2 matrix. This elegant and simple framework affords various new insights into radio interferometry, especially in calibration of the direction dependent effects (DDE). Following is a brief outline explaining the fundamentals of the framework.

In Jones' framework, the polarized light is described by a column vector and the optical elements that transform the light are denoted by 2×2 matrices.

Following the said framework, an electromagnetic wave $\mathbf{e}$, traveling along the z axis of the Cartesian xyz coordinate system can be represented as a column vector in its complex parts as,

$$\mathbf{e} = \begin{pmatrix} e_x \\ e_y \end{pmatrix}$$

The transformation of the wave due to various propagation effects represented by Jones' matrices, $\mathbf{J}_n, \mathbf{J}_{n-1}, ..., \mathbf{J}_1$, is then represented as,

$$\mathbf{e}' = \mathbf{J}_n, \mathbf{J}_{n-1}, ..., \mathbf{J}_1 \begin{pmatrix} e_x \\ e_y \end{pmatrix} = \mathbf{J}\mathbf{e} \tag{4.6}$$

Two antennas, p and q, of an interferometer detect the incident wave as voltages v_p and v_q, each with two receivers a and b. The voltages are correlated and output is a visibility matrix (also referred as coherency matrix) defined as,

$$\mathbf{V}_{pq} = 2 \begin{pmatrix} \langle v_{pa} v_{qa}^* \rangle & \langle v_{pa} v_{qb}^* \rangle \\ \langle v_{pb} v_{qa}^* \rangle & \langle v_{pb} v_{qb}^* \rangle \end{pmatrix} \tag{4.7}$$

where, the * denotes the complex conjugate and the $\langle\rangle$ represents the time average of the signal, also known as the integration time. For the detailed explanation of the factor 2 see section 7.2 of Smirnov [2011a]. The above equation can be rearranged as following,

$$\mathbf{V}_{pq} = 2 \left\langle \begin{pmatrix} v_{pa} \\ v_{pb} \end{pmatrix} \begin{pmatrix} v_{qa}^* & v_{qb}^* \end{pmatrix} \right\rangle = 2 \langle \mathbf{v}_p \mathbf{v}_q^H \rangle \tag{4.8}$$

where, the superscript ^{H} is the Hermitian transpose operation.

Now assuming the linearity between the incident wave and the induced voltage, such that, $\mathbf{V} = \mathbf{J}\mathbf{e}$, the equation 4.8 can be rewritten as,

$$\mathbf{V}_{pq} = 2 \langle \mathbf{J}_p \mathbf{e} \, (\mathbf{J}_q \mathbf{e})^H \rangle = 2 \langle \mathbf{J}_p (\mathbf{e} \, \mathbf{e}^H) \mathbf{J}_q^H \rangle \tag{4.9}$$

Further assuming that the Jones terms $\mathbf{J}_p$ and $\mathbf{J}_q$ are time and frequency invariant, the above equation is expanded as,

$$\mathbf{V}_{pq} = 2\mathbf{J}_p\langle(\mathbf{e}\ \mathbf{e}^H)\rangle\mathbf{J}_q^H = 2\mathbf{J}_p \begin{pmatrix} \langle e_x e_x^* \rangle & \langle e_x e_y^* \rangle \\ \langle e_y e_x^* \rangle & \langle e_y e_y^* \rangle \end{pmatrix} \mathbf{J}_q^H \tag{4.10}$$

The matrix term above is equivalent to the Stokes parameters, Hamaker et al. [1996], as shown below,

$$2 \begin{pmatrix} \langle e_x e_x^* \rangle & \langle e_x e_y^* \rangle \\ \langle e_y e_x^* \rangle & \langle e_y e_y^* \rangle \end{pmatrix} = \begin{pmatrix} I+Q & U+iV \\ U-iV & I-Q \end{pmatrix} = \mathbf{B} \tag{4.11}$$

where, I, Q, U, V are Stokes parameters and $\mathbf{B}$ is the brightness of the incident wavefront. More explicitly written, the above relationship equates the complex visibility components to the incident brightness are transformed by the propagation effects represented by the Jones' matrices,

$$\begin{pmatrix} \langle v_{pa} v_{qa}^* \rangle & \langle v_{pa} v_{qb}^* \rangle \\ \langle v_{pb} v_{qa}^* \rangle & \langle v_{pb} v_{qb}^* \rangle \end{pmatrix} = \begin{pmatrix} J_{11p} & J_{12p} \\ J_{21p} & J_{22p} \end{pmatrix} \begin{pmatrix} I+Q & U+iV \\ U-iV & I-Q \end{pmatrix} \begin{pmatrix} J_{11q} & J_{12q} \\ J_{21q} & J_{22q} \end{pmatrix}^H \tag{4.12}$$

Or,

$$\mathbf{V}_{pq} = \mathbf{J}_p\ \mathbf{B}\ \mathbf{J}_q^H \tag{4.13}$$

A few important consequences of the above relationship are obvious. First, the equation separates the antenna based effects into different Jones' terms, *viz.*, $\mathbf{J}_p$ and $\mathbf{J}_q$. This allows for exploring antenna based (direction independent effects - DIE) and direction dependent effects (DDE). This provides a more accurate calibration of the instruments especially for heterogeneous arrays. This is a big step from previous methodologies where the single antenna calibration solutions were applied to the entire array thus only correcting for the direction independent effects. Second, even though the coordinates used in the above derivation were Cartesian xyz, the relationship is independent of the coordinate system. Any transformations arising due to different coordinate systems can be represented as another set of Jones' matrices.

The discussion of RIME formalism will not be complete without mentioning the limitations

and corresponding solutions when considering phased array feeds (PAFs), aperture arrays (AAs), and wide-field polarimetry. These limitations arise from variety of implicit assumptions in the RIME formalism, see Smirnov [2011d]. A tensor based generalized formalism is introduced that captures effects beyond the 2×2 Jones' matrices. In the tensor product form the visibility is then written as,

$$\mathrm{V}_p^q = \mathrm{J}_\alpha^p \; \mathrm{B}_\beta^\alpha \; \bar{\mathrm{J}}_q^\beta \tag{4.14}$$

where, α and β are free indices. The tensor version of the RIME provides a rigorous method to test and extend Jones' matrices, however, for wide range of interferometric applications the 2×2 RIME suffice.

Finally, this elegant framework forms the foundation for new tools badly needed in radio astronomy for simulations and DDE calibration. To address this a directed acyclic graph based tool entitled MeqTrees is developed, Noordam and Smirnov [2010, 2012]. This tool is used for large number of simulations for this research.

Part II

Simulations

Chapter 5

Simulating EoR and Dark Ages

5.1 Simulations

The basic methodologies for the numerical simulations used for this study are discussed in Iliev et al. [2006], Mellema et al. [2006b] and Iliev et al. [2007]. To include the effects due to the LLS, the radiative transfer code is modified as discussed below. In this section, a brief summary of the numerical simulation methodology and the implementation of the LLS models is presented.

5.1.1 CubeP^{3}M - N-body simulations

The evolving matter density fields in a given comoving volume for the desired redshift ranges are generated with the N-body code entitled CubeP^{3}M [Harnois-Déraps et al., 2013]. The evolution of the density fields is based upon the initial conditions specified by the standard Zel'dovich approximation and primordial power spectrum transfer function derived by CAMB[1] [Lewis et al., 2000], originally based on CMBFAST [Seljak and Zaldarriaga, 1996]. The cosmological parameters used are for the flat ΛCDM model of the Universe based on WMAP 5-year data combined with constraints from baryonic acoustic oscillations and high-redshift supernovae, given as, $(\Omega_{\rm M} = 0.27, \Omega_\Lambda = 0.73, h = 0.7, \Omega_b = 0.044, \sigma_8 = 0.8, n_s = 0.96)$. To ensure against numerical artifacts [Crocce et al., 2006] the initial conditions are generated at sufficiently high redshift (here $z_i = 300$).

The CubeP^{3}M code is public domain N-body code designed for simulating large-scale cosmological systems. The code is accurate, efficient, scalable, and parallel across

[1] http://camb.info

box size h^{-1} Mpc	$N_{\rm part}$	mesh	spatial resolution h^{-1}kpc	particle mass $10^6 M_\odot$	$\min(M_{\rm halo})$ $10^8 M_\odot$
114	3072^3	6144^3	1.86	5.47	1.09

Table 5.1: The N-body simulation parameters for the two volumes.

distributed (MPI) and shared (OpenMP) memory systems. The underlying N-body algorithm estimates short-range (sub-grid distances) gravitational forces using the particle-particle (P-P) method. While for the long-range forces, a 2-level particle-mesh (PM) method is applied. Computationally, in comparison to the P-P method which is of the order $O(N^2)$, the P^{3}M method has significantly lower overhead and is of the order $O(N \log N)$, where N is the number of particles.

For the current study, two sets of comoving volumes of sizes, 37 h^{-1} Mpc and 114 h^{-1} Mpc , are simulated. The same N-body simulations were presented in detail in [Iliev et al., 2012]. Here the smaller volume, 37 h^{-1} Mpc , is primarily used for testing and validation purposes only. The simulations for 114 h^{-1} Mpc use $3072^3 \approx 28.9$ billion dark matter particles distributed in 6144^3 mesh cells. While for the 37 h^{-1} Mpc volume, 1024^3 particles are used within 2048^3 mesh. Each particle has mass of $5 \times 10^6 M_\odot$. Through the simulation steps as the structures start to form, the halos are identified using a spherical overdensity halo finder with overdensity parameter of $\Delta = 178$ with respect to the mean density. The halos with more than 20 particles ($M > 10^8 M_\odot$) are considered resolved. The number density of the halos increases for lower redshifts and the mass function approaches the Sheth-Tormen mass function. Iliev et al. [2006] and Watson et al. [2013] provide detailed fits to the high-redshift halo mass function.

5.1.2 C^2-Ray - Radiative Transfer

The second stage of the simulation performs radiative transfer using the C^2-Ray (Conservative, Causal Ray-Tracing) code [Mellema et al., 2006a]. The conservative part of the code ensures spatial and temporal photon conservation, while the causal ray-tracing is implemented using the short-characteristic method.

The C^2-Ray implements a discrete spatial and temporal version of the ionization rate equation [Osterbrock, 1989],

$$\Gamma(r) = \frac{1}{4\pi r^2} \int_\nu \frac{L(\nu)\sigma(\nu)e^{-\tau(\nu,r)}}{h\nu}\, d\nu \tag{5.1}$$

where,$\Gamma(\ r)$ is the ionization rate at distance r from the hydrogen ionizing source, L_ν is the spectral energy distribution of the ionizing source at frequency ν, σ_ν is the cross-section for the ionizing photons, and τ_ν is the frequency dependent optical depth of the hydrogen gas.

Due to the spatial discretization of the computational domain, we do not know τ_ν as a continuous function of position. As was shown in Abel et al. [1999], the photo-ionization rate of one cell whose center has a distance r from the source can be calculated as,

$$\Gamma = \frac{\dot{N}(r - \frac{\Delta r}{2}) - \dot{N}(r + \frac{\Delta r}{2})}{n_{\mathrm{H\,I}} V_{\mathrm{shell}}} \tag{5.2}$$

where, V_{shell} is the volume of the spherical shell with radius r and width$\Delta\ r$, the shell is filled with neutral hydrogen of number density n_{HI}, $\dot{N}(r - \Delta r/2)$ is the rate of ionizing photons arriving and $\dot{N}(r + \Delta r/2)$ the number of photons leaving this shell.

Since,

$$\dot{N}(r) = \frac{1}{4\pi r^2} \int_\nu \frac{L(\nu)e^{-\tau(\nu,r)}}{h\nu}\, d\nu, \tag{5.3}$$

the Equation 5.2 implies that the local photo-ionization rate Γ depends on the difference between $\tau_{\mathrm{in}} \equiv \tau(r - \frac{\Delta r}{2})$ and $\tau_{\mathrm{out}} \equiv \tau(r + \frac{\Delta r}{2})$. In Section 5.1.4 we explain how these optical depths are modified to include the effect of LLS.

In our reionization model, the ionizing luminosity of the collapsed halos is proportional to their mass M. Each halo produces a number of photons,

$$N_\gamma = \frac{f_\gamma M \Omega_b}{\Omega_0 m_p} \tag{5.4}$$

for every n-body output of$\Delta\ t\ =\ 11.46$ Myr. The efficiency factor f_γ is the product $f_{esc}f_\star N_\star$, where, f_{esc} is the ionizing photon escape fraction, $f_\star$ is the star formation efficiency, and $N_\star$ is the number of ionizing photon per stellar atoms, and m_p is the proton mass. The parameter $N_\star$ depends on the initial mass function (IMF) of the stellar population producing the ionizing radiation. Its value for a Pop II population (Salpeter IMF) is ∼4000 and for a Pop III population (top-heavy IMF) it can reach ∼100,000. Due to the uncertainties in f_{esc} and $f_\star$, the value of f_γ is not well constrained. In this study we use 10 for high mass halos (HMACH: High Mass Atomicaly-Cooling Halos) and 150 for low mass halos (LMACH: Low Mass Atomicaly-Cooling Halos), see Table 5.2. The higher value for the LMACHs is motivated either by a larger contribution of metal-free/poor stars or by a larger escape fraction. The LMACHs are also assumed to be susceptible to negative radiative feedback. When the cell in which an LMACH is present is ionized at the start of a new 11.46 Myr time step, the LMACH will not produce any ionizing photons.

From previous work we know that the efficiency factors chosen result in reasonable reionization history in accord with the WMAP optical depth value.

box size h^{-1} Mpc	f_γ HMACH	f_γ LMACH	RT grid
114	10	150	256^3

Table 5.2: Simulation parameters for the 114 h^{-1} Mpc box with LLS. f_γ is the star formation efficiency for high and low mass, and RT grid is the coarser grid for radiative transfer ray-tracing. The underlying cosmology uses the WMAP 5-year results.

5.1.3 Simulating the Effects of Lyman Limit Systems

It is thought that the LLSs correspond to the denser, ionized halos of the collapsed objects which, although ionized, have a high enough column density of H I to result in an optical depth > 1. Therefore, the effect of the LLS, is physically better described by a recombination process than that of an absorber. Recombinations by dense structures below the resolution limit of the code are described with clumping factors. This has for example been the approach of Sobacchi and Mesinger [2014].

Introducing a clumping factor, however, does not directly yield the value of the mean

free path (mfp) and in general it is not clear how to exactly assign the clumping factor for different redshifts and different environments. Therefore, for this study we decided to work directly with the mfp. This is similar to prior work by Alvarez and Abel [2012] with the difference that in the prior studies the mfp was implemented as a hard boundary which photons could not cross. Instead, in our implementation, the mfp is employed to define a global ionizing photon absorbing component which after one mean free path reaches an optical depth of 1.

The advantages of working with the mfp directly is that it is easier to connect the effect on the sizes of H II regions to the imposed mean free path. It also allows the use of published mfp expressions. The disadvantage, on the other hand, is that the mfp in the ionized medium is not a measured quantity beyond $z = 6$. Therefore, we extrapolate from the lower redshift results. To the extent that the ionized regions during reionization can be viewed as being locally post-reionization, there is some justification in performing this extrapolation. The additional absorption our LLS component adds in the fully neutral regions is marginal, and therefore only affects the already ionized regions. Also when introducing a clumping factor similar uncertainties about the behavior into the Epoch of Reionization play a role.

To perform the extrapolation of the mfp beyond $z = 6$, we use the parametrization given by Songaila and Cowie [2010]. Based upon the observational data, the number density of the LLSs per unit redshift path dz is parametrized as,

$$f(N_{\rm HI}, z) = f(N_{\rm HI}, z = 3.5) \left(\frac{1+z}{4.5}\right)^{\gamma} \tag{5.5}$$

where, $f(N_{\rm HI}, z = 3.5)$ is the number density at $z = 3.5$. Estimating the log-likelihood function for the entire redshift range of $0 < z < 6$ in Songaila and Cowie [2010] yields the values for the parameters to be, $f(N_{\rm HI}, z = 3.5) = 2.8 \pm 0.33$ and $\gamma = 2.04^{+0.29}_{-0.37}$. Furthermore, in the approximation that the column density function $f(N_{\rm HI}, z)dN_{\rm HI} \propto N_{\rm HI}^{-\beta} dN_{\rm HI}$ [Petitjean et al., 1993], the mean free path is related to the number density

as, [Miralda-Escudé, 2003],

$$\ell(\nu_0, z) f(N_{\rm HI}, z) \propto \frac{\int_a^\infty \tau^{-\beta} d\tau}{\int_0^\infty \tau^{-\beta}(1 - e^{-\beta}) d\tau}$$
$$\text{or,} \quad \ell(\nu_0, z) = \frac{a^{1-\beta}}{\Gamma(2-\beta)} \frac{c}{H(z)(1+z) f(N_{\rm HI}, z)} \tag{5.6}$$

where, $f(N_{\rm HI}, z)$ is measured above the column density $N_{\rm HI}$ corresponding to a value a for the optical depth (here, $a \approx 1$), τ is the optical depth at the Lyman limit, and ν_0 is ionization edge frequency. Here, Γ is the gamma function and not the ionization rate [Songaila and Cowie, 2010].

In order to test the impact of different evolutions of the mean free path we use two different extrapolations, one using the parameters given by Songaila and Cowie [2010] and the other using parameters derived from fitting the curve in the inset of Figure 1 in McQuinn et al. [2011]. The simulations for these two choices are labeled as LLS1 and LLS2, respectively and the parameters used are listed in Table 5.3. The evolution of the mean free path for these two sets of parameters is shown in Figure 5.1. LLS2 has substantially smaller values of the mfp through the reionization epoch. The figure also shows the values of the mean free path at different redshifts below 6 as estimated by Songaila and Cowie [2010] (using $\beta = 1.28$ and $\gamma = 1.94$ in their Equation 7).

From Figure 5.1 it is evident that both extrapolations result in very small mfps at very high redshifts. Below our cell size it does not make sense to implement the LLS model as we already use an assumed escape fraction for absorptions within the source cell. As we want to concentrate on how the LLSs impact the later stages of reionization when the ionized regions have reached sizes of 10-20 cMpc, we chose to only switch on our LLS absorption if the mean free path is larger than 5 grid cells (3 cMpc). This occurs around $z \sim 15$. We found that this choice did not impact the evolution around this transition redshift.

5.1.4 LLS implementation in C^2-Ray

To include the effects of LLS in the radiative transfer calculation, an additional optical depth term, $\tau_{\rm LLS}$, is added. The implementation of the additional optical depth is based

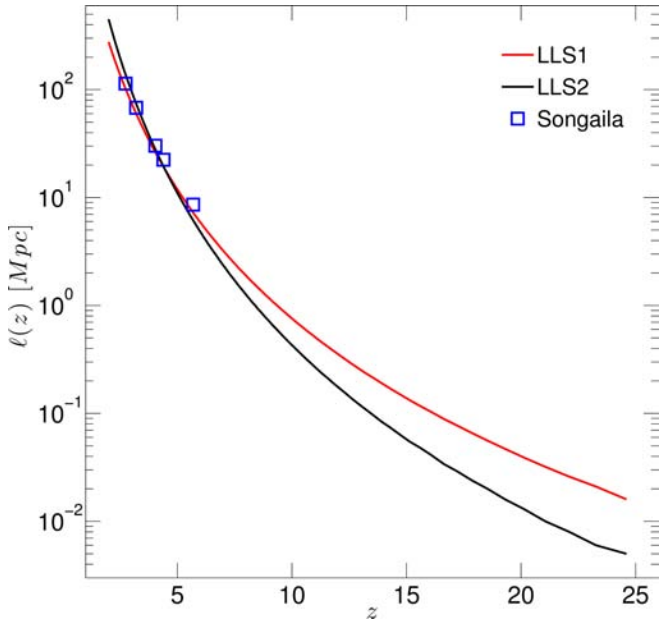

Figure 5.1: The mean free path (in $\log_{10}$ scale) of the ionizing photons for the two LLS models, LLS1 (Songaila, red), and LLS2 (McQuinn, black) in proper Mpc, see Equation 5.6. The blue squares are the data points computed from Equation (7) of Songaila and Cowie [2010] using the maximum likelihood estimate of $n_{\rm LLS}$ in the redshift bins. The parameters are listed in the Table 5.3.

Simulation	Model	γ	$f(N_{\rm HI}, z_{\rm x})$	$z_{\rm x}$	β
LLS1	Songaila *et al.*	2.04	2.84	3.5	1.28
LLS2	McQuinn *et al.*	2.85	2.34	3.5	1.30
L1	No LLS	-	-	-	-

Table 5.3: Simulation parameters for the two LLS models LLS1 and LLS2. In the model L1, the case without LLS, the simulation is not affected by LLS.

upon the notion that after one mean free path, $\tau_{\rm LLS}$ acquires the typical value of the optical depth of a Lyman-limit system at the Lyman limit. For the purpose of this paper we assume that each cell contributes equally to $\tau_{\rm LLS}$ with a valueΔ $\tau_{\rm LLS}$. One could envisage algorithms that vary this quantity depending on the density field but for this paper we selected the simplest assumption of a uniform 'mist' of the LLSs.

As explained in Section 5.1.2, C^2-Ray uses two optical depth values for each cell, $\tau_{\rm in}$, the optical depth between the source and the entry point of the ray into the cell, andΔ τ, the optical depth of the ray section that is contained within the cell. The difference between these two values is used to calculate the ionization rate Γ in the cell, using Equation 5.2. In principle one could addΔ $\tau_{\rm LLS}$ toΔ τ but this would then impact Γ which would give

incorrect results. The fundamental purpose to implement the subgrid LLS model is to remove (absorb) photons due to LLS without impacting any other parts of the radiative transfer calculation.

For two cells, n and $n+1$, with the same ray crossing their centers, $\tau_{\rm in}^{n+1}$ is equal to $\tau_{\rm out}^{n} \equiv \tau_{\rm in}^{n} + \Delta\tau^{n}$. To include the LLS optical depth this equality is changed to

$$\tau_{\rm in}^{n+1} = \tau_{\rm out}^{n} + \Delta\tau_{\rm LLS}\,. \tag{5.7}$$

This effectively adds the additional optical depth in between the two cells which means that it is not used in the calculation of Γ for a cell. A simple schematic of this process is shown in the Figure 5.2.

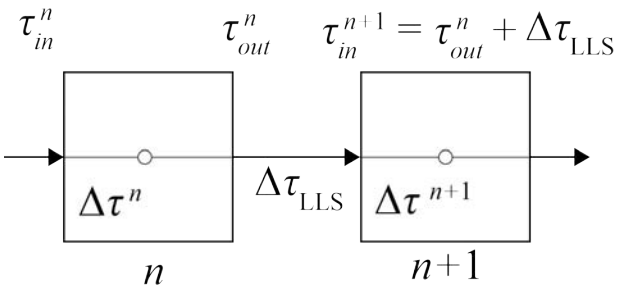

Figure 5.2: The schematic of the C^2-Ray optical depth estimation.

As the ray traverses through the cell n, the ionization rate Γ in the cell is estimated as the difference of the incoming optical depth τ_{in}^{n} and the optical depth in the cell$\Delta\ \tau^{n}$. The outgoing optical depth of the cell n is then the incoming optical depth of the next cell $n+1$. However, in the case of LLS, the new incoming depth of the cell $n+1$ is further added with the optical depth due to the LLS. As a result, as shown in the figure, the incoming optical depth for the cell $n+1$ is $\tau_{out}^{n} + \Delta\tau_{\rm LLS}$.

The column density per cell is estimated as,

$$f(N_{\rm HI}, z) = \frac{\tau_{\rm LLS}}{\sigma_{\rm H}}\ n_{\rm LLS} \tag{5.8}$$

where, $\sigma_{\rm H} = 6.30 \times 10^{-18}{\rm cm}^2$ is the photon cross section of a hydrogen atom at energies above the Lyman limit, $\tau_{\rm LLS} = 2$, and $n_{\rm LLS}$ is the inverse of the distance between LLSs.

The mean free path is then estimated as,

$$\ell(z) = \frac{V_{\rm cell}(z)}{n_{\rm LLS}} \frac{1}{\rm Mpc} \tag{5.9}$$

For the cells whose centers do not lie on the same ray, the short characteristic ray tracing algorithm constructs $\tau_{\rm in}$ through interpolation of the relevant $\tau_{\rm out}$. The above modification works equally well if one replaces each $\tau_{\rm out}$ by $\tau^n_{\rm out} + \Delta\tau_{\rm LLS}$.

To calculate the value ofΔ $\tau_{\rm LLS}$ we use the value of $\ell(\nu_0, z)$ from Equation 5.9. If the proper cell size is given byΔ x then the contribution of every cell is estimated as,

$$\Delta\tau_{\rm LLS} = \tau_{\rm LLS}\frac{\Delta x}{\ell(\nu_0, z)}\,. \tag{5.10}$$

We use the value of $\tau_{\rm LLS} = 2$.

As explained in Section 5.1.3, this additional optical depth is only applied when $\ell(\nu_0, z) >$ 3 cMpc. For smaller values we setΔ $\tau_{\rm LLS}$ to zero.

5.1.5 Ray-Tracing in C^2-Ray

This is brief overview of the implementation of the ray-tracing in C^2-Ray. For details see Mellema et al. [2006a]. The method of ray-tracing is used to simulate the transportation of the ionizing radiation across the simulation volume. The simulations are temporally iterative and require the iteration stepΔ t to be small enough so that variables of interest such as the time-averaged optical depthΔ $\tau(\nu)$ through the cell remain invariant. In the simulations for the volume 162.8 Mpc theΔ t = 11.6 Myr. This is based on the criteria described in Mellema et al. [2006a] such that the ionization rate is defined as,

$$\frac{{\rm d}y_{\rm HI}}{{\rm d}t} = -\langle\Gamma\rangle\ y_{\rm HI} \tag{5.11}$$

where, $y_{\rm HI}$ is the neutral fraction of hydrogen and $\langle\Gamma\rangle$ is the time-averaged photoionization rate. The relationship indicates that ionization rate is only dependent on the photoionization rate and therefore could be assumed as constant in the time step.

Now, let us consider a given volume (for example 162.8 Mpc) of neutral hydrogen density field in which for simplicity after some time (each iteration of 11.6 Myr) only two sources form at diagonally opposite corners of the cube. The number of photons emitted by these sources per time iteration depends on their masses and ages. The light rays are traced from these sources traversing radially outwards. The tracing of the rays defines the long- and short-characteristic ray-tracing. In the long-characteristic ray-tracing the rays are cast from the source to each cell in the simulation volume. As an aside, each ray is independent and therefore a good candidate for parallelism. However, since each cell must be reached by at least one ray, the cells closer to the source are crossed by rays far many times than the cells father out. This can be easily visualized in 2D as the density of the spokes of a wheel closer to the center. This results in oversampling of the cells closer to the source and thereby computationally redundant. Abel and Wandelt [2002] introduced adaptive ray-tracing to mitigate redundant calculations. Mellema et al. [2006a], however, impelmented the short-characteristic method of ray-tracing to solve the same issue. In the short-characteric ray-tracing the a single ray is cast to the center of the cell, but importantly, in the next time step only the ray in the previous cell is used to estimate the optical depth as discussed in 5.1.4. The rays represent traveling photons. Depending on the set boundary conditions (periodic or not), the photons could travel out of the box or reenter from the other side. As the stream of photons encounter the very first cell, the optical depth of the cell defines how many are going to exit the cell which in turn gives the ionization rate of the cell. The key part to this calculation is the geometry. The $\tau(\nu)$ of the cell is weighted by the path length the ray takes as it traverses across the cell. The extreme case being the diagonal of the cube, in which case the weight is one. The number of photons entering a cell is related to the column density to the cell. For the details of calculating the column density see Appendix A of Mellema et al. [2006a]. A 2D version is shown in the Figure 5.3.

The ray from the source are cast to the centers of the cells m and n. For the cells m and n, the geometry of the entering ray in orientation with the cell dictates the weight of the path length ds. While for cell m it is almost diagonal, it is parallel for the cell n. In addition, the different optical depth of each cell combined defines the ionization of the cell as the rays traverse across the cube.

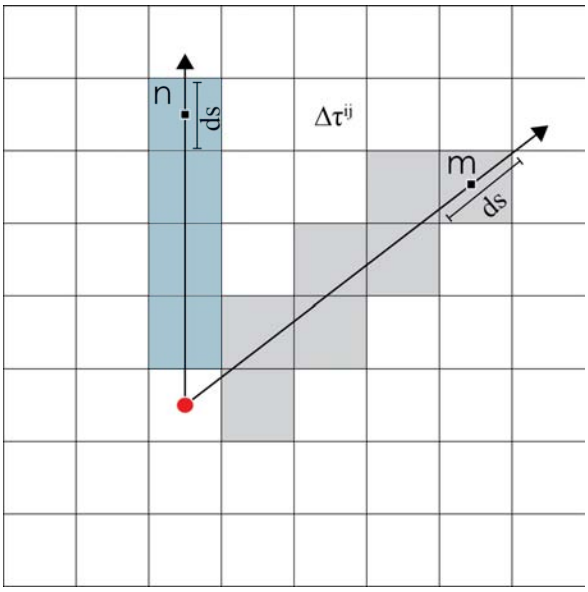

Figure 5.3: The 2D schematic of the short-characterictic ray tracing.

For illustrative purposes, the program data flow for the LLS implementation is shown below,

```
1  Define LLS model (Songaila, McQuinn, Prochaska, ...)
2  Define LLS distribution
3  Initialize LLS
4
5  Loop over redshifts
6        Evolve cosmology per redshift
7        Estimate column density and mfp per cell due to LLS
```

For a given model, the LLS are distributed in the simulation volume. In our case we used uniform distribution as the extreme case. Once the threshold mfp is crossed the column density and mfp per cell is estimated. For the next generation of simulations the distribution model specially based upon the new observational data (if available) will be implemented and differentiated.

Chapter 6

Simulating Interferometry Measurements (SIM)

In the previous Chapter 5, we have used N-body and radiative transfer methods to build the evolution of the cosmological density fluctuations and the ionization field. Now we want to examine how the fluctuations appear in the form of the signal to the radio interferometers. This cosmological signal, as it traverses across the Universe, is corrupted by wide variety of mitigating effects including astrophysical (free-free and diffuse Galactic foregrounds, extra-galactic foregrounds), non-astrophysical (Faraday rotation, ionosphere), and instrumental (thermal noise, gains, direction dependent and independent effects). These effects are 5-6 orders of magnitudes brighter than the cosmological signal, thus making the task of designing the radio telescope arrays and defining the observational strategies, challenging. Realistic simulations of these effects, therefore, are critical in testing the efficacy of various techniques proposed to achieve the science goals for various experiments. There are many methodologies employed to model the propagation effects. However, more realistic solutions tend to fall in the numerical simulations category and consequently lead up to computational challenges.

This chapter discusses the development of the end-to-end simulation tool entitled, Simulating Interferometry Measurements (SIM). SIM is a software framework that consolidates CubeP^{3}M, C^2-Ray, and MeqTrees with various layers of middleware developed for this research. The term framework here is not used in the strictest sense as applied in

computer science (CS). Rather, it represents a codebase that in the future will be converted into a real framework. From the strictest CS definition, a framework is a codebase that extends API (applications programming interface) to enrich the functionality of the code without exposing the `main()`. The good examples of frameworks in scientific computing are GAMER framework for adaptive mesh refinement [Shukla et al., 2011] and Cactus framework [Löffler et al., 2012] used for numerical relativity.

To test and establish the effectiveness of SIM framework, the results are validated against existing expectation values from LOFAR telescope before extending it to SKA-class telescopes. In the Part III of this thesis SIM is used to derive science parameters as basic examples. It is evident that such tools are becoming essential in the upcoming array development process. The tools are at early stages and will require advanced software engineering and high-performance computing compliance to scale.

6.1 Significance of SIM

The current and upcoming radio interferometer telescopes around the world are at the technological frontier. The scientific objectives of the telescopes are driving the costs of data processing to unprecedented petascale and exascale regimes. During the exascale panel discussion at the Supercomputing Conference 2010 in New Orleans LA, the two applications that were recognized by the panel of experts as baseline exascale candidates were human brain simulation and Square Kilometer Array (SKA) [SKA] telescope. The roadmap leading to SKA and exascale computational challenge is punctuated with near-term telescopes with petascale requirements, namely, Atacama Large Millimeter/Sub-millimeter Array (ALMA) [ALM], extended Very Large Array (eVLA) [eVL], Low Frequency Array (LOFAR) [LOF], Australian SKA Pathfinder (ASKAP) [ASK], to name a few.

With massive data throughput, the traditional techniques for data transport, processing and analysis will no longer suffice. The in-depth studies of scalable algorithms, processing paradigms, complete pipelines and underlying computational architectures etc. are imperative. The telescope design and data processing are tightly coupled. The end-to-end large-scale modular simulations provide a constructive test-bed for research and

development of novel effective and optimal algorithms and solutions.

There is an obtrusive dearth of clearly defined and standardized infrastructure to address these issues. The end-to-end SIM consists of entire dataflow from the science data simulation to analysis. While stage-based studies may be performed, a combined framework affords understanding of interaction and interdependence of various parameters in the entire dataflow. Moreover, the pipeline simulation allows for systematic exploration of array configurations and their impact on the success of present and upcoming telescopes. Such a framework is computationally challenging, however, output of the simulations generate quantifiable boundary conditions for the experimental phase-space enabling discovery. The interplay of the parameters is complex and therefore is best suited for a simulation studies. The simulations have enabled in making the first generation of statistically meaningful predictions.

The SIM is extremely timely, given that LOFAR is currently online and collecting data, while the SKA-class telescopes are gearing up in their different phases of construction. The SIM simulations are based upon well-tested methods. The recent significant new developments, both scientific and numerical, which go far beyond anything attempted to date, are incorporated in SIM namely,

(i) Handling very large volumes with tens of millions of sources with radiative transfer. This is a crucial development for modeling realistic signals. Especially, since it is for the first time that the full EoR survey volumes are simulated with precision. Previous efforts had to resort to much smaller volumes, or to less precise semi-analytical studies.

(ii) Extremely large dynamic range including all active sources, down to mini-haloes, which are typically neglected, in a dynamically self-regulated and self-consistent large-scale simulation.

(iii) Simulating the early fluctuating X-ray background in proper EoR context. Each of these advances by itself re-defines the state-of-the-art in reionization simulations and has the potential to transform our understanding of this epoch.

(iv) Complete instrumental response simulation using the state-of-the-art RIME framework.

(v) Including complete foregrounds and instrumental effects to test calibration limits to recovering the EoR signal.

The SIM framework provides a flexible mechanism to conduct studies to test the efficacy of the instruments and various analyses methodologies, thus allowing the fine-tuning of the science and technology requirements of the experiments. However, like most of the models, there are limitations due to assumptions. The key, however, is to minimize the errors due to assumptions within the desired error budgets and conduct the studies. The Part III of this thesis demonstrates a few basic studies possible with SIM. More intricate studies with SIM are proposed in end as future work outside the scope of this research. The following section provides and overview of SIM.

6.2 SIM Overview

The SIM software framework has four primary software component layers, as shown in the Figure 6.1, Cosmological Data Layer, SIM middleware, Meqtrees, and Analysis. Some of these layers are high-performance computing compliant. In other words, the codes are capable of running on supercomputers. The Cosmological Data layer, for example, uses OpenMP and MPI to distribute the load across the cluster. In addition, MeqTrees and parts of the Analysis layer are also HPC compliant. MeqTrees runs on multicores and at the writing of this thesis has been tested on a cluster. Most of these codes are both compute and memory intensive. For example, for 114 h^{-1} Mpc sized volume C^2-Ray takes about 60 system hours with 512 MPI tasks on heterogeneous cluster like Stampede (TACC) which has 6400 nodes each with two Xeon E5-2680 processors and one Intel Xeon Phi SE10P Coprocessor (on a PCIe card). In the host-device layout, the host is configured with 32GB of memory with an additional 8GB of memory on the device. The code progressively slows as the number of the ionizing sources increase at late times. The total data volumes for the 114 h^{-1} Mpc are of the order of 60 GB with the output only ranging from 20 GB. Expectedly, for larger volumes, for example 425 h^{-1} Mpc , the total data sizes are of the oder of 800 GB with results only at 200 GB. It should be noted that this is after significant reduction in the resolution for ray tracing; a step that decreases the dynamic

range of the simulation and also mitigates the capability to explore small scale physics. Emerging compute architectures, such as accelerators (Graphics Processing Units (GPUs) and Xeon Phi), are effective in compute efficient for ray-tracing type algorithms. There is an attempt underway to map the ray-tracing algorithms on accelerator programming models within the codes.

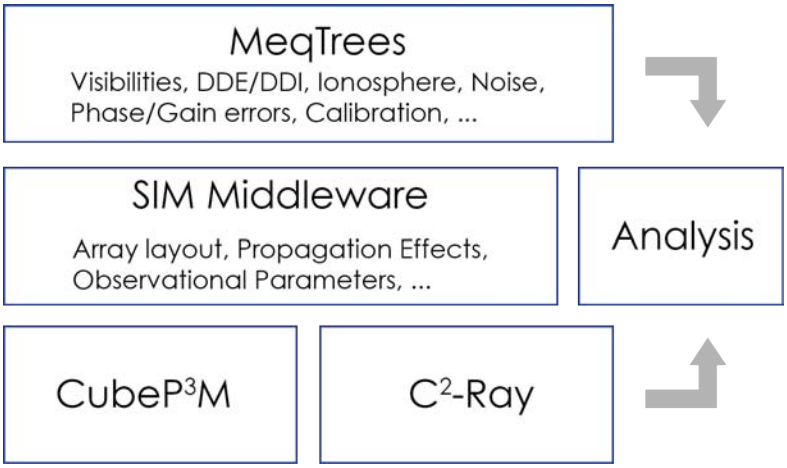

Figure 6.1: The schematic layout of the SIM framework.

6.2.1 Cosmological Data Layer

The bottom most layer of Figure 6.1 is the cosmology data layer that comprises of CubeP^{3}m and C^2-Ray codes. This layer generates the cosmological data. Based upon the defined cosmology the layer generates coeval boxes for a given redshift range. In the case of most ionization studies the redshift ranges are $6 < z < 25 - 30$. The N-body code is run separately and the catalog of the halos are generated. Theses halos are the sources of ionizing photons for the simulation. The density fields are then convolved with a larger kernel to lower resolution. Thereafter, based upon the source (halo) masses the ionization photons are propagated in 3D comoving volumes and the ionization history is estimated for defined time steps. As mentioned above, the data volumes are relatively large. The C^2-Ray code also has checkpointing mechanism built in. Checkpointing is a fault-tolerance methodology used in HPC where the state of the run are saved to a point so that it is possible to recover from any unprecedented fault(s). This method also affords flexibility to the code whereby entire simulation run may be executed semi-contiguously. The coeval reionization boxes once ready are piped into analysis or prepared for observational run and piped through the SIM middleware.

6.2.2 SIM Middleware

The SIM middleware is a collection of codes written in C/C++, FORTRAN, Python, Matlab, and IDL to facilitate intermediate steps required for the end-to-end simulations. The middleware is a large part of SIM and solely developed for this research. The multi-language choice was largely necessitated by the data output formats and in some cases available solutions. The next version of SIM shall have license-free middleware with focus on mitigating the platform dependence. Based upon the functionality, the middleware is divided into the following broad categories - Cosmological Parameter Estimation, Signal Preparation, Antenna Configuration, Coordinates Conversions, Measurement Sets, Analyses and Visualization. In the following sections we will elaborate on the disparate layers of the SIM middleware.

Sky Projection

The co-moving volumes from the Cosmological Data Layer roughly range from redshifts $6 < z < 25 - 30$ for every 11.5 Myr time interval. Based upon the observational frequency of study/interest a cube that closely corresponds is selected. This cube has a physical comoving size of 114 or 425 h^{-1} Mpc . The cube subtends a solid angle on the sky at a given redshift. The depth of the cube is represented as the bandwidth in terms of redshifted 21-cm. The angular size of the cube in the sky is then,

$$\Delta\theta_{\mathrm{box}} = \frac{\mathrm{L\ [Mpc]}}{D_{\mathrm{A}}\ (1+z)} \qquad \mathrm{[radians]} \tag{6.1}$$

where, L is the proper length of the box on the side in Mpc, and D_{A} is the angular diameter distance. The bandwidth along the axis of redshift is given as,

$$\Delta\nu_{\mathrm{box}} = \frac{\nu_0\ \mathrm{H}(z)\ \mathrm{L}}{c\ (1+z)^2} \qquad \mathrm{[MHz]} \tag{6.2}$$

where, ν_0 is the rest frame frequency, 1420.4 MHz, and $\mathrm{H}(z) = \mathrm{H}_0\ (1+z)^{3/2}\ \sqrt{\Omega_m}$. The number of pixels on the side of the simulation volume decide the resolution in the angular and frequency units. For example, for the comoving volume of 425 h^{-1} Mpc at $z = 8.515 (\nu_{\mathrm{obs}} \sim 150$ MHz) the angular size is$\Delta\ \theta = 3.74^\circ$ and the bandwidth is $\Delta\nu_{\mathrm{box}} = 34.38$ MHz. For 504 pixels on the side, the angular resolution per pixel is $26.73''$ and the frequency channel resolution per pixel is 68.21 kHz.

Signal Preparation

The coeval volumes are ionized fractions of the neutral hydrogen and must be converted to brightness temperature before it could be used for observation. The conversion mechanism requires the underlying density. The SIM middleware converts the ionized fractions into temperature (K) and brightness (Jy). The data is zero-mean corrected before it is converted to physical units. The conversion relation is defined as the differential brightness temperature with respect to CMB ($T_{\rm CMB}$) given as,

$$\begin{aligned} \delta T_{\rm b} &= \frac{T_{\rm S} - T_{\rm CMB}}{1+z}\,(1 - e^{-\tau}) \\ &\approx \frac{T_{\rm S} - T_{\rm CMB}}{1+z}\,\frac{3\lambda_0^3 A_{10} T_\star n_{\rm HI}(z)}{32\pi T_{\rm S} {\rm H}(z)} \qquad [{\rm mK}] \end{aligned} \tag{6.3}$$

where, $T_{\rm S}$ is spin temperature [Field, 1959], τ is the corresponding 21-cm optical depth at redshift z, λ_0 is rest-frame wavelength of the hydrogen line, A_{10} is the Einstein's A coefficient, $T_\star$ is the energy difference between the two hyperfine levels ~ 0.068 K, and $n_{\rm HI} = (1+\delta)\langle n_{\rm H}\rangle$ is the mean number density of the neutral hydrogen. The brightness temperature is converted to Jy by the simple relation $2k_{\rm B}T\theta^2/\lambda^2$.

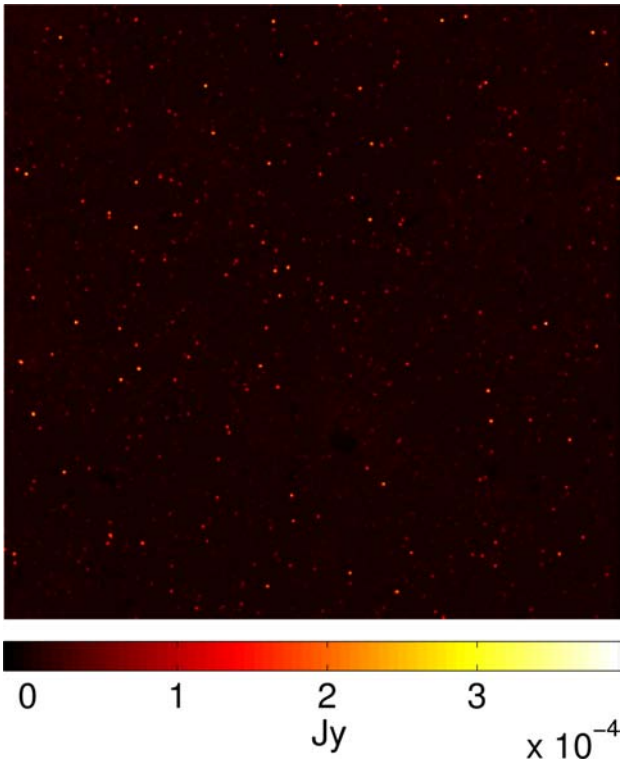

Figure 6.2: The 1 MHz bandwidth signal including the EoR, extragalactic, and Galactic foregrounds at $z = 8.515$. The side of image is$\Delta\ \theta = 3.74^\circ$ and 425 $\rm h^{-1}$ Mpc . The image is 504$\times$ 504 pixels.

The comoving volume is integrated to generate 1 MHz equivalent bandwidth. Unless explicitly specified all the studies in this research use the 1 MHz channel to study the effects. This is primarily due to data sizes and computation overload. When testing for channel dependent effects multi-channel approach is more suitable. The extragalactic and Galactic foregrounds are re-gridded to match the pixel sizes and numbers of the ionized fraction data. The foregrounds are originally in mK units and therefore are converted to Jy. The 1 MHz channels are integrated from the foregrounds as well. At this stage there are three 1 MHz datasets in Jy, namely, EoR signal, extragalactic foregrounds, and Galactic foregrounds, that map one-to-one. Simple integration of the channels gives the sky signal, see Figure 6.2. The figure shows the 1 MHz bandwidth signal including the EoR, extragalactic, and Galactic foregrounds at $z = 8.515$. The side of image is$\Delta\,\theta = 3.74°$ and 425 h^{-1} Mpc . The image is 504$\times$ 504 pixels.

Extragalactic and Galactic Foregrounds

The very first propagation effects that distort the redshifted 21-cm signal are the extragalactic foreground followed by the Galactic foreground. The foreground models used in the SIM simulations are from Jelić et al. [2010]. The foregrounds from Jelić et al. [2010] are $5° \times 5°$, 0.5 MHz wide, 200 channel cuboids. The cuboids represent the extragalactic foreground, the galactic synchrotron, and galactic free-free emissions. There are two separate models for the Galactic foregrounds. The foreground data is in the units of Kelcin. The SIM middleware remaps the foregrounds to the angular size of the science (EoR, Dark Ages) data for one-to-one mapping. The data is also converted to Jy for observations with SIM. For 1 MHz channel, two slices of the cuboids are used from the frequency corresponding to the observational frequency. As discussed in the previous section, the 6.2 is the complete sky signal including the extragalactic, galactic, and the 21-cm signal. The diffuse emission lingers below the extragalactic foreground which is an order of magnitude brighter at 10^{-6} Jy. The foreground removal is a non-trivial task and a wide range of efforts have been made in the area. While discrete point sources are calibrated out, the diffuse emission removal require multichannel approach, see [Chapman et al., 2012, 2013, 2014].

Antenna Configuration / Coordinates Conversion / Measurement Sets

The three components of the SIM middleware - Antenna Configuration, Coordinates Conversion, Measurement Sets - work in tandem. The coordinates of the antenna layout are usually in ENU (East, North, Up) system. When mapped on the Earth coordinates, the ENU coordinates have no physical meaning and therefore are converted to the World Geodetic System (WGS84) standard. The WGS84 is an implementation of the International Terrestrial Reference Framework (ITRF). The fundamental idea of the coordinate conversion is to place the original ENU layout of an array configuration at a desired location on the Earth. The location on Earth allows for transformation to the sky position coordinate system, for example the Right Ascension and Declination. Therefore, depending on the position of the source and time for observation the UV coverage on the sky is defined.

The Measurement Set (MS) is a data container for observations. It is defined based upon the observational parameters. For example, the Table 6.1 shows the observational details for single 1 MHZ channel observation for total of 10 hours for the field shown in the Figure 6.2. An empty MS then is used for collecting observational or simulation data. Each row of the MS contains single visibility and related data.

Observation Frequency	149.3 MHz
Channel Bandwidth	1.0 MHz
Date and Time	June 1, 2013, 11:11:11
Integration Time	30 sec

Table 6.1: The observational setup for SKA LOW-1.

In SIM, before any observations are simulated, the signal in the Figure 6.2 must be projected to the sky centered around the phase center of the MS. Once this is achieved we have a sky image and are ready simulate observations. The Figure 6.3 shows the sky signal projected on the sky. This is achieved by adding the appropriate FITS header to the data payload.

Telescopes

The telescopes simulated in this study are based upon the real-world array configuration data currently used in the case of LOFAR and officially proposed baseline designs for

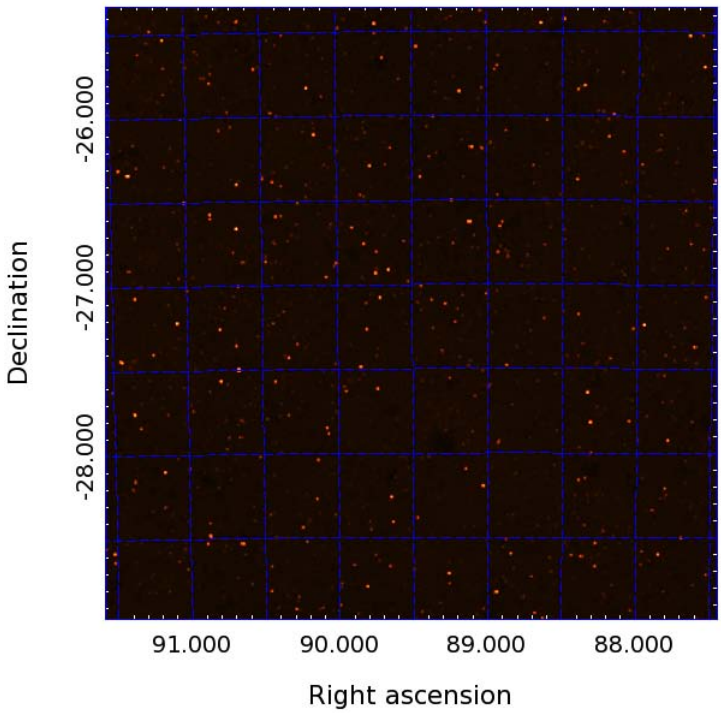

Figure 6.3: The 1 MHz bandwidth signal including the EoR, extragalactic, and Galactic foregrounds at $z = 8.515$ projected on the sky at RA = 90.5° and DEC = -27.71°. The side of image is$\Delta\ \theta = 3.74°$ and 425 h^{-1} Mpc . The image is 504× 504 pixels.

the SKA telescope. The underlying science goals ultimately drive the system design of any telescope array. However, large telescopes are never built for singular science goal. Therefore, optimally satisfying various scientific goals with a single system design requires tradeoffs. In the following sections, the existing and proposed designs are explored for the uv coverage and baseline distribution that ultimately define the performance metrics for the science goals..

LOFAR The LOFAR MS was directly obtained from the LOFAR EoR team. The specific MS used is entitled `L80897_SAP000_SB000_uv.MS.dppp.1ch10snew.dppp`. Antenna details from this MS were extracted and used to examine the baseline distribution and the synthesized beam. The MS for 10 hours and different observational frequency were also created using the Antenna coordinates from the original MS. The antenna diameter (stations) in the MS is 25 m and there are total of 61 stations. The baseline distribution and PSF, bit naturally and uniformly weighted are shown in the Figure 6.4. Note that an order of magnitude baselines roughly less tham a km is indicative of a dense core. For the EoR observation the general strategy is to observe with the dense core to gain sensitivity and use the longer baselines to build sky models for calibration.

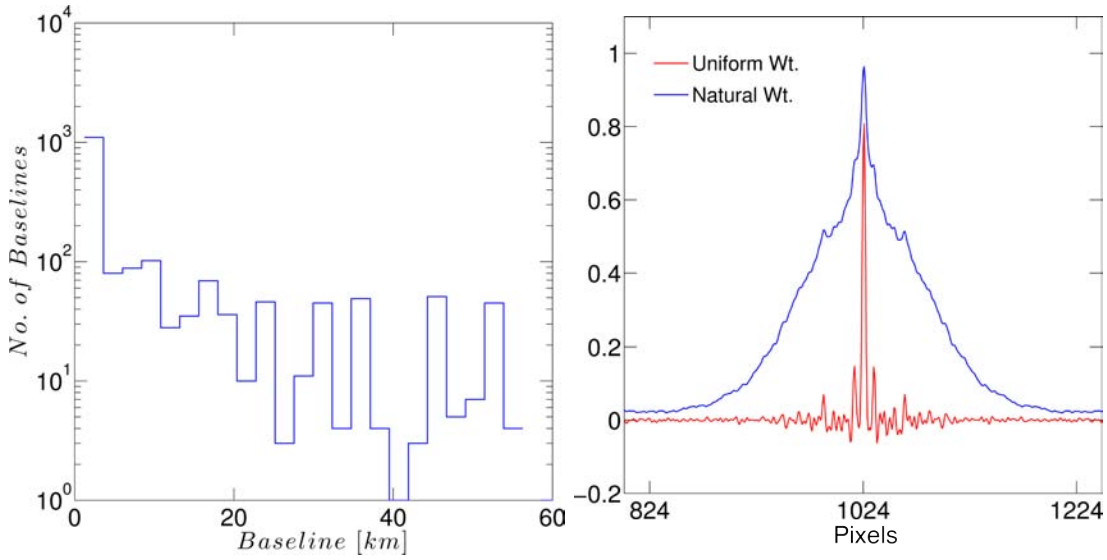

Figure 6.4: (Left) The baseline distribution for LOFAR. (Right) The synthesized beam of the entire array, with uniform weighting (red), and natural weighting (blue). The pixel size in the figure is 1.75″.

The uv-coverage for 10 hours for the LOFAR configuration at 136 MHz observing frequency is shown in 6.5 (Left). It is noticeable that certain regions of the uv-plane have higher density. Over density allows to sample the uv-plane completely, however, it also allows for building redundancy in case of faulty/corrupted stations.

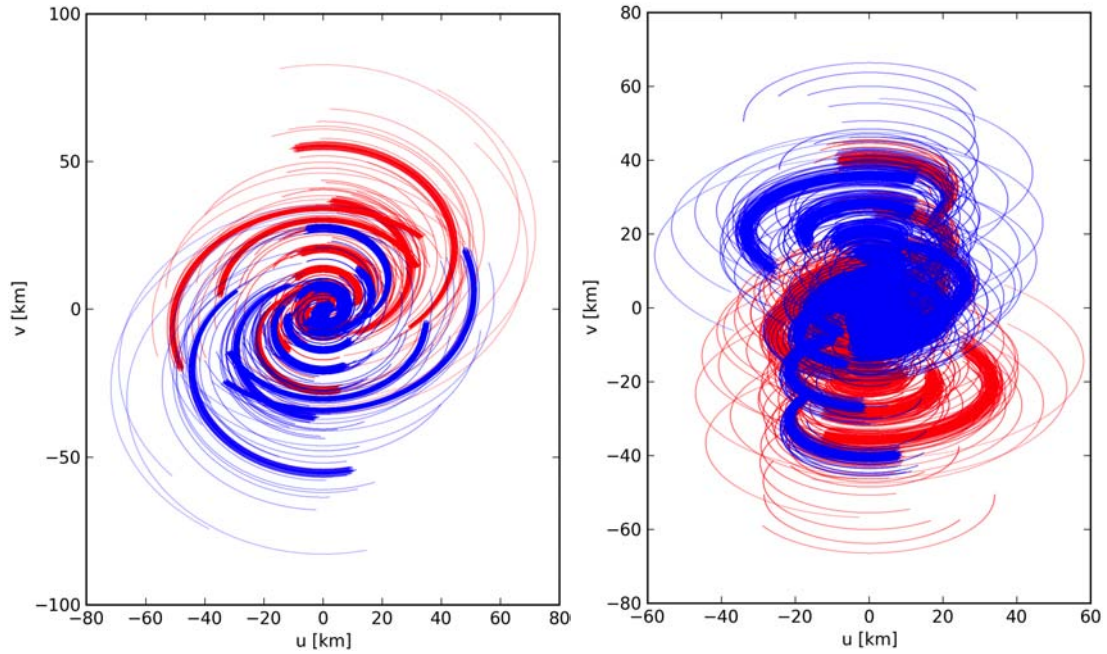

Figure 6.5: (Left) The LOFAR uv-coverage for 136 MHz observing frequency for 10 hours. (Right) The SKA-LOW for the 150 MHz for 10 hours. The red tracks are the UV tracks and blue represent the symmetric complex conjugate.

SKA LOW-1 and Variations We use the proposed SKA Low-1 baseline design (BD) as the fiducial configuration and make modifications as discussed below. The effective diameter of a station used in the BD is 45 m giving at field of view of 3.8 deg^2 at 160 MHz observational frequency. The diameter of the core is 5.29 km, and that of the arm is 66.51 km. The fiducial configuration, however, use 35 m diameter antenna stations with 866 in the core and 44 in the arm. While studying the baseline distribution of BD SKA Low-1 we discovered that many antennas in the core overlapped. In the discussions below we have imposed constraints to correct for this flaw in the original BD configuration.

Array Configuration The BD SKA Low-1 array configuration is a hybrid of open and closed configurations with a uniformly filled core critical for sensitivity for the observation of diffused radiation and long arms to synthesize narrow beams for compact source critical for calibrating extragalactic foregrounds.

This study uses 30 s visibility integrations to build the measurement sets, therefore, for large number of antennas the processing is computationally prohibitive. For example, in case of 500 antennas with 10 hours of observations with 30 s integration time, the visibility data (single visibility of 8 bytes complex number) 1.19 GB. This is for one channel and hugely underestimated because MS contains far more data than the 8 byte visibilites. We address the computational load by reducing the number of antennas in the core. The reduction of antennas results in incomplete UV coverage leading to side-lobes. However, by employing tapering the extended sources are easily detectable. Using the BD SKA Low-1 configuration, we define a new array by incorporating only 10% of randomly selected antennas from the core (87) and use all the antennas in the arm (44). The random selection applies the constraint such that no overlapping antennas are selected. The new configuration SKA Low-1-10 in the ITRF coordinates is shown in Figure 6.6. We also define arrays that are 2 times and 0.5 times the size of the BD SKA Low-1. The abbreviated names of the configurations, see Table 6.2, are used in the paper.

UV coverage and Synthesized Beam We define a measurement set (MS) of 10 hours with 30 s integrations for 1 MHz bandwidth centered at 149.3 MHz pointing at the phase center with RA = 174:00:00 and Dec = -26.70:00:00, and single polarization. The UV coverage for the MS is shown in Figure 6.5 (Right). For all of the imaging studies in the

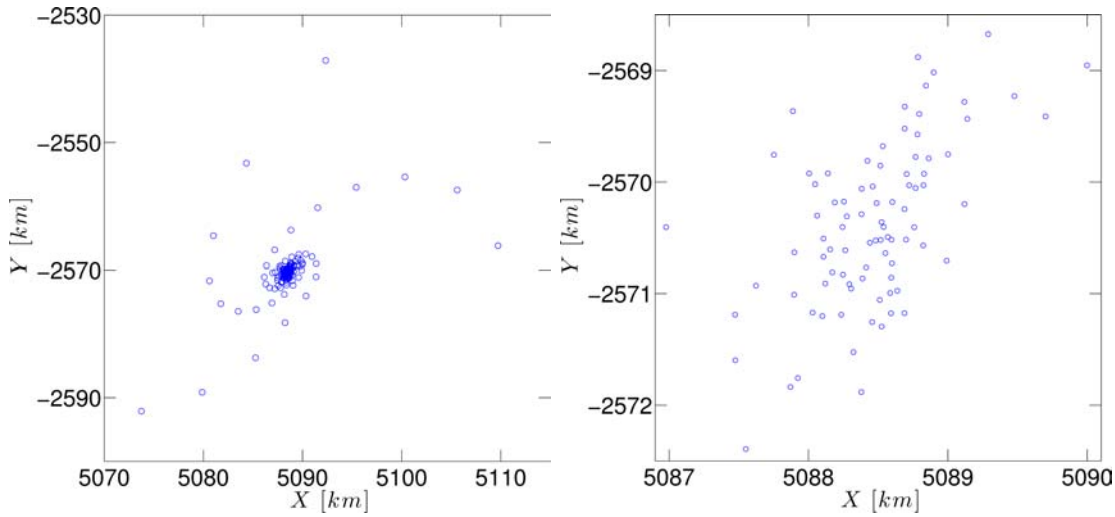

Figure 6.6: Left: SKA Low-1-10 is the 10% of the SKA LOW1. Right: Core of randomly selected antennas. The axes are in ITRF coordinates centered at the location with latitude $= -26.7^\circ$ and longitude $= 116.7^\circ$. The antenna diameter (not shown to scale) is 35 m. There are total of 131 antennas with 87 in the core and 44 in the arms.

Antenna Configuration	No. of Antennas Core + Arm = Total	Max. baseline Core (km)
BD SKA Low-1	866 + 44 = 910	5.29
SL10	87 + 44 = 131	4.22
SL10-2x	3464 + 176 = 3644	8.44
SL10-0.5x	217 + 11 = 228	2.11

Table 6.2: The parameters of the derived configurations used in the studies.

paper we use the single channel of 1 MHz. It is only for the 21-cm tomography more channels are added. The science and foreground data are integrated on the redshift bins corresponding to the 1MHz bandwidth at the 150 MHz observational frequency.

The baseline distribution of the entire SL10 configuration is shown in Figure 6.7. The total number of baselines for the configuration SL10 are 8515, 62% of which are less than 1.5 km. The planarity of the array (and therefore the baselines) is assumed for both the core and the arm resulting in minimal errors in the synthesized beam. The UV coverage of the SL10 configuration with the phase center at RA = 174:00:00 and Dec = -26.70:00:00, at 150 MHz is shown in Figure 6.5 (right). It is evident from the figure that the smaller baselines form a dense and overlapping (large redundancy) sampling pattern with relative thinning of the longer baselines.

The Figure 6.8 (left) shows the cross-section of the synthesized beam formed by natural

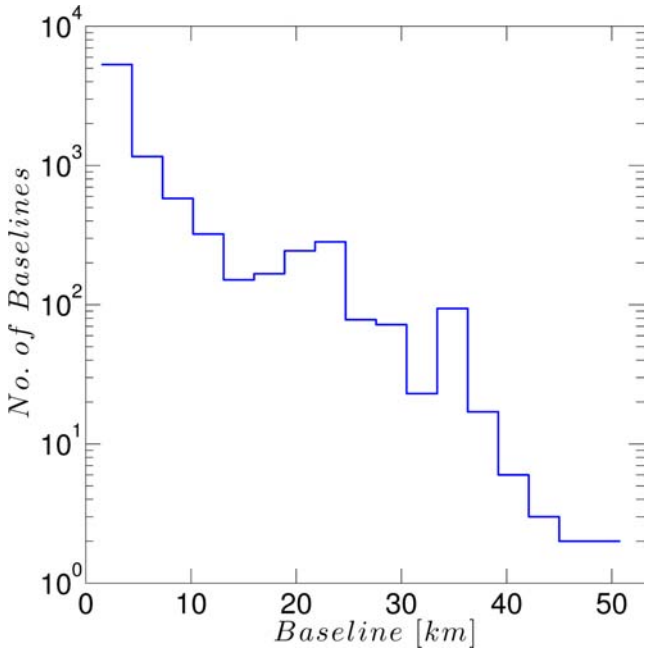

Figure 6.7: The distribution of baselines for the SL10 configuration. The ordinate axis is in log scale.

and uniform weighting for the core of SL10 configuration, and natural weighting for cores of SL10-2x and SL10-0.5x. The synthesized beam images are sized 2048×2048 ($30' \times 30'$). The first sidelobes, Figure 6.8 (right), in the uniform weighting for the SL10 core are of the order of 5-10% of the peak. This is primarily due to the incomplete sampling of the UV-plane. The sidelobes are accentuated due 90% missing antenna in the SL10 configuration. The synthesized beam quality study done by Braun [2014] shows that tapering the synthesized beam results in best response (low noise) at the first width half maximum (FWHM) of $300''(5')$.

The FWHM of the synthesized beams are tabulated in the Table 6.3.

Antenna Configuration	FWHM ($'$)
SL10 Core (natural wt.)	2.37
SL10 Core (uniform wt.)	0.96
SL10-2x Core (natural wt.)	1.18
SL10-0.5x Core (natural wt.)	4.74

Table 6.3: The first width half maximum of the synthesized beams at 150 MHz.

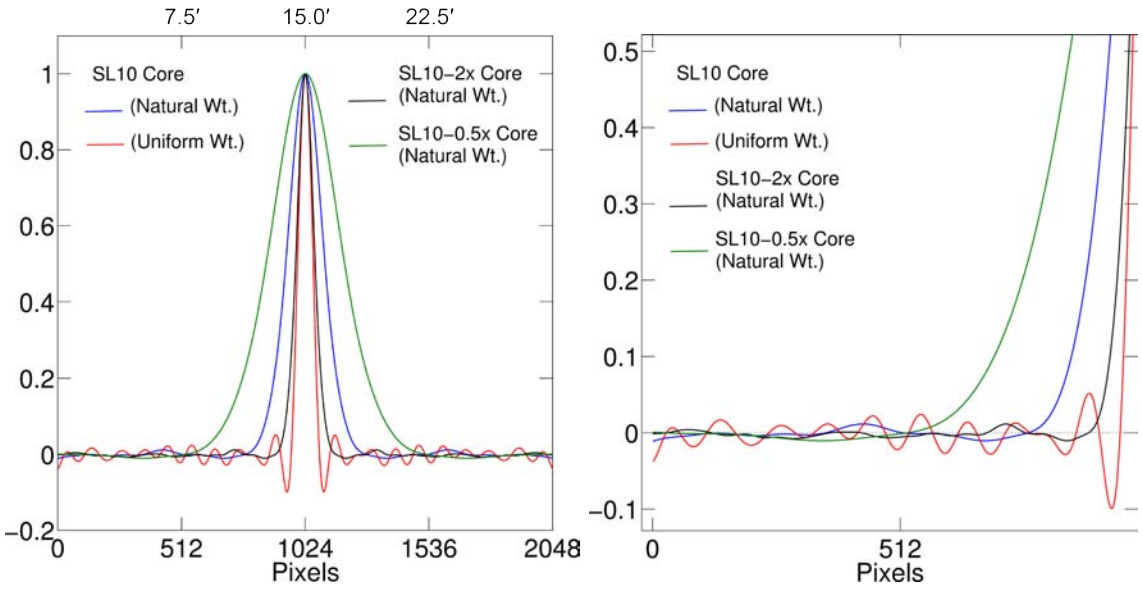

Figure 6.8: Left: The beam cross-section for the cores of SL10, SL10-2x and SL10-0.5x showing natural and uniform weighting. Right: The closeup of the sidelobes.

Analyses and Visualization

The final layer of the SIM middleware is Analyses and Visualization. The analyses is performed at two stages of data flow. One, directly at the comoving volumes, such as, power spectrum, morphological analyses, cross-correlations etc. Two, after the data is processed observational simulation. At this stage the power spectrum is still valid and provides a strong comparative before and after study. This technique is far more robust and insightful and next step to the commonly used Fisher analyses for single k or image plane PSF convolution studies. For the single channel images, radio astronomy metric such as the Image Fidelity and Dynamic Range were explored. However, these techniques were not able to capture the performance at different scales. In this thesis a new technique is developed entitled Spherically Averaged Spatial Spectrum (SASS) to examine the performance of the noise and convolution due to synthesized beam for the single channel data. This technique is described in detail in the next section.

Spherically Average Spatial Spectrum (SASS) The image quality in synthesis imaging is measured in terms of the dynamic range or the image fidelity [Cornwell et al., 1993]. The dynamic range is the peak brightness to the RMS noise of the image. Image fidelity on the other hand is the ratio of observed image to the difference of the observed and true sky model. Both these techniques have their merits and demerits. While the dynamic range is localized, the image fidelity assumes the knowledge of the true model

and returns a single number left for interpretation.

One of the primary science goals for the SKA class telescopes would be to image the H II regions. Hence it is imperative that the response of the configuration is known as a function of the observed spatial sizes. This is best captured by the radially averaged spatial spectrum of the image. This is same as the power spectrum, however, to avoid confusion with the power spectrum as used in the EoR studies, we term this metric as the spherically averaged spatial spectrum. This metric captures the entire image and is

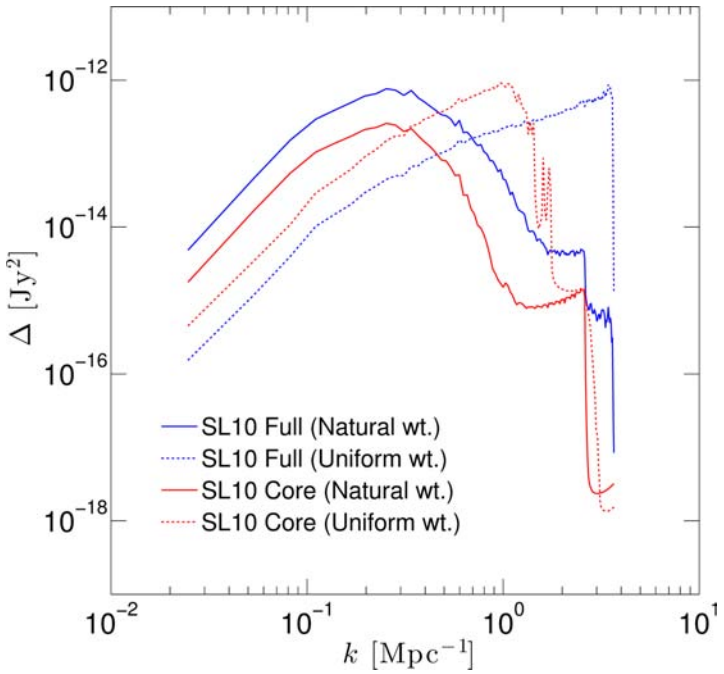

Figure 6.9: The spherically averaged spatial spectrum of the pristine sky model with SL10 full (blue) and core (red) configuration.

useful in examining variations across the large field-of-views. In addition, the technique is sensitive to the power at various scales. For a 3D data cube or a 2D averaged channel data, 3D or 2D Fourier transform is estimated respectively. Thereafter, the power in the concentric k values is averaged to genrate a 1D spectrum. The Figure 6.9 is the 1D spatial spectrum comparing the pristine signal with the SL10 configuration using the full and the core configuration. The spatial spectrum is plotted as the unit-less quantity $\Delta^2(k) = \mathrm{P}(k)\ k^3/2\pi^2$, where $\mathrm{P}(k)$ is the spatial spectrum of the image measured in image units, Jy/Beam or Jy. Note that this method radially averages the power when used on single channel images. The quantity$\Delta^{\ 2}(k)$ is related to the variance of the signal as $\approx \mathrm{d}\sigma^2/\mathrm{d}\ \ln k$. The spatial spectrum represents the variance in the d $\ln k$ bins. From the

Figure 6.9 it is evident that the core is sensitive to scales smaller than $k < 2.5$ Mpc^{-1} while the full configuration with longer baseline with higher resolution is sensitive to $k < 3.5$ Mpc^{-1}. It is also evident that the core is more sensitive to larger scale structures by an order of magnitude. The sensitivity of the core drops below the full configuration at scale $k \sim 0.65$ Mpc^{-1}. These results are based upon synthesized beam without tapering.

6.3 MeqTrees

The code MeqTrees forms the observational layer of the SIM framework. The details of MeqTrees are explained in the seminal paper by Noordam and Smirnov [2010]. The code implements the RIME [Smirnov, 2011a,b,c,d] and serves the purpose for simulations and third generation calibrations of the real world data. In their paper, Noordam and Smirnov [2010] demonstrate calibration of WSRT field around the bright source 3C147 and achieve the dynamic range of 1.6×10^6.

MeqTrees uses directed acyclic graphs (DAGs) to build computational sequences for visibility predictions per frequency per integration. A single monochromatic visibility representing 10 s of integration is M (2×2 matrix) M^H computations, where M is Jones' chain. For N(N-1)/2 baselines, bandwidth, and exposure time these computations steeply scale. The DAGs lend to the efficiency of the computation.

A DAG (tree) is a hierarchical relational construct (parent, child, friend, etc.) of nodes that represent the state of the data. The nodes are functionals and operate upon the data. This affords the code to be highly modular and flexible. In other words, additional functionality in the form of nodes is introduced later without disrupting the code. The implementation of the RIME equation of the form,

$$\mathbf{V}_{pq} = \mathbf{G}_p \left(\sum_{k=1}^{N} \mathbf{J}_p \mathbf{B} \mathbf{J}_q^H \right) \mathbf{G}_q^H, \tag{6.4}$$

is implemented in MeqTrees as a relational tree of nodes such as MeqAdd, MeqConjTranspose, MeqMatrixMultiply and so on. The Figure 6.10 shows this relational subtree schematic of the implementation of the RIME equation 6.4. There are various such subtrees for different time, frequency, antennas, and so on. In its totality the complete

state representation is called a forest. Note in the figure, the 2×2 matrices for gains($\mathbf{G}$), Jones' ($\mathbf{J}$), and coherency matrix ($\mathbf{B}$) are operated upon by functional nodes, such as, MeqConjTranspose, MeqAdd etc. In terms of propagation effects, the $\mathbf{G}$ and $\mathbf{J}$ represent the direction independent and direction dependent effects respectively.

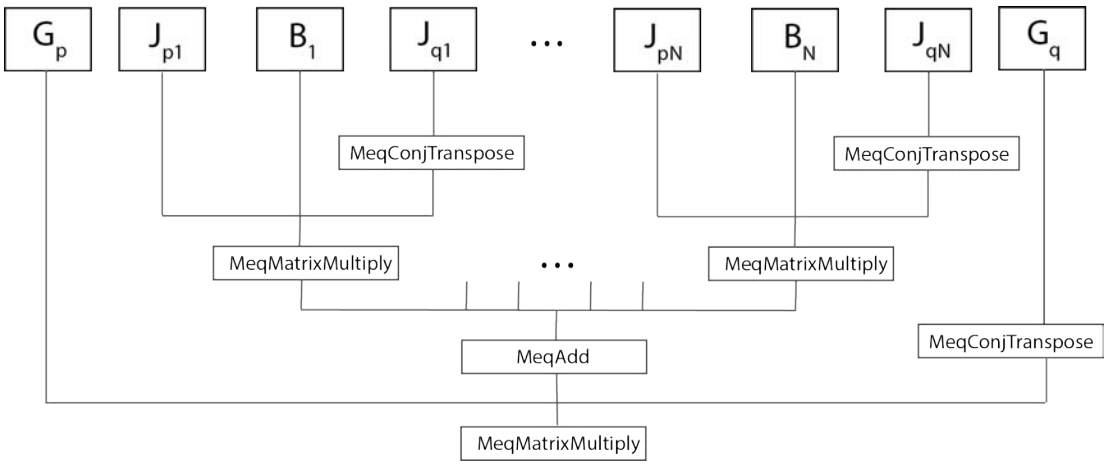

Figure 6.10: The subtree of a RIME implementation.

In MeqTrees the visibilities of the local sky model (LSM) are predicted in different ways. For the discreet point sources, the intensity, $I(l, m)$, is converted to coherency matrix, $\mathbf{B}(u, v)$, using discrete Fourier transform to predict the visibilities. For the sky images with diffuse or extended sources, an FFT with degridding generates $\mathbf{B}(u, v)$. In MeqTrees this is implemented as a node called UVBricks [Abdalla, 2009, Nijober, 2005] by using nodes MeqFFTBrick and MeqUVInterpol.

Meqtrees is a client-server architecture. The client builds the tree which is solved by the server. The interactive client for the MeqTrees is called MeqBrowser. Since MeqTrees is based on Python, the client side could be written as scripts and run non-interactively. There is inbuilt parallelism in MeqTrees. However, the application is not HPC ready yet. There are many ongoing efforts to make it more advanced.

Part III

Applications and Results

Summary

So far we have explored the scientific background, motivation, and developed the techniques/tools needed to conduct this research. We have developed new sets of simulation data that include different models of observed Lyman-limit systems and techniques of radiative transfer to study their effects on the reionization. We have consolidated state-of-the art tools into a framework named SIM to explore the wide range of propagation effects on the original 21-cm signal. We have also explored employing high-order statistics such as bispectrum to examine the underlying primordial non-Gaussianity as captured by the ionization epoch.

In this part of the thesis we will go over the analyses of each of the three applications, namely, LLS, propagation effects, and primordial non-Gaussianity, in detail, and discuss the results.

The motivation of this effort is to highlight the scope and significance of the techniques/tools in exploring the wide phase space of theory and observational planning.

Chapter 7

Lyman-Limit Systems Analyses

7.1 Results

We summarize the results of the analyses of the LLS simulations in the following section.

7.1.1 Globally Averaged Quantities

The Figure 7.1 shows the evolution of the globally averaged mass-weighted $\langle x_m \rangle$ and volume-weighted $\langle x_v \rangle$ ionized fractions of the three models as the function of redshift. In both the top and the bottom panels of the figure we note that the divergence of the models start at $z = 14$ and becomes pronounced at $z \sim 10 - 11$. While the ionization starts closer to denser regions, the shorter mean free paths for the LLSs delay the overall process of the expansion and merging of the H II regions. The volume without LLS reaches the ionization global average $\langle x_v \rangle = 0.98$ at $z = 8.34$, while for LLS1 and LLS2 the same ionization levels are reached at $z = 7.61$, and $z = 7.71$, respectively.

The top panel of the Figure 7.1 shows the ratio x_m/x_v, while the bottom panel shows only the averaged x_m. The ionized factions are global averages and the angled-brackets have been simply dropped for brevity. From the top panel it is quite evident that the mass-weighted ionized fraction is significantly higher than the volume-weighted fraction. The higher value of x_m is consistently maintained throughout the course of the simulation for all the three models. This means that the reionization is inside-out, that is, the dense regions surrounding the sources are preferentially ionized first yielding higher x_m averages. The ionization fronts expand outwards eventually reaching the less dense regions and voids. The ratio x_m/x_v is the mean over-density of the ionized regions [Iliev et al., 2006] as shown

below,

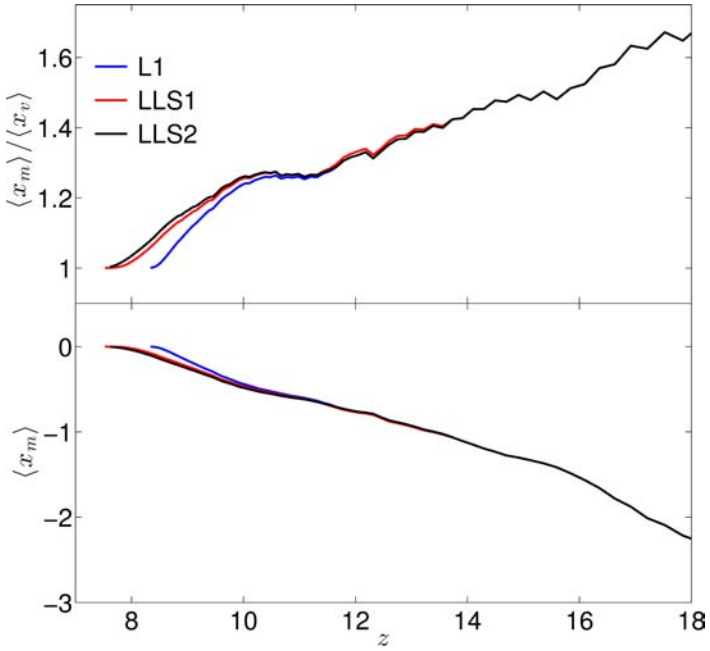

Figure 7.1: (Top) The ratios of mass- and volume-weighted, x_v, vs. redshift z; and (Bottom) Evolution of the ionized fractions: log of mass-weighted, x_m, for the three simulations L1, LLS1, and LLS2.

$$\frac{x_m}{x_v} = \frac{V_{\rm box}}{M_{\rm box}} \frac{x_m M_{\rm box}}{x_v V_{\rm box}} = \frac{1}{\bar{\rho}} \frac{M_{\rm ionized}}{V_{\rm ionized}} \tag{7.1}$$

where, $\bar{\rho}$ is the mean density of the Universe. The Figure 7.1 indicates that the ratio remains mass dominated (> 1) for all the models, while LLS cases reach the ratio of 1 much later. This is because less dense regions such as voids do not have ionizing sources and therefore require photons from afar to get ionized. The simulations LLS1 and LLS2 reach the numerical ratio value of 1.003 at redshifts $z = 7.76$ and $z = 7.617$ respectively, while for the L1 model the value is reached much earlier at redshift $z = 8.397$, thereby, delaying the ionization by$\Delta\ z = 0.78 - 0.64$.

The ratio of the two ionized fractions, x_m/x_v, is in fact equal to the average gas density in the ionized regions in the units of the mean density of the Universe. This is a manifestation of the predominantly inside-out character of reionization. The high-density regions and local density peaks surrounding the sources are ionized first. The ionization fronts then expand further into both high- and low-density nearby regions, with the material in the large voids getting ionized last. The highest-density cells are almost instantly ionized and

remain ionized throughout the simulation, while the lower-density cells take progressively longer to become ionized. Higher-density cells are on average always more ionized than lower-density ones. Naturally, closer to overlap the average density of the ionized regions approaches the global mean density, and both high- and low-density cells become mostly ionized.

7.1.2 Photon Statistics

The reionization period is defined by the complex interaction and evolution of the ionizing photon sources and sinks. In the simulations the sources of the ionizing photons are the halos. The very first of the insuppressible halo forms around $z \sim 21$. For a more in-depth study of the mass and the number density distribution of the halos see Iliev et al. [2012]. The clustering of halos defines the photon emanating regions and sets the initial conditions for the formation and evolution of H II regions. The mean free path is dominated by the size of the ionized regions in the IGM. While the LLSs continue to absorb the ionizing photons, it is only towards later times ($z \sim 14 - 10$) that the absorption contributions due to the LLSs become dominant.

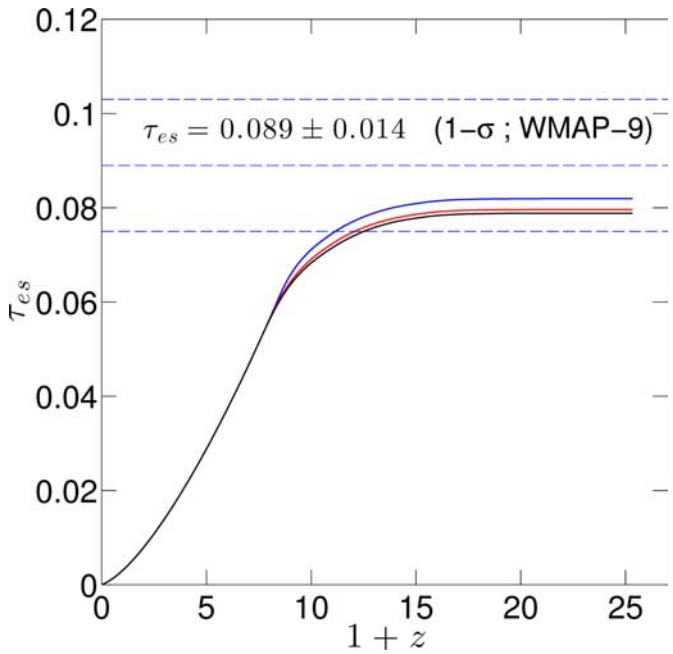

Figure 7.2: The Thomson electron scattering optical depth, $\tau_{\rm es}(z)$ integrated for simulation redshifts for the cases, L1, LLS1, and LLS2. Horizontal lines indicate the mean and 1-σ limits derived from the WMAP-9 year.

The photon and baryon populations in the simulations are recorded to extract statistical properties of interest. The Figure 7.2 shows the integrated Thomson electron-scattering

optical depth, $\tau_{\rm es}$, for the three ionization cases as the function of redshift. Also plotted are the WMAP-9 mean optical depth estimates with 1-σ spread. All the three optical depths fall within the 1-σ range of the observed values. The values of the optical depth, $\tau_{\rm es}$, in the simulations at $z = 25.33$ for L1, LLS1, and LLS2 are 0.0819, 0.0796, and 0.0788, respectively. The optical depth in the presence of LLS is diminished by about ~ 0.002. This is expected as there are overall less ionized electrons available for scattering the CMB photons. The three ionization histories are the result of available ionizing photons from

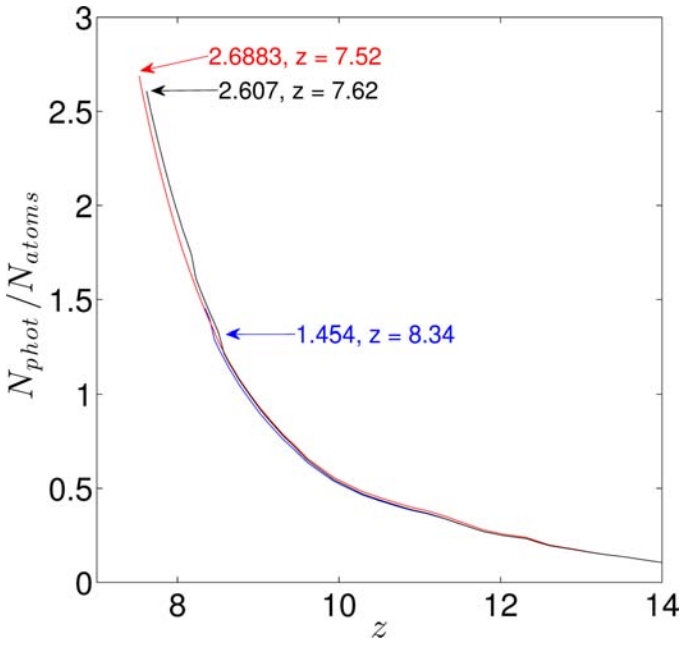

Figure 7.3: The cumulative number of ionizing photons per total gas atoms in the simulation volume for the three ionization case, L1 (blue), LLS1 (red), and LLS2 (black). The arrows label the respective N_{phot}/N_{atoms} values and the corresponding redshifts of the overlap.

the sources. The Figure 7.3 shows the cumulative number of photons per baryons as the function of redshift. At the end of the ionization for the three cases, the photons per atoms are twice as many for the LLS case. The LLSs, therefore, absorb an approximately 1 extra photons before reionization is completed with not much difference between the two LLS cases. Their effect dominates over the recombinations included in the simulation which only have consumed 0.5 photon per baryon by the end of reionization.

7.1.3 Morphology of the H II Regions

The morphology of ionized regions is complex. We use several methods to quantitatively study the H II region sizes, distribution, and evolution in the presence of the two LLS models. These methods, as discussed below, provide complementary information.

One of the expected outcome of different mean free paths, $\ell(z)$, of the ionizing photons of different LLS models, is that the varying evolution of the size distribution of the H II regions and the consequent ionization fraction history. Once the H II regions grow larger than the mfp in certain directions, not all sources inside the region can contribute to their growth and therefore they will not grow as fast as in the case without LLS. The H II regions can still grow larger than the mfp because they are driven by many sources some of which lie closer than the mfp to the edge of the region.

Evolution of the H II Regions

The Figure 7.4 shows examples of the morphologies and growth of the ionized patches in the presence of the varying model-dependent mean free paths, $\ell(z)$. The top panels show the ionization history of the fiducial model L1 (case without LLS) spanning redshifts, $z = 16.9$-8.5, approximately 370 million years. The panels from left to right show the slow ionization process, which reaches mass weighted ionized fraction of 1% only at $z = 16.9$, even though the first halos in the simulation (with $M > 10^8$ $M_\odot$) form at $z = 21$.

The halos are strongly clustered about the high density peaks. This is common throughout the duration of the simulation, but even more so at the higher redshifts. The complexity of the non-symmetrical morphologies grow as the ionization progresses and the smaller H II regions merge. To gauge the resolution of the simulation and the evolving physical sizes of the H II regions, the volume of a given H II region is estimated using the time derivative of the Equation 5.4, [Friedrich et al., 2011]. The minimum volume, $V_{\rm min}$, of the emerging H II region is,

$$V_{\rm min} = \frac{dN_\gamma}{dt}\frac{\Delta t_i}{n_{\rm H}} \tag{7.2}$$

where, N_γ is the total number iof ionizing photons from a halo of mass M, Δt_i is the radiative transfer simulation time step and $n_{\rm H} = \Omega_b(\rho_{\rm crit}/\mu m_p)$ is the number density of hydrogen. The recombinations are ignored in this estimate and therefore it provides an overestimate. For the time-step value of$\Delta\ t_i = 5.75 \times 10^6$ yr, the smallest volume is $V_{\rm min} = 0.1361\,{\rm Mpc}^3$. In comparison the cell volume of the simulation box of size 114 h^{-1} Mpc is ~ 0.25 Mpc^3, which is 1.8 times larger than $V_{\rm min}$. This is the reason the H II regions remain unresolved in the early stages of the simulation and appear on the maps

as partially ionized cells. However, by 10% ionization at $z \sim 13$, the H II regions are large enough to be visible. The rapidly growing sizes and the mergers of the ionized regions are shown in the right panels on the top. The total volume of the simulation box is 4.32×10^6 Mpc^3 with the resolution of 256^3 cells, leading to the volumetric dynamic range of the simulation of the order $\sim 10^7$.

The bottom three panels of Figure 7.4 emphasize the morphological and topological difference between the three simulation models. The three spatial ionization slices compare the global ionization of $\langle x_m \rangle = 50\%$ for models, L1, LLS1, and LLS2. The most immediate features visible are the different sizes of the larger H II regions, especially between the non-LLS and the LLS models. This is indicative of the effect of LLS that slows down the merger process. In the case of models LLS1 and LLS2 the differences in shapes and sizes of the ionized regions are not severe, however, in detailed statistical analysis discussed below, some differences emerge. As expected, the slow growth of ionized regions delays the complete ionization for LLS simulations.

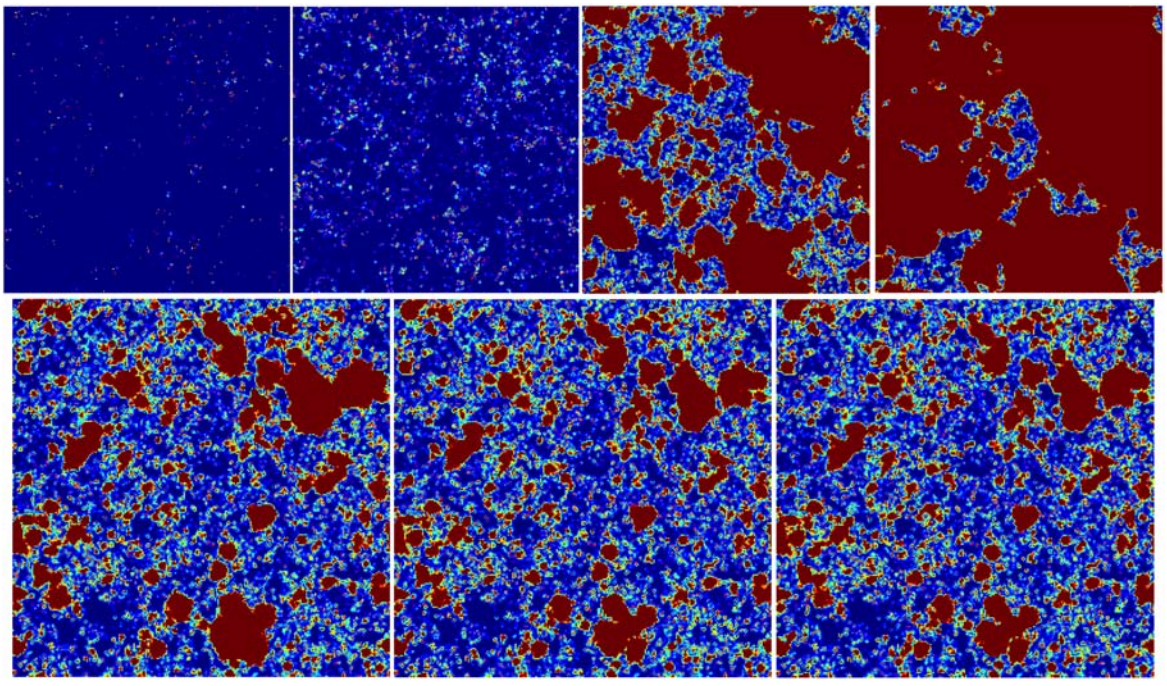

Figure 7.4: (Top) Spatial slices of the ionized hydrogen for the 114 h^{-1} Mpc box for the L1 case with no LLSs at different ionization fractions and redshifts. From left to right - $\langle x_m \rangle = 0.1$, 10.0, 75, and 95% at $z = 16.9$, 13.2, 8.892, and 8.515. (Bottom) Spatial slices for three models at $\langle x_m \rangle = 50\%$. From left to right, models L1, LLS1, and LLS2 at redshifts $z = 9.4$, 9.3, and 9.1.

7.1.4 Size Distribution of H II Regions

In this section we quantify the results seen in the Figure 7.4 by using three different methods to study the size evolution of the H II regions in the numerical simulations of the reionization with two different LLS models, LLS1 and LLS2, and compare them against L1, the case without LLS. The statistical property measured in this analysis is the probability function of the volumes (radii) of the H II regions. The three approaches employed to estimate these size distributions are the friends-of-friends (FoF) [Iliev et al., 2006], the spherical average (SPA) [Zahn et al., 2007] and 3D power spectra methods. All of these algorithms differ in their approach of defining the size of the H II regions as discussed below. However, the different techniques complement each other and together provide greater insight into the morphologies and the evolution of the H II regions.

Friends-of-Friends

The friends-of-friends (FoF) algorithm operates on the ionized fractions and generates a catalog of ionized H II regions. For the desired ionization threshold, x_{th}, the algorithm connects all the ionized neighboring cells and classifies them in a friendship based topology using the 'equivalence class' or 'sameness' method of the Numerical Recipes [Press et al., 1992]. The H II regions catalogs based upon the ionization threshold and volume size are thus generated. These catalogs provide detailed insight in the evolution of the number densities and size distributions of the topologically-connected ionized regions. This method was first introduced in Iliev et al. [2006].

The FoF H II region catalog is strongly dependent on the free parameter, the ionization threshold value x_{th}. In Figure 7.5 we illustrate the effect of this parameter in estimating the sizes of the H II regions. Shown is the probability distribution function at different friends-of-friends threshold values $x_{th} = 0.1, 0.5$, and 0.9, versus the volume size of the H II regions for the no LLS model at the global ionization of $\langle x_m \rangle = 0.5$ that occurs at $z = 9.457$.

For a quick visual inspection of the regions, the slice from the data cube corresponding to the same redshift, is shown in the bottom left panel of the Figure 7.4. At the global ionization fraction of the order 50%, the dichotomy of many small and one very large,

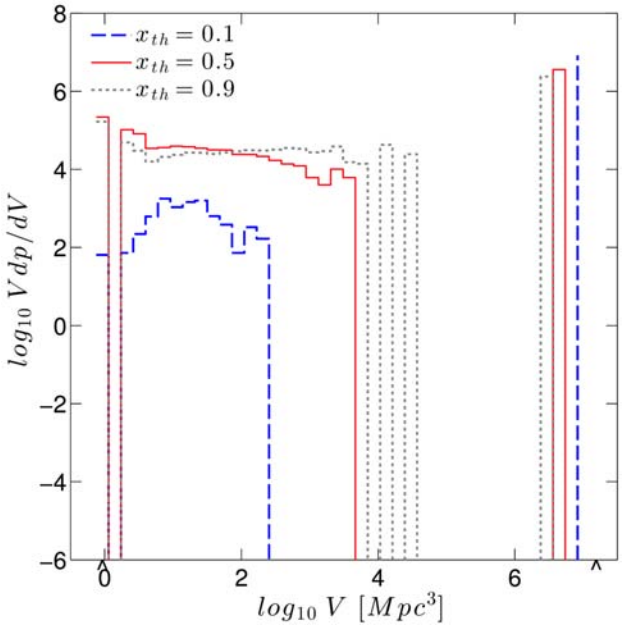

Figure 7.5: The effects of three different thresholds, $x_{th} = 0.1, 0.5$, and 0.9, in the FoF method for the ionization simulation for the L1 (no LLS) case at z = 9.4 with global ionization fraction of $\langle x_m \rangle = 0.5$. The two arrowheads on the abscissa, from left to right, mark the volume of a single cell (0.25 Mpc^3) and the volume of the box (4.3×10^6 Mpc^3) respectively.

connected region is evident for all the thresholds. As is evident in Figure 7.5, for the threshold of 0.1, the FoF algorithm over-links the H II regions, resulting in almost all being merged into the one large, connected region through partially-ionized 'bridges'. In contrast, for the threshold values of $x_{th} = 0.5$, and 0.9 the resulting distributions are relatively similar. The higher threshold value of 0.9 results in the large, connected region taking a significant fraction of the volume to break up into several smaller regions. For consistency the threshold value of $x_{th} = 0.5$ is used throughout the analyses.

The topological evolution of the H II regions for the L1 and LLS2 models is shown in Figure 7.6 for the threshold value $x_{th} = 0.5$. The difference between the two LLS models was not discernible in the FoF analysis, therefore only one model comparison is shown in the Figure 7.6. The color represents the probability distribution dp/dV. It is evident from Figure 7.6 that the H II regions grow as the ionization fraction increases up to a point where the volumes of the regions separate into two populations comprising of very large and relatively smaller sized regions. The emergence of the dichotomy is primarily due to the merging of smaller regions into a larger volumes as the ionization fronts travel outwards from the higher density areas. As expected, the larger H II regions of the order

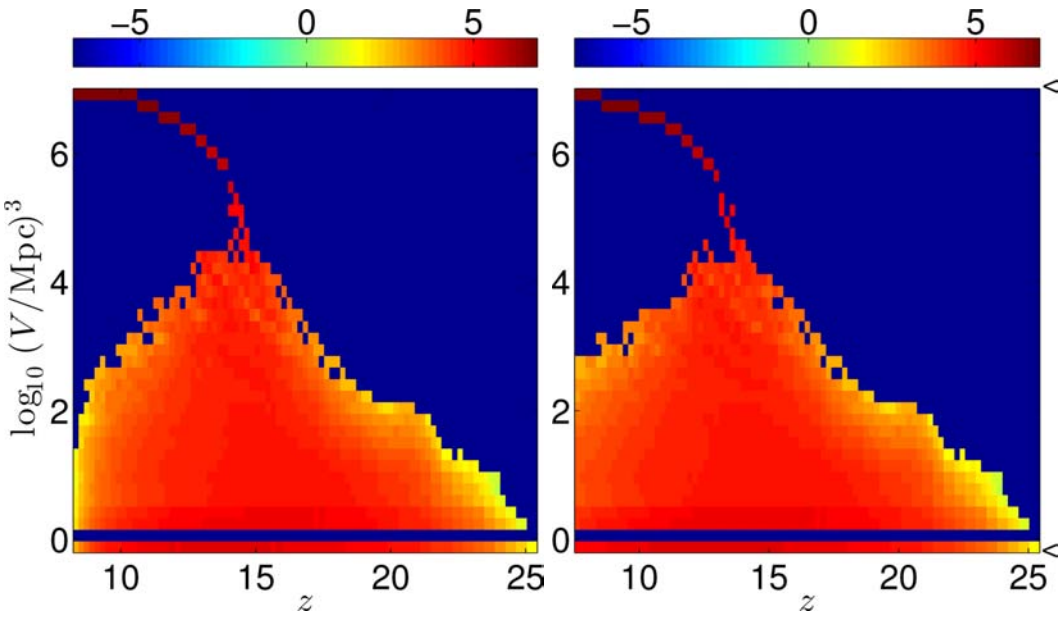

Figure 7.6: Size distributions of the ionized H II regions using the FoF method for the models L1 (left) and LLS2 (right) as a function of the redshift. The threshold used is $x_{th} = 0.5$. The colors correspond to the $\log_{10}$ scale of the Vdp/dV. The two arrowheads on the ordinate (right), from bottom to top, mark the volume of a single cell (0.25 Mpc^3) and the volume of the box (4.3×10^6 Mpc^3) respectively.

of $\sim 10^6$ Mpc^3 appear slightly earlier in the L1 ($z = 13.48$) case as compared to the LLS2 ($z = 12.31$) model. Another difference between the the two models is that the largest of the "small" H II regions disappear faster in the L1 case than in the LLS models. This is indicative of fewer mergers in the LLS cases as these regions only disappear when they merge with the larger regions. Towards the end of the ionization, the contribution to the global average of the ionization rate is largely due to largest regions. For the no LLS case L1, at $z = 8.34$ ($\langle x_m \rangle = 0.99$), the second largest H II regions are 50% smaller compared with the similar population in the LLS2 simulation. This emphasizes the trends we have noticed earlier where the ionizing photons of the shorter mean free paths are absorbed and fail to contribute in the formation of H II regions that grow and merge. In both the no LLS and LLS scenarios we notice that when the ionization reaches 10%, there are two distinct populations of H II regions that emerge and begin to diverge; more steeply for the no LLS mode. Largest volumes are of the order of volume of the entire box. The single-cell populations of H II regions also contribute throughout the ionization history but are limited to the cells. From the observational perspective, the large H II regions could be directly imaged with SKA-class interferometers. The volume distribution of such regions may help put limits on the mean free path and therefore on the LLS models.

Spherical Averaging

The second algorithm to evaluate the size distribution statistics was developed in Zahn et al. [2007]. The numerical scheme in the spherical averaging technique constructs spheres of varying radii around each cell in the ionization simulation and estimates the enclosed ionization fraction. The largest spheres with ionization fraction greater than the defined threshold x_{th} define the spherically averaged H II regions. In contrast to the FoF method, the SPA technique yields a smoother and spherical distribution function, biased towards the shorter axis of a triaxial structure.

The SPA analyses highlight similar behavior in the evolution of the ionized regions as seen earlier with FoF method. The shorter mean free path for the LLS simulation affects the growth as measured in the radii of the spherical regions. In Figure 7.7, the solid, dashed, and dotted lines correspond to the 50%, 70%, and 90% global ionization rates respectively. The color motif remains the same throughout the paper with L1 (blue), LLS1 (red), and LLS2 (black). The corresponding redshifts for which the distributions are estimated for the two models are LLS1: $z = 9.236, 8.636, 8.172$ and LLS2: $z = 9.164, 8.515, 8.812$. The vertical lines are the mean free path for the two LLS models as shown in the Figure 5.1. These lines are plotted for radii at 50 and 90% ionization.

It is evident in the Figure 7.7 that the smaller radii ($< 0.2 - 0.3$ Mpc) for all the three models are relatively of the same size at different stages of the ionization history. However, for the larger radii (> 0.3 Mpc) the differences in the probability distributions between L1 and both the LLS models emerge; especially as the ionization progresses. For example, at the 50% and 70% ionization stages, the radii in L1 simulations compared to the LLS models are larger by factor of $\sim 2 - 3$. This trend is also evident in longer mfp LLS1 model. At 90% ionization most of the H II regions have merged and therefore the spherical volumes appear the same. In addition, at radii values reaching $\sim 80 - 90$ Mpc the H II regions are as big as the simulation box ($R_{114} = 81.42$ Mpc). The spherical averaging algorithm reaches its limits at this stage.

The maximum radii difference between LI and LLS2 for 50, 70, and 90% ionization varies

from roughly 18, 33, to 18%. Another characteristic that is apparent from the SPA analyses is that for early times the smaller spheres for the LLS2 ionization model make the most contribution to the probability distribution, $R\ dp/dR$. However, this behavior is not so obvious at later times. This is attributed to slow growth of the H II regions in the LLS simulations and hence the larger population of smaller bubbles. In contrast, the bubbles of larger radii merge early for no LLS model. When the ionization reaches 50%, the maximum radii of the H II regions are comparable to the mfp, more for the LLS2 model than for LLS1. However, as the ionization progresses, the radii of the H II regions grow beyond the mfp due to mergers.

These results are consistent with ones from FoF method. The unimpeded ionizing photons in the L1 model noticeably differentiate the ionizing history from that of the LLS models. There is not much difference between the LLS ionizing histories themselves, with radii less than 10% different at different stages of the ionization rendering them hard to distinguish.

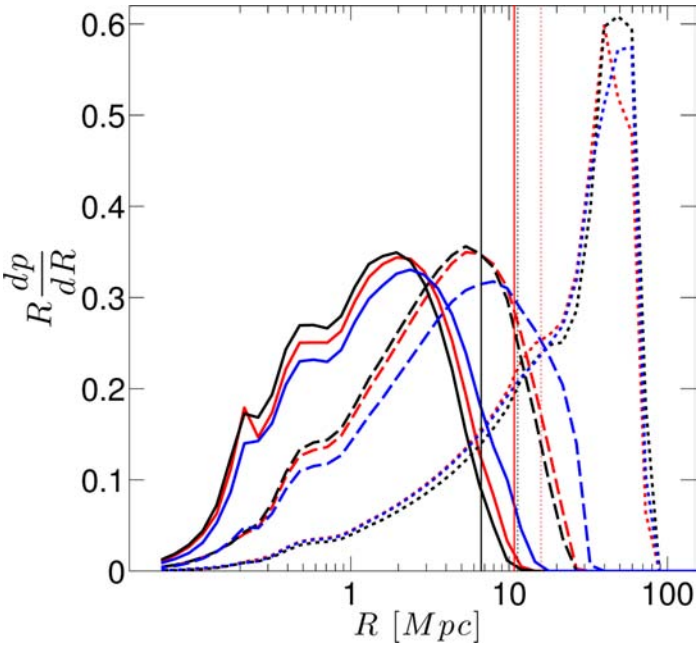

Figure 7.7: Probability distribution function $R\ dp/dR$ per radial bins of spherical H II regions as measured by the spherical averaging algorithm for the no LLS (L1, blue), and LLS models (LLS1, red) and (LLS2, black.) The three sets are for the mass-weighted global ionization fraction $\langle x_m \rangle = 50\%$ (solid), 70% (dashed), and 90% (dotted). The threshold used is $x_{th} = 0.9$. The vertical lines correspond to the mean free path for the two LLS models as listed in Figure 5.1 for the 50% and 90% ionization fraction.

Ionized fraction Power Spectrum

The third method for the volumetric analyses is the power spectrum of the ionized fraction field. The power spectrum is a measure of the contribution from different spatial frequencies and therefore is sensitive to the underlying structures. In the case of the ionization filed, the different sizes of the H II regions are captured in the spatial frequencies.

The Figure 7.8 shows the dimensionless power spectrum per comoving wavenumber, k [Mpc^{-1}h], of the ionized fraction field at ionization stages of 70% and 90% for all the three models, and is calculated as the dimensionless quantity,$\Delta^2_x(k) = k^3P(k)/2\pi$. The power spectrum is the radially averaged 3D Fourier transform of the ionization fraction volume. At the 70% ionization stage, see left panel of Figure 7.8, the steep slope at the large scales highlights the mergers of the H II regions. The size of the H II regions for all the three models peak at $k \sim 0.9$ and quickly merge to larger scale. As the reionization progresses and reaches to 90%, see right panel, the slope on the small scales also steepens indicating the decline of smaller regions as the ionization reaches towards completion. The peak in this case shifts towards smaller value of $k \sim 0.2$. It is evident in the figure that at large scale features ($k < 0.3$ Mpc^{-1}h) the power due to the H II regions is larger by a factor of 2-3 for the L1 (non LLS) case in both stages of ionization. However, as the ionization progresses, reaching 90%, the contribution from the small scale features ($k > 0.5$ Mpc^{-1}h) diminishes, indicating relatively larger H II region for L1 compared to LLS cases.

7.2 Observing Redshifted 21-cm

The first generation of radio telescopes will focus on statistical quantities, such as the power spectrum, of the neutral regions. The comprehensive studies of the 21-cm power spectra evolution help identify preferred wave-numbers that in turn help define the next generation array layouts. The discussion below explores the 21-cm signal with brightness temperature fluctuations and 21-cm power spectra. In addition, we discuss some of the observable signatures of cosmic reionization based on the redshifted 21-cm emission from neutral hydrogen expected to be detectable quantities for the current and upcoming 21-cm experiments.

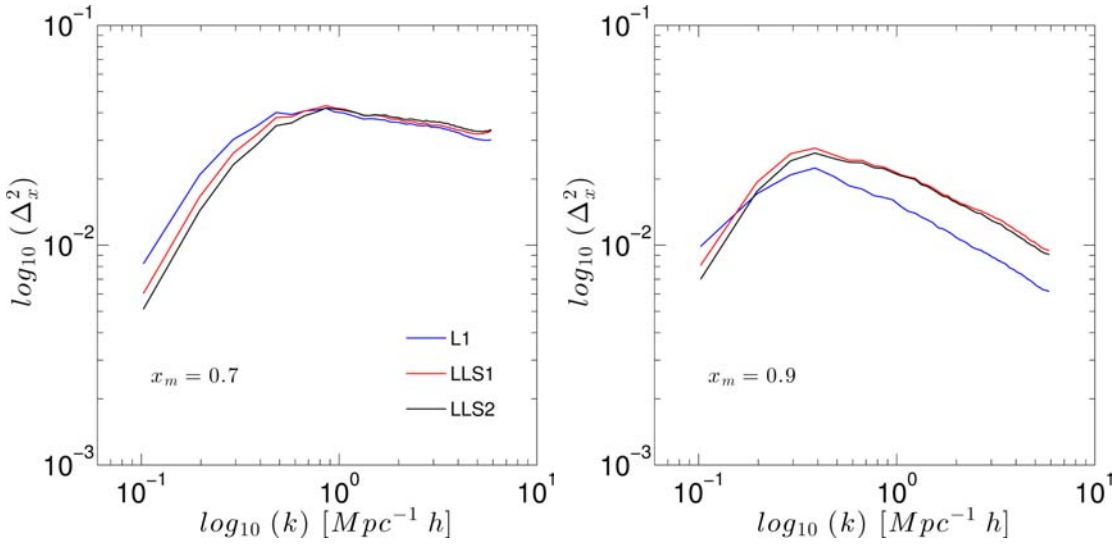

Figure 7.8: The log-log plot of the dimensionless 3D power spectra of the ionized fraction, at $\langle x_m \rangle = 70\%$(left) and $\langle x_m \rangle = 90\%$ (right) for the three models.

7.2.1 RMS of the 21-cm background

The differential brightness temperature of the redshifted 21-cm emission with respect to the CMB is given by the spin temperature, $T_{\rm S}$, of the neutral hydrogen and its density, $\rho_{H\,I}$, and at the limit such that $T_{\rm S} \gg T_{\rm CMB}$ is given by [Field, 1959],

$$\delta T_b = \frac{T_{\rm S} - T_{\rm CMB}}{1+z}(1 - e^{-\tau}) \tag{7.3}$$

where, z is the redshift, $T_{\rm CMB}$ is the temperature of the CMB radiation at z, and τ is the corresponding 21-cm optical depth.

As seen in the previous analyses, the overall effect of the LLS is to slow the ionization process and impede the growth of the H II regions. This should manifest as two observable properties. One, the peak of the brightness temperature fluctuations for the LLS simulations should be delayed and therefore should be visible at relatively higher frequencies; and two, the amplitudes of the peaks should be diminished due to the relatively smaller size of the H II regions in the LLS simulations.

The Figure 7.9 shows the evolution of the RMS fluctuations of the mean differential brightness temperature for the three simulation models as convolved with LOFAR-like boxcar beam of size $3'$ at bandwidth of 0.2 MHz. As depicted in the figure, at lower

frequencies (early times) the fluctuations for all the three models are similar and closely track each other. The temperature fluctuations peak at 141 MHz for the L1 model and 147 MHz for the LLS1 and LLS2 models. The peak value of the brightness temperature RMS for the L1 model is 6.06 mK with the brightness temperature of 16.66 mK. The RMS is lower about 9% and 8.7% for LLS1 and LLS2 models respectively. The temperature fluctuations RMS vs. the mass-weighted ionization global average are shown on the right side of the Figure 7.9. The brightness temperature fluctuations are again seen following each other very closely at early times. However, as the ionization reaches 20% the temperature fluctuations for different models start to diverge and peak at about 65-70% of the ionization stage. Whereafter, the temperature fluctuations subside and are indistinguishable as the ionization completes.

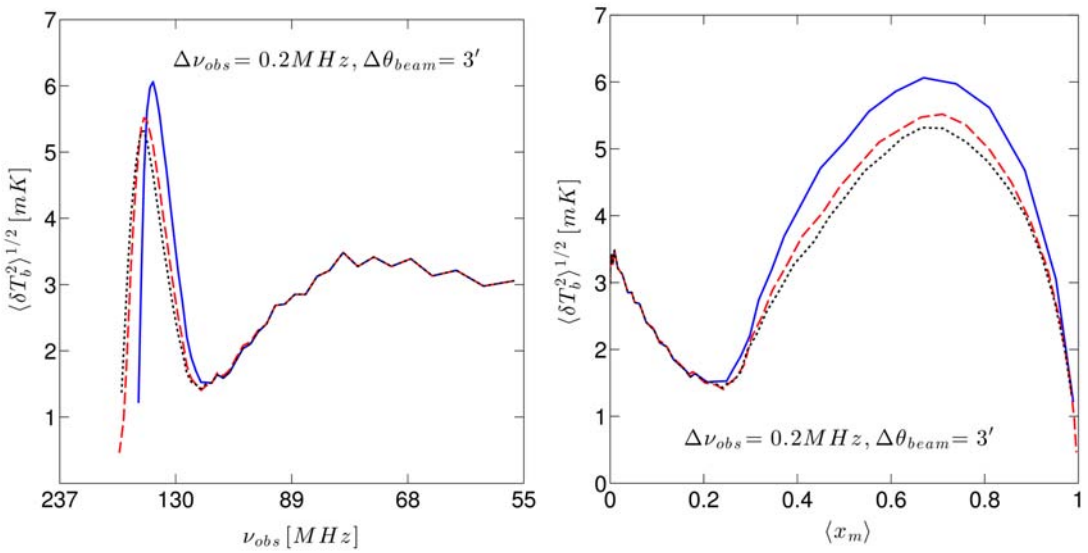

Figure 7.9: The evolution of the RMS fluctuations of the 21-cm background, for beamsize $3'$ and bandwidth 0.2 MHz and boxcar filter vs. frequency (left) and vs. average ionization (right). The simulations shown are L1 (blue, solid), LLS1 (red, dashed), and LLS2 (black, dotted).

As mentioned earlier, these differences in brightness temperatures are manifested by the varying distribution and growth of H II regions in the different models as seen in the statistical analyses of previous sections. These fluctuations have been averaged over by LOFAR-like beam and bandwidth. This is a simple first order estimation. Detailed and more accurate estimates require defining a noise budget including system temperatures, gains and phase errors, along with propagation effects (foregrounds, ionosphere etc.) and telescope based visibility sampling functions. Expectedly, increasing bandwidth reduces

the RMS as the fluctuations for a wider bandwidth are smoothed out. The increasing of the resolution of the beam increases and broadens the RMS. This is also expected as a smaller beam is sensitive to small scale fluctuations that are smoothed out by larger beams. Similar to the analyses in the previous sections, the differences are more pronounced between non-LLS and LLS models. However, based solely upon brightness temperature fluctuations it will be non-trivial to distinguish between the LLS models, see Figure 5.1.

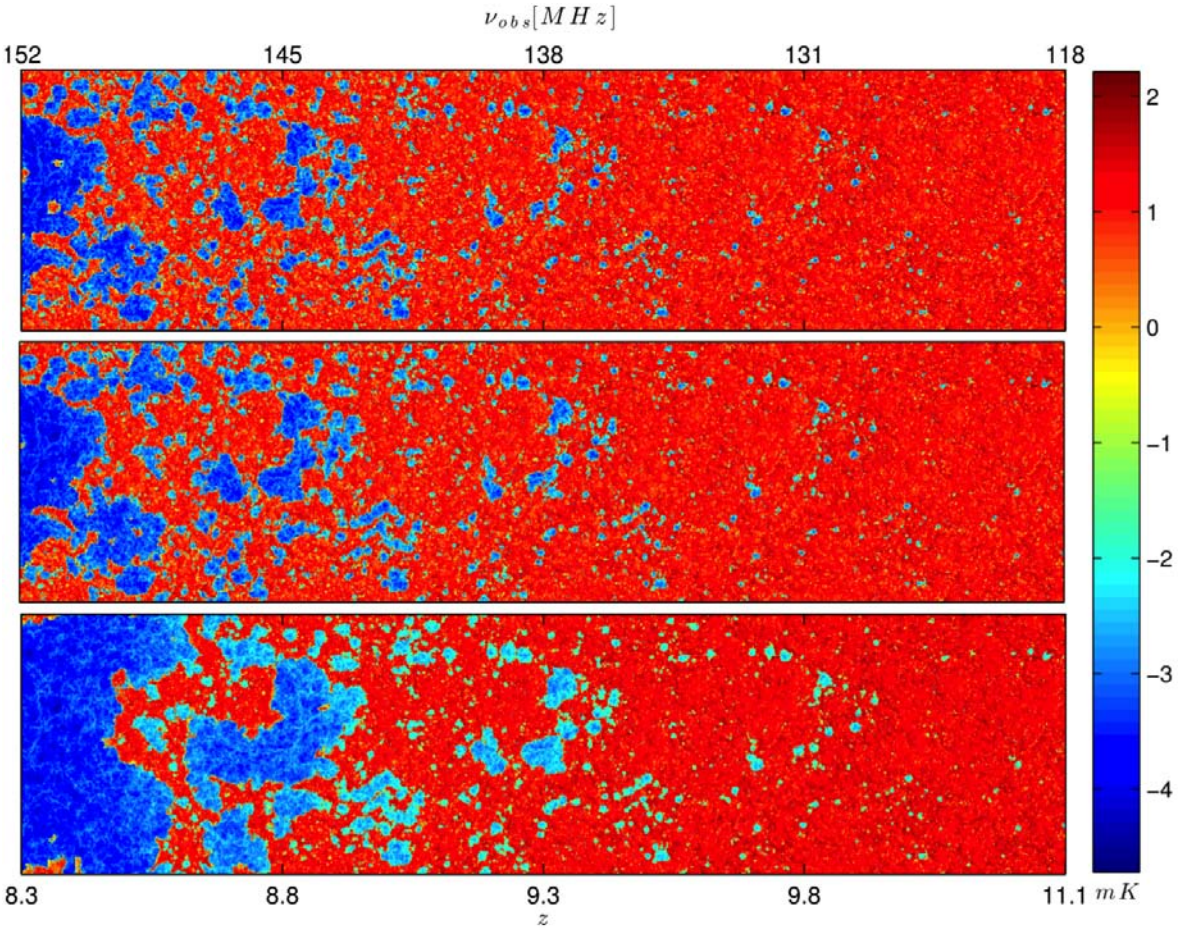

Figure 7.10: From the top are the three images from simulations LLS2, LLS1, and L1 for the box size 114 h^{-1} Mpc . The images depict the position-redshift/frequency ionization brightness temperatures. The abscissae of the images correspond to redshift range from z = 8.3-11.1 and equivalent observational frequencies (ν_{obs} [MHz]). The ordinates of the images are the comoving spatial dimension of 114 h^{-1} Mpc and 4 times that in the abscissa. The images show the differential brightness temperature in log scale (log_{10} δT [mK]) at the full grid resolution. The images are corrected for redshift-space distortions due to the peculiar velocities.

7.2.2 Evolution of the patchiness

The Figure 7.10 shows slices through the simulation cubes along the redshift (frequency) axis. The ionized fraction of the simulation cubes is converted to the 21-cm emission

differential brightness temperature, shown in log scale in mK, for the three models, shown from the top, L1, LLS1, and LLS2. For the desired range of redshifts, the data from the cubes is interpolated along the redshift/frequency axis. The interpolation is performed along the plane with an oblique angle of 10° across the cubes in order to observe different structures along random line of sight. The simulation evolves the same volume over time and therefore has same H II regions spatially distributed. To interpolate across them along the same coordinates will generate evolution image of the region with repetitive features unlike what the telescope arrays will observe. A slice at an angle captures different features and mimics a relatively realistic image along the ling of sight. The neutral regions are shown in red and the H II regions cover the dynamic range through blue as shown by the color bar of the Figure 7.10. No corrections for the redshift space distortions are applied.

In Figure 7.10 it is evident that at high redshifts the H II regions are small and distributed sparsely. These regions closely trace the ionizing halos. The effect of the different mfps of the the three models on the ionization becomes visually evident at redshift $z \sim 9.8$ increasing with lower redshifts. The H II regions for the three models grow and merge at different pace. For this reason by redshift $z \sim 8.3$ the L1 model is fully ionized while the models with LLS the mass weighted global average ionization for LLS1 is $\langle x_m \rangle \sim 83\%$ and LLS2, $\langle x_m \rangle \sim 78\%$. The spatial axis at redshift $z = 9.457$ subtends an angle of $\sim 0.97°$ in the sky with each pixel of $13.76''$. Without any astrophysical and instrumentational propagation effects the H II regions at lower redshifts are large enough to be directly observed by arrays with $\sim 1'$ angular resolution capabilities. The effect of the observation due to synthesized beam smoothes the fine structure but the statistical measurement of the temperature is still achievable.

7.2.3 Power Spectrum of 21-cm

The differential brightness temperature distribution, δT_b, is defined as,

$$\langle \widetilde{\delta T_b^\star}(\mathbf{k}) \widetilde{\delta T_b}(\mathbf{k}') \rangle = (2\pi^3) P_{21}(\mathbf{k}) \delta_D^{(3)}(\mathbf{k} - \mathbf{k}') \tag{7.4}$$

where, $\widetilde{\delta T_b}$ is the Fourier transform of the differential brightness temperature, $\widetilde{\delta T_b^\star}$ is the complex conjugate, P_{21} is the spherically averaged power spectrum, and $\delta_D^{(3)}$ is the three-dimensional Dirac delta function representing the sampling function of the Fourier

transformed quantity. The power spectrum is in the units of mK^2 and is also used in the dimensionless form as following,

$$\Delta^2_{21\text{-}cm}(\mathbf{k}) = \frac{k^3}{2\pi^2} P_{21}(\mathbf{k}) \quad [\mathrm{mK}^2] \tag{7.5}$$

There are various schemes for estimating the power spectrum. In this paper, the results from the *mesh-to-mesh real-to-redshift-space mapping* (MM-RRM) methodology [Mao et al., 2012] are used. Also see Appendix B. The MM-RRM uses the ionization fraction, density, and velocity files as input to estimate the power spectrum. This methodology takes into account the effects of redshift space distortions and predicts accurate estimates of the 21-cm background with the caveat that at $k_N^{256}/4 < 1.75^{-1}$ $\mathrm{Mpc}^{-1}\mathrm{h}$ the errors in the estimated PS are large.

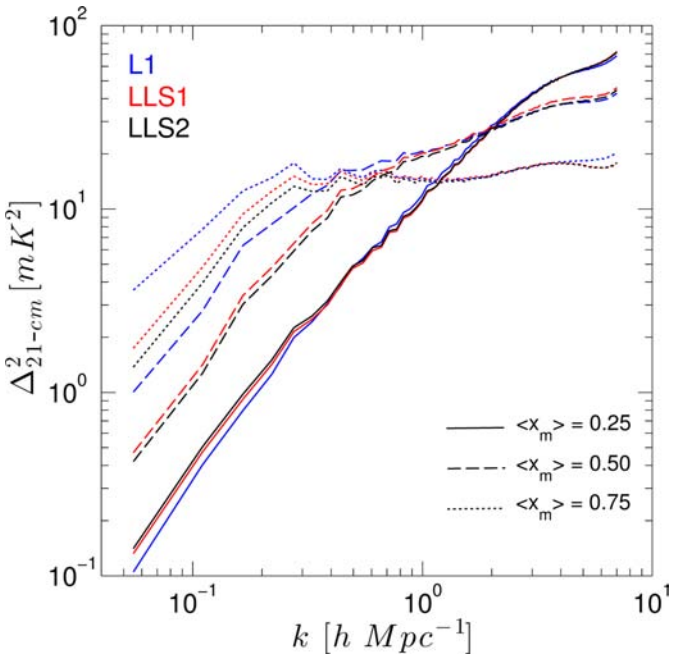

Figure 7.11: The 3-D spherically averaged 21-cm differential brightness temperature fluctuation power spectra for models L1 (blue), LLS1 (red), and LLS2 (black) at mass weighted global ionization of 25% (solid lines), 50% (dashed lines), and 75% (dotted lines).

The measurement of the power spectrum lends itself naturally to the radio interferometric observations since the visibilities of the interferometric measurement are sampling the Fourier transform of the sky and the power spectrum is the Fourier transform of the two-point correlation function.

Figure 7.11 shows the 21-cm dimensionless differential brightness fluctuation power spectra

of the three models at three representative stages, global ionization average of 25%, 50%, and 75%, of the reionization. The most distinct characteristic visible in the figure is that the fluctuations in the brightness temperature at large scales ($k < 2$ Mpc^{-1}h) grow by two orders of magnitude for the fiducial L1 case and less than an order of magnitude of the LLS cases. This is a signature of the larger H II regions causing larger temperature fluctuations. The smaller fluctuations, on the other hand, flatten out as the ionization progresses. Another noteworthy feature is the divergence of the fiducial L1 model with the LLS models at the largest scales of the simulations.

Figure 7.12 shows the evolution of the power spectra with redshift for the three models for two k values, 0.05 and 0.9 Mpc^{-1}h representing large and small scale fluctuations respectively.

The features in the 21-cm power spectra are consistent with the prior analyses. The recurring theme in the analysis of size and distribution of the H II regions is that for the LLS models the growth of ionized regions is obstructed and ionization is delayed. This is well captured in the 21-cm power spectra, defining implications for the upcoming experiments. For both the scales ($k = 0.05$ and 0.9 Mpc^{-1}h) the observational frequency range from 140-150 MHz is where signals peak and the models are most differentiable. For large-scales ($k = 0.05$ Mpc^{-1}h) the signal also goes to minimum in 123-127 MHz range with the lowest signal occurring for LLS2 followed by LLS1 and L1 models. While the depression in the signal is only 15% the significant difference occurs at peak with L1 rising by 27% and 31% excess for LLS1 and LLS2 models. As can be noted, the difference between the two models is 0.63 mK^2. For small-scales ($k = 0.9$ Mpc^{-1}h) the spectra peaks very early on at $z = 17.85$ corresponding to redshifted 21-cm at 75 MHz. This is region of the power spectrum where the models are virtual identical. The next peak for the small-scale features tracks the large-scale but occurs slightly earlier at 133 MHz range with the corresponding dip occurring at 117 MHz.

It is discernible in the evolution of the power spectrum, both at small ($k = 0.9$ Mpc^{-1}h) and large-scales ($k = 0.05$ Mpc^{-1}h), that the peak in the power are delayed for the LLS cases. This lag in the ionization process is due to the longer mfp of the ionizing photons

in the dense LLSs. The delay in the overall ionization is also evident in the figure with the peaks for non LLS case rising at earlier times followed by models LLS1 and LLS2 in that order.

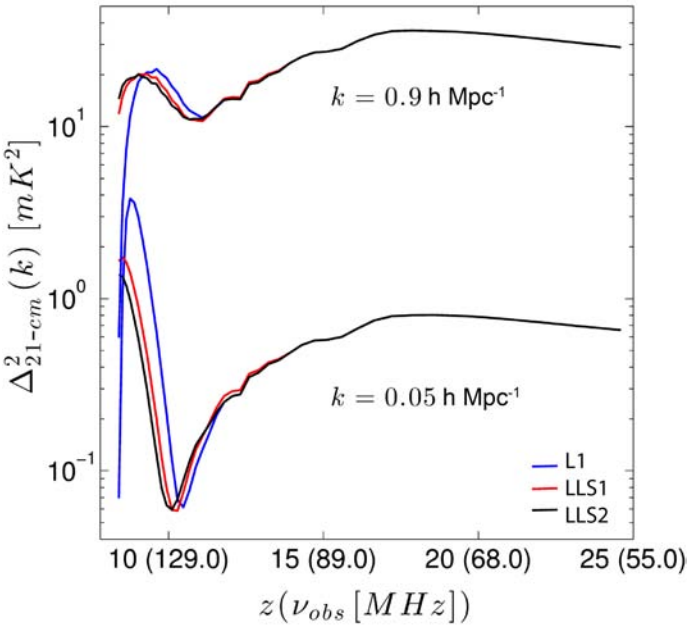

Figure 7.12: The time evolution of the two k-modes, $k = 0.05$ and 0.9 Mpc^{-1}h of the spherically averaged 3-D power spectra of the differential brightness temperature fluctuations for the three models.

The power spectrum contains a wealth of information on the clustering and the nature of the ionization sources. The Figure 7.13 shows the complete evolution of the power spectrum for the no LLS case (top, L1) and the differences with the LLS models (bottom two; LLS1 - L1 and LLS2 - L2). The image in the top row shows that the maximum power in the power spectrum shifts from lower to higher wave numbers as the ionization progresses, peaking around 50% ($z \approx 9.5$). The bottom two rows depict the difference of the power spectra evolution at ionization rates of the L1 model given as LLS1 - L1 and LLS2 - L1 respectively. It is evident that the differences between the no LLS and the two LLS models appear later in the ionization history. As can be seen from the Figure 7.12, the power spectra remain the same at different k-modes and any differences emerge around redshift $z \sim 15$. The negative features in the bottom two figures of the Figure 7.13, shown in blue, are indicative of the lower values of the LLS power spectrum at lower k values in the later times. Higher power spectrum values at lower k means contribution from smaller H II regions. This means that for the LLS models that show delayed ionization many small H II regions have not formed yet. This result is consistent with the visual inspection of the

H II regions in the bottom row of the of the Figure 7.4. This difference is relatively reversed at higher k values. In fact, the difference is significantly positive suggesting higher power spectrum values for the LLS models. This again is consistent with the delayed ionization scenario. The power spectrum peaks for the two models is delayed to later times and thereby shown in the higher k and later times in Figure 7.13.

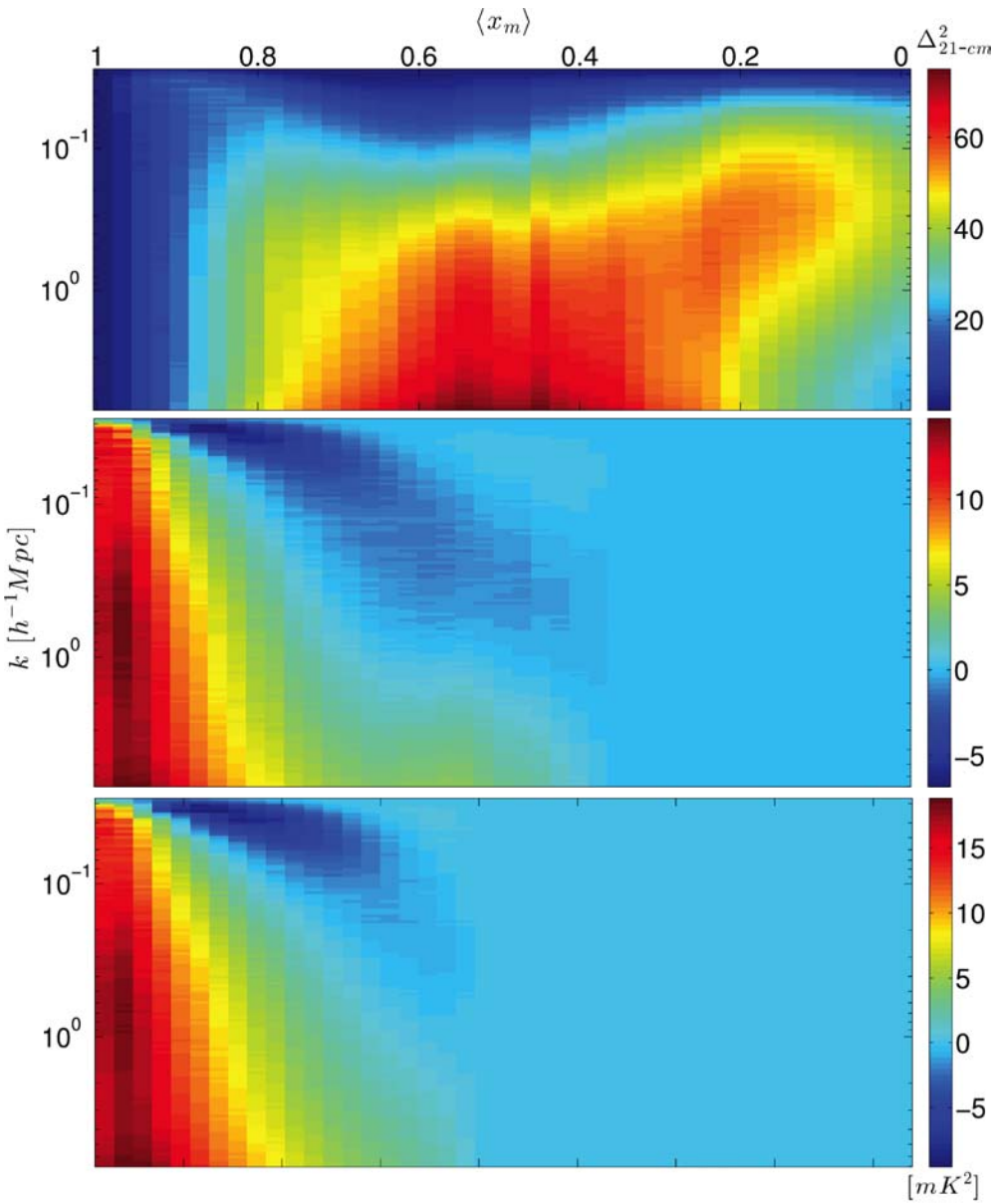

Figure 7.13: Evolution and differences between the power spectra for the different models. From top (a) The power evolution for the L1 model (no LLS). The ordinate is the k-mode, the abscissa is the ionization rate, and the color represent the power spectrum amplitude. (b) Difference of the LLS1 - L1 evolution, and (c) the difference of LLS2 - L1.

7.3 Conclusions

We have presented the results of the first large-scale (114 h^{-1} Mpc) numerical simulation, with volumetric dynamic range of the order 10^7, of the epoch of reionization in the presence of the LLSs. The LLS models are implemented in C^2-Ray using the various low-redshift observational data, namely, Songaila and Cowie [2010] and McQuinn et al. [2011]. We have analyzed the data with different techniques to explore the underlying physics defining the size distributions, morphologies, and growth rate of the ionization process in the presence of LLSs and to establish the efficacy of the observable parameters such as the brightness temperature fluctuations and 21-cm power spectra.

(i) We note that by introducing the dampening effects of the LLSs on the ionizing photons, the ionization process is delayed by$\Delta\ z \sim 0.8$ (for 99% ionization) for both the LLS models as compared with the fiducial non-LLS model.

(ii) The integrated optical depth, $\tau_{\rm es}$, due to Thomson electron scattering is diminished by ~ 0.002 for both the LLS models in agreement with the fact that in the case of LLS there are lesser number of electrons available for scattering the CMB photons. The calculated values are within the 1-σ deviation of the WMAP-9 observations.

(iii) The photon statistics analyses show that by the time the ionization is complete, there are twice as many photons per baryons for the LLS case. The difference between the LLS models is small.

(iv) The topological differences between the large H II regions in the three models are observable at $\langle x_m \rangle = 0.5$ indicating slow merger due to LLS. The morphology further quantified by using the statistical measures of the size with friends-of-friends, spherical averaging, and power spectrum. The friend-of-friend analyses show that in all the simulations at $\langle x_m \rangle = 0.1$ two distinct populations of H II regions emerge. However, this dichotomy diverges faster for the fiducial L1 case. The spherical averaging also show that by the ionization rate of 50-70%, the radii of the H II regions for the no LLS case are larger by a factor of 2-3.

(v) The 21-cm brightness temperature power spectra highlights an order of magnitude difference in fluctuations at large scales ($k < 0.1$ $\rm Mpc^{-1}h$). The evolution of the

power spectra also highlights the 140-150 MHz observing window for higher signal-to-noise and possibility, if any, for distinguishing the LLS models.

(vi) The peak value of the RMS of the brightness temperature fluctuations for the L1 model (no LLS) is 6.06 mK. This is decreased by about 9% due to the presence of LLS.

(vii) We also note that while the sizes and mergers of the H II regions are impeded by the presence of LLSs, the "freeze out" of the size as reported in [Sobacchi and Mesinger, 2014] is not observed. In the FoF and Spherical averging methods we have shown that the largest H II regions reach the entire simulation box sizes at the end for both LLS models.

The two LLS models discussed are based upon observational data and parametrized to yield different mean free paths and column densities. We have seen throughout our analyses that even though the model without the LLS is distinguishable from the ones with LLS, it is non-trivial to differentiate between the LLS models themselves. As noted in the beginning, this study is limited by the observational data and thereby the computational modeling. Improvements in either can only enhance the overall studies and help fine-tune the future experiments. In addition, a more in depth study on the prospects of imaging H II regions with SKA-class telescopes in the presence of instrumentation effects is in preparation [Shukla et al., 2014] and will complement the presented study.

Chapter 8

SIM Response

This section employs SIM to explore the instrument response to the input data. As we have demonstrated in the previous sections, the input data consists of the propagation effects due to extragalactic and galactic foregrounds. The additional effects due to ionosphere and the instrument, such as gains, pointing errors etc., are incorporated in the visibility prediction process. We pursue a systematic approach to study the propagation effects by introducing the effects piecemeal to the input data and estimate the loss of the true underlying signal. The overall effect due to most of the propagation errors is eventually estimated. The input data is used as slices and frequency integrated cuboid. The single slice from the data cubes integrated for 1 MHz are computationally manageable and sufficient for various studies, while the cuboids with 1 MHz bandwidth channels help explore the realistic multichannel simulations. The two telescope configurations used for the studies are the LOFAR and SKA1-LOW 10%. The LOFAR configuration was used only for testing and validation of the SIM and does not represent the part of the studies. Details of the techniques and results are expanded upon in this chapter.

8.1 Results

We demonstrate the efficacy of the SIM framework by applying it to the various topical studies. We start with the uncorrupted image of the RMS sky model as observed by various configurations and subsequently apply propagation effects to estimate degradation of the original signal. We use the robust image metric developed in this research, the spherically averaged spatial spectrum (SASS, to analyze image quality. The two primary studies we conduct are the effects of varying the core size and the calibration with the extragalactic

foregrounds.

8.1.1 Sky Model

The CubeP^{3}M and C^2-Ray output are coeval cubes of size 425 h^{-1} Mpc covering the redshift ranges from $6.5 < z < 30$. Details of the simulation are listed in Table 5.1. The data in the coeval boxes after the radiative transfer are in the form of normalized ionization fraction ranging from 0-1 (not ionized - to fully ionized). For the EoR studies the volume at redshift $z = 8.515$ which corresponds to the redshifted 21-cm at $\sim$ 150 MHz is used. The angular size, the bandwidth of the box, and other relevant observational parameters are given in Table 8.1.

$L_{\rm box}$	425 h^{-1} Mpc
Pixels	$504 \times 504 \times 504$
z	8.515
$\Delta\theta_{\rm box}$	3.74°
$\Delta\theta_{\rm pixel}$	26.73″
$\Delta\nu_{\rm box}$	34.38 MHz
$\nu_{\rm obs}$	149.3 MHz
$\langle x_m \rangle$	0.21

Table 8.1: Observational parameters for the science data for the EoR studies.

For the imaging studies with SIM, a zero mean 1 MHz slice is constructed from the box and converted to brightness temperature given in Kelvin (K) and Jansky (Jy) shown in Figure 8.1. The global average ionization rate by mass, $\langle x_m \rangle \sim 21\%$. A large H II region of size 22 pixels (9.5′, 18.55 h^{-1} Mpc) is visible south of the center of the image.

8.1.2 Units

Before we examine the results, it is important to define the units in the images. All the images are dirty images unless explicitly specified. The images are corrected for beam area to convert the image units from Jy/Beam to Jy. This is explained briefly in the next section. This conversion is relevant when the output from different synthesized beams is measured. For example, in the case of comparison of the different core sizes. In some cases, for the same beam, the results are left as Jy/Beam. For validation purposes in the section 8.1.4 we recover the image and convert it to Jy and K to demonstrate the validity of the output. Note that the Jy recovered are not exactly the same as the RMS image. That is because the sampling function is not complete.

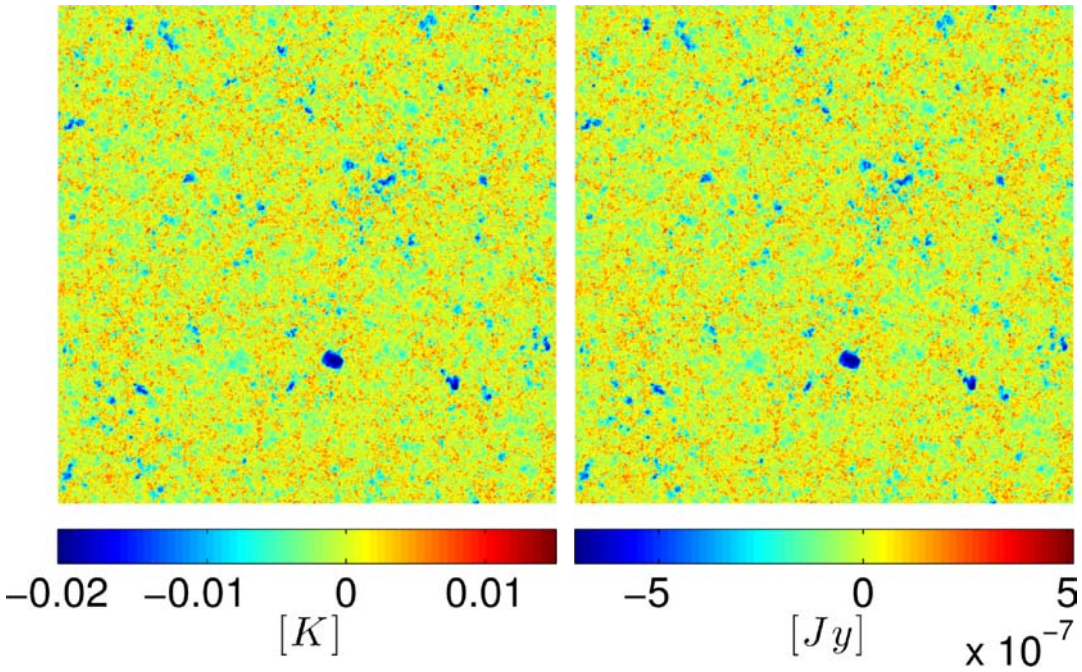

Figure 8.1: 3.74° × 3.74° (504 × 504 pixels), ionization image integrated for 1 MHz from left (a) in K, and (b) in Jy.

8.1.3 Uncorrupted Dirty Image

At the outset, we build, what could be considered as, the diffraction limited image of the RMS science model. The images are the convolution of the EoR signal sky model with the synthesized beams.

The Figure 8.2 shows the uncorrupted dirty image of the sky signal as observed with the SL10 configuration using the full array and only the core. The units of the images are in Jy/Beam. The synthesized beams for the full and the core configuration of SL10 are estimated to be BMAJ: 102.37″, BMIN: 81.2759″, BPA: 104.973°, and BMAJ: 176.018″, BMAJ: 142.97″, BPA: 91.3783° respectively. The higher flux in the image with only the core is due to the larger convolution kernel (beam area). The images are at the same resolution as the sky model shown in Figure 8.1 with 3.74° × 3.74° (504 × 504) pixels.

The synthesis images are corrupted due to various propagation effects. In the following sections, we add/multiply various additive/multiplicative errors, due to the propagation effects, to the visibilities and study the degradation of the resulting images. These effects are UV-plane effects and therefore are applied to the visibilities.

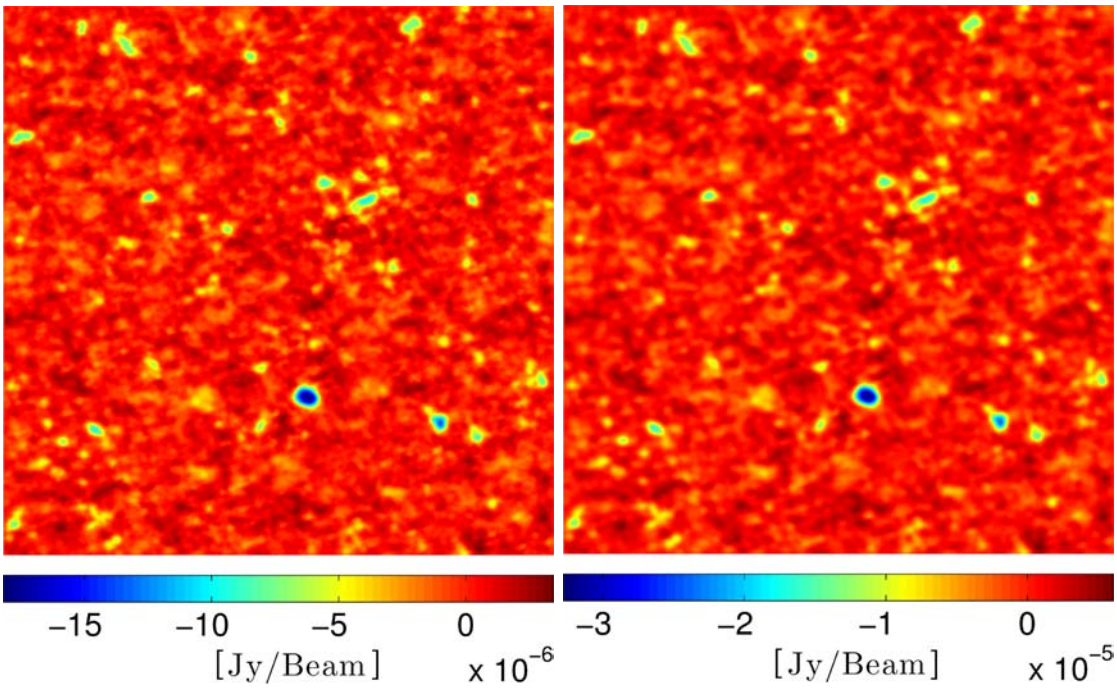

Figure 8.2: The dirty image with the SL10 configuration for the full (left) and the core (right) configuration.

8.1.4 Recovered Image

The flux of the input image in the SIM framework is in the units of Jy. The flux of the output image is in the units of Jy/Beam, where Beam corresponds to the area of the synthesized beam. In order to compare the output image with the input image to attain the factor of the recovered flux, the output image is converted to the units of Jy. This process is performed in two stages. Firstly, the output image is deconvolved using `CSCLEAN` algorithm. Secondly, the full width half maximum (FWHM) of the synthesized is measured and the beam area is estimated using the area of the beam as reported by the `CSCLEAN` algorithm. Figure 8.3 shows the recovered image for SL10 CORE in the units of Jy after corrected for the synthesized beam (BMAJ: 176.018″, BMAJ: 142.97″, BPA: 91.3783°). The recovered flux is of the order of the 10^{-7} Jy, same as that of the input image. See, Figure 8.1(b). While the deconvolution is fundamental in obtaining high fidelity images, the inherent assumptions in the deconvolution algorithms add artifacts in the final image [Yatawatta, 2010]. To avoid any spurious effects, all the comparisons, unless explicitly specified, are performed on dirty images without any deconvolution.

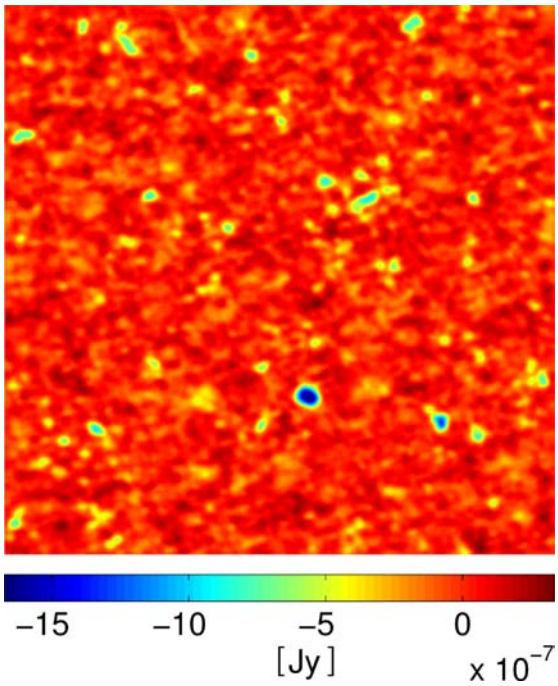

Figure 8.3: The recovered image with SL10 Core in the units of Jy after deconvolution and correction for beam area.

8.1.5 Sensitivity with varying Core sizes

The sensitivity, that is the detectability of the weakest signal, of the interferometric arrays is dependent on the antenna performance metric measured as the system flux density $SEFD$ in the units of Jy. The $SEFD$ is directly proportional to the system temperature $T_{\rm sys}$ and inversely proportional to the collecting area of the telescope. The thermal noise, σ_{ij}, per visibility with two antennas i and j is given as [Thompson et al., 2001],

$$\sigma_{ij} = \frac{\sqrt{2}k_{\rm B}}{\eta\sqrt{\Delta\nu\ \tau}}\frac{T_{\rm sys}}{A_{\rm eff}} \qquad [\rm Jy] \tag{8.1}$$

where, $k_{\rm B}$ is the Boltzmann's constant, η is the efficiency of the telescope,$\Delta\ \nu$ is the complex correlator bandwidth, τ is the integration time, $T_{\rm sys}$ is the system temperature, and $A_{\rm eff}$ is the effective area of the telescope. The system temperature for SKA Low-1 is given as, $T_{\rm sys} = 60\lambda^{2.55} + 40$. In our noise calculations we use 400 K for 150 MHz observational frequency.

For higher signal to noise, the integration times are increased and we study the case for 100 and 1000 hours of observations. In addition, we also account for the missing 779

antennas from the core. The thermal noise estimates for the cores are given in Table 8.2. These noise estimates are for 1 MHz correlator bandwidth, and 30 s integration times. The efficiency of the system is optimal and is 1 for antennas (stations) of diameter 35 m.

Configuration	σ [Jy]		
Core	10 hrs	100 hrs	1000 hrs
SL10	1.48×10^{-2}	4.68×10^{-3}	1.48×10^{-3}
SL10-2x	3.70×10^{-3}	1.17×10^{-3}	3.70×10^{-4}
SL10-0.5x	5.92×10^{-2}	1.87×10^{-2}	5.92×10^{-3}

Table 8.2: The RMS (thermal) noise for the cores of the three configurations for three different integration times.

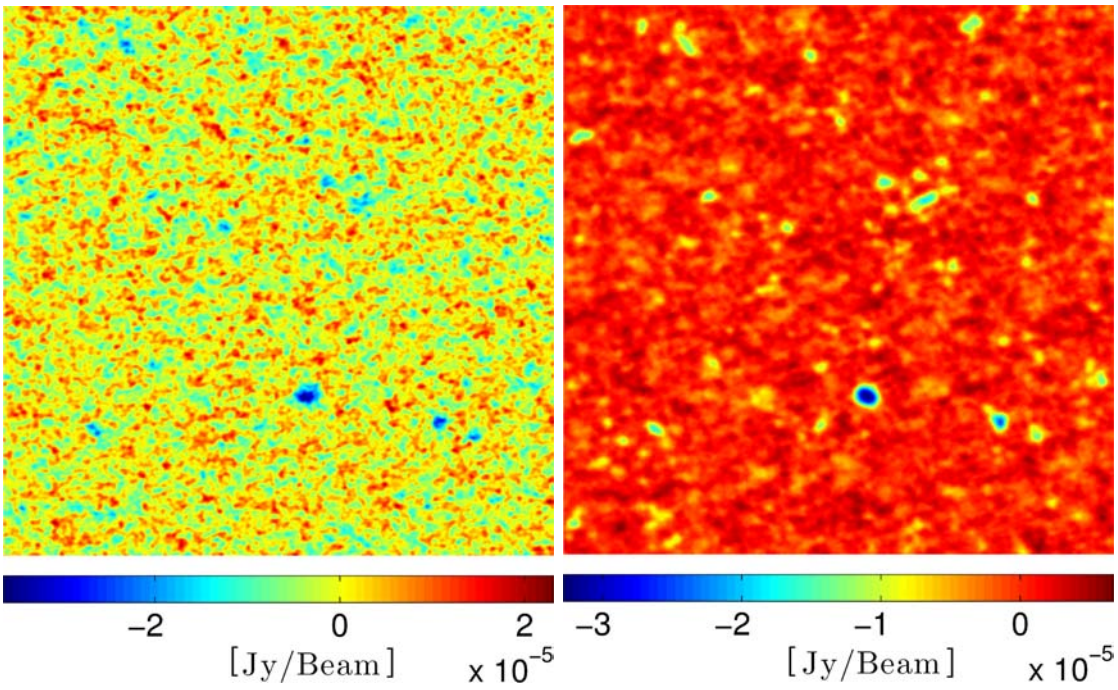

Figure 8.4: The dirty image of science data with thermal noise for the SL10-Core configuration for (left) 10 hours, and (right) 1000 hours integration time. The images are scaled for total of 866 antennas.

Upon adding the noise to the visibilities we can generate the dirty images for 10 and 1000 hours integration time as shown in Figure 8.4. The visual inspection itself differentiates the two images with the thermal noise degrading the signal significantly (left). By increasing the integration time the signal reaches almost the original signal as shown in Figure 8.2 (right).

The spatial spectrum of the images from Figure 8.2 as compared with that of the RMS

signal is shown in the Figure 8.5. Also shown in the figure is the size of the H II region at $k \sim 0.23$ [Mpc^{-1}]. For 1000 hours of integration the core traces the RMS structures exactly up to $k \sim 0.35$ [Mpc^{-1}], whereafter, the smaller structures are lost in the thermal noise. Coincidentally, the H II region lies below the threshold and is observable at the RMS level. For the 10 hour integration as expected the noise dominates the signal along all the scales.

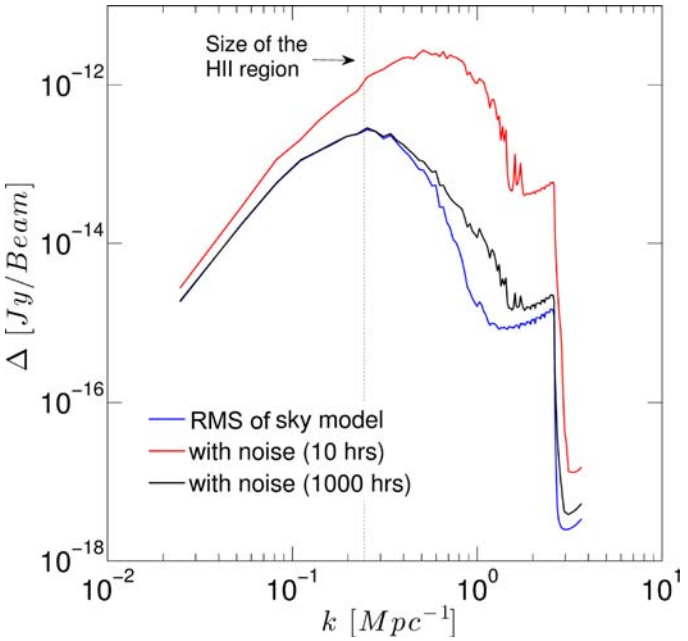

Figure 8.5: The spherically averaged spatial spectrum of the RMS sky model compared with thermal noise for 10 and 1000 hrs as observed by the SL10 Core. The line in the middle depicts the size of the H II region in the original science data. See Figure 8.1.

The general observational strategy is to observe the field(s) of interest with the core and use the arms (longer baselines) for calibrating the extragalactic foregrounds. The sensitivity of the core is increased by increasing the density or the filling factor. It will take 22k 35 m stations to reach the 100% density for the core area of the Baseline Design SKA Low-1. In the current design the core has 866 antennas. Using this as the fiducial model we explore the performance of 2× and 0.5× the core diameter. Theses models are defined in the Table 6.2 and named SL10-2x and SK10-0.5x respectively. Note that the collecting area scales as 4× and 0.25× respectively.

Based upon the thermal noise per visibility as listed in the Table 8.2, it is evident that the performance of the SL10-2x is far superior to the other models even at 10 hours integration time. However, assuming that the cost of a station scales linearly, that performance comes

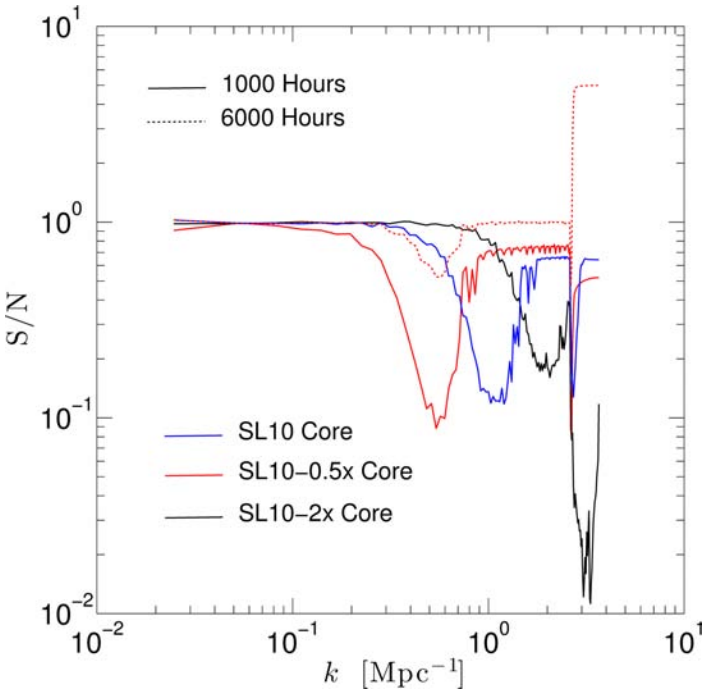

Figure 8.6: The performance of the the Core models for 1000 hrs of observing for all the three Core configurations. Also added is the 6000 hrs observation with the SL10-0.5x Core. Note that the S/N is in the Fourier domain and is the measure of spatial frequencies.

at 4 times the cost.

The Figure 8.6 shows the comparative performance of different core models as the ratio of the diffraction limited image and the image with thermal noise. Note, that this signal-to-noise (S/N) is in the Fourier domain and not to be confused by the image plane S/N which is traditionally used in literature. The noise response in the Fourier domain is distributed by the uv-sampling function across the k-scales. The amplitude of the noise varies based upon the initial value added per visibility. A detailed response of noise based upon the weighting of the uv-sampling is discussed in the next section 8.1.6.

The Figure 8.6 shows the performance for 1000 hours of observation for all the three cores. In addition, 6000 hours of observation is also shown for the SL10-0.5x Core. The results are beam corrected, converted from Jy/Beam to Jy, for both the signal and the signal with noise. The SL10-2x core is significantly sensitive to smaller scales compared to the other two models; roughly 2.6 times more wave-numbers as compared with the SL10 Core 1000 hours. SL10-0.5x in comparison with 1000 hrs of observation time has poor performance and can recover signal above 90% only for large scales with $k > 0.13$ Mpc^{-1}. The 6000

hours observation with the SL10-0.5x is plotted in dashed line. This is an interesting result because the performance of SL1-0.5x core with 6000 hrs is comparable with that of the SL10 core. But more importantly the value performs at much smaller scales. The value of $k = 1.73$ is roughly 3 pixels. The increased integration time results in significant increase in performance for the smaller core both in recovering the signal and resolution for the relevant scales. Naively, at quarter the cost of SKA Low-1 a 750 day (assuming 8 hours a day cadence) observational campaign could recover the EoR signal. However, the longer timeline introduces additional competing complications (primarily temporal changes in calibration, ionosphere modeling etc.). In the phase-space of integration time, core size, and costs there maybe a single or multiple minimum. This study, however, provides a first order estimate by bookending the phase-space with extreme boundary values. Depending upon the science drivers decision of expanding the core size will allow for sensitivity to smaller structures in the neutral hydrogen ionized field. However, for scales $k < 0.35$ Mpc^{-1} the baselines design reaches the threshold in 1000 hours of integration time. The decreased size gives the better performance with six times the increased integration time. The 21-cm power spectrum for the used data shows increasing power at larger k-scales. See the first panel on the left of the figure 15 of Iliev et al. [2014]. The probably distribution of H II regions for the used data peaks at radius of 0.63 Mpc. At $z = 8.515$ (150 MHz), the angular size of the H II region is about $0.50'$. None of the cores will resolve these size H II regions. However, the $\log_{10}$ R dp/dR distribution also illustrates 25% H II regions of size $2'$ and about 10% regions of size $6'$ corresponding to $k \sim 0.7$ [Mpc^{-1}]. This is the a region in the Figure 8.6 where the performance of both SL10 and SL-0.5x cores is not optimal. It should be noted that this is a single observational frequency study. At lower frequencies the H II regions will be smaller and the beam sizes with increase. As a future study, beyond the scope of this thesis, we will explore H II region size and beam relation to gauge the core size metric.

8.1.6 Beam Shapes (Tapering)

The performance of a telescope is measured by the sensitivity and the shape of the synthesized beam. A preliminary study by Braun [2014] for SKA 1 mK RMS for 1000 hours on 1 degree angular scales at 50-150 MHz range. This sensitivity will allow the detection of the individual fluctuations.

In this section we use the SL10 Core layout to explore similar metrics. We generate variance-limited noise maps for four different density weighting and tapering and compare the results. The noise are estimated for 1000 hours for the single channel at 150 MHz. The Figure 8.7 shows the comparison of noise maps as compared to the RMS signal for the uniform and natural weighting. The 300″ Gaussian taper as mentioned in Braun [2014] is also included.

The figure shows the results of different sizes of the FWHM for uniform weighting as with the noise for 1000 hrs. From the figure it is evident that the FWHM of the Gaussian taper ranging from 10″ to 1000″ recovers the signal differently. The dichotomy of the sensitivity to the structure size is again visible for all the beam tapering. However, 300″ FWHM recovers the signal at all the scales which is seen in the left panel as well.

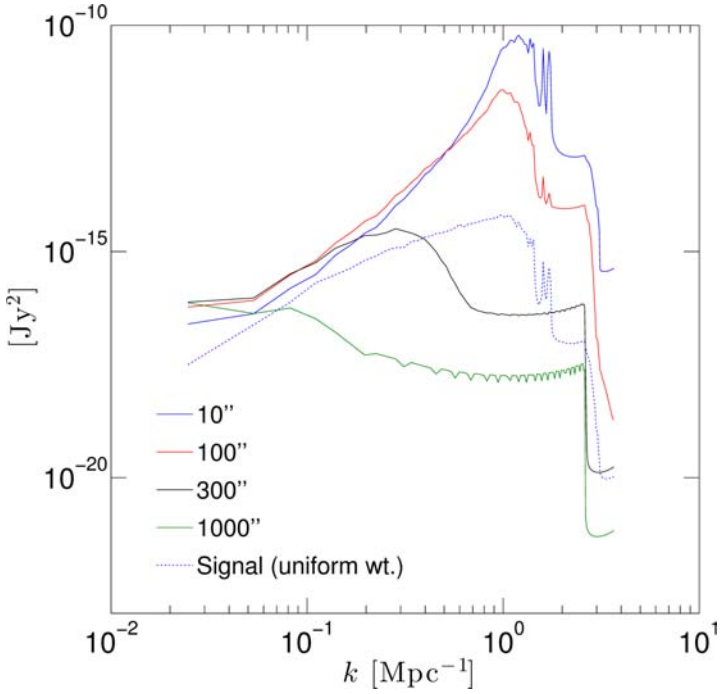

Figure 8.7: Tapered variance-limited noise as observed with SL10 core with different Gaussian tapering for 150 MHz. The RMS signal with uniform weighting is also plotted (dotted line) for comparison.

8.1.7 Calibrating Gain and Phase Errors

The other source of corruption in the visibility plane is due to the gain and phase errors. These errors are due to the variations in the response of the receivers due to temporal

changes in the instrument (electronics, for example) and the atmosphere. In the RIME formalism these errors are defined by the **G** Jones matrix which is a diagonal matrix of complex gain terms per receiver. The gains and phase errors are added to the signal and are defined in the Table 8.3. The signal in this case is the EoR signal plus the zero-mean extragalactic foregrounds along with the thermal noise for 1000 hrs of observation.

Periodic Gains	
Min Gain	0.5
Max Gain	1.5
Min variation / hr	1.0
Max variation / hr	5.00
Phase Errors	
Max Error	120°
Max variation / hr	0.01°
Min variation / hr	0.02°

Table 8.3: Gains and Phase errors as added to the signal.

Before we apply the errors to the data and solve for the calibration solution, see Equation 8.2, it may be useful to review some of the methodologies applied. Recall that in the RIME formalism, the propagation effects are represented as the components of the Jones' chains closely following the physical processes. Smirnov [2011b] has concluded that that such a chain could be reduced for the number of solvable terms by introducing the phenomenological RIME that consists of macros of Jones' matrices representing multiple effects. For example, the phase errors due to the atmosphere (T-Jones) and the antenna/receiver gains could be collectively represented by the 2×2 **G**-Jones matrix. It must be noted that only the terms that commute form the phenomenological RIME terms. In addition, the terms obtained analytically may also be included in the collective form.

The process of calibration involves building a Sky model and fitting it to the observed data. The fitting is a form of non-liner least squares. What is fitted (solved for) are a set of parameters $\mathbf{p} \equiv (p_1, ..., p_k)$ such that the difference between the model $M(\nu, t; \mathbf{p})$ and

the data $D(\nu, t)$ is minimized in the Chi-squared sense,

$$\chi^2(\mathbf{p}) = \sum_{ij} w_{ij}^2 \ (D_{ij} - M_{ij}(\mathbf{p}))^2 \tag{8.2}$$

where, w_{ij} are weights. There are a wide range of solvers for the above equation. In MeqTrees, the gradient descent Levenberg-Marquardt algorithm is used to minimize the equation. In practice, the Sky model for extragalactic foregrounds is build by using the full telescope, especially with the longer baselines. The general methodology is to observe the diffuse regions with the core and build the point sources models with the longer baselines. In the following calibration exercise we adopt this prescription.

The calibration solutions are obtained using two models for the extragalactic foregrounds. The first model (M1) assumes that the model of the extragalactic foreground is same as the truth. This is the extreme best case against which we will measure the second (M2) and the third (M3)calibration model (M3). The models M2 and M3 are observed with the full SL10 and baselines $>$ 2 km for SL10 configuration. The models are made from the extragalactic foregrounds alone, therefore do not have diffuse emission. The Table 8.4 shows the sensitivity of the three models.

Model	Max [Jy]	Min [Jy]
M2	1.026×10^{-4}	-4.785×10^{-5}
M3	8.948×10^{-5}	-9.953×10^{-6}

Table 8.4: Sensitivity of the calibration models.

The integrated 1 MHz data for the sky is prepared by combining the extragalactic foregrounds and the EoR signal. This data is observed with the SL10 Core. Thereafter, using the models M1, M2, and M3 the data is calibrated. The calibration falls under the 2G scheme. We are not solving for DDEs. The calibration solutions are estimated using the non-linear least squares minimization as mentioned above and the solutions are subtracted from the data visibilities in the uv-plane.

The spatial spectrum of the residual image is shown in the Figure 8.8. What is evident from the figure is that the model M3 performs relatively better at scales with $k > 0.2$. The most obvious difference between the two models is that the dynamic range of the model M3

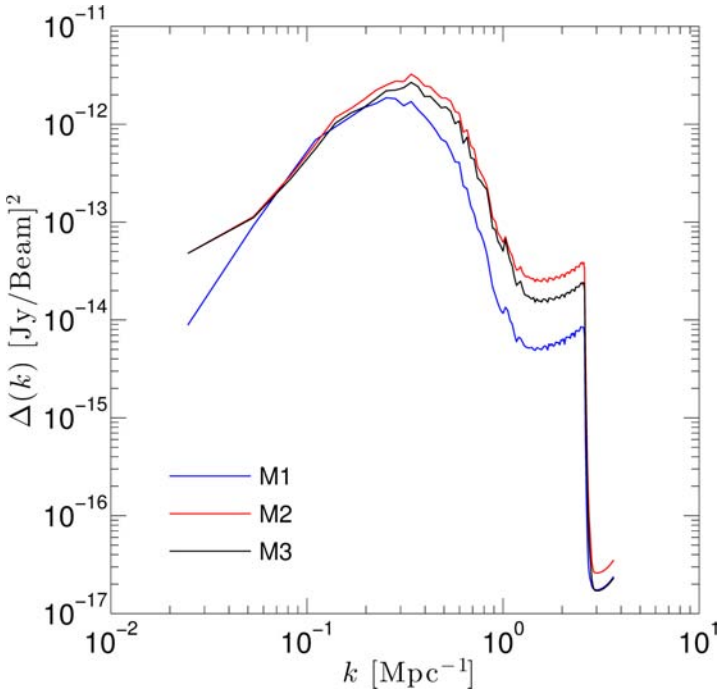

Figure 8.8: The spatial spectra of the calibration residuals with models M1 (blue), M2 (red), and M3 (red).

is 4 times that of the model M2. This brief and simple exercise demonstrates the prospects of defining the boundary limits for the sky models used for foreground subtraction. In this setup, the real sky models may be used to estimate their expected performances. Note that adding wide range of propagation effects, especially the DDEs, along with the diffuse foreground will require 3G calibration techniques.

8.1.8 Complete Data Model

In this section we build a single 1 MHz channel with the propagation effects as described by the respective Jones' matrices and thermal noise. These effects are simulated under two categories, image-plane effects, and uv-plane effects. The image-plane effects are direction dependent and require advanced calibration methods for removal. The uv-plane effects are direction independent and are antenna dependent.

In MeqTrees, the extended or diffused sources are considered as multiple discrete sources. The RIME for such a system is defined as pixelated sky of N sources. The path of the signal from each source to the antennas p and q are different. However, each path from the source (pixel on the sky), s, can be described as a standalone Jones' chain $\mathbf{J}_{sp}$ and $\mathbf{J}_{sq}$. The chain represents the matrices in the physical order of effects along the line of the signal

propagation and is represented as, $\mathbf{J}_{sp} = \mathbf{J}_{spn}...\mathbf{J}_{sp1}$. The convention of the chain follows that the outer matrix element ($\mathbf{J}_{spn}$) is at the antenna and the internal element (J_{sp1}) occurs at the source. The visibility matrix in the Equation 4.13 can then be rewritten as,

$$\mathbf{V}_{pq} = \mathbf{G}_p \left(\sum_s \mathbf{E}_{sp}\mathbf{K}_{sp}\mathbf{B}_s\mathbf{K}_{sq}^H\mathbf{E}_{sq}^H \right) \mathbf{G}_q^H + Noise \tag{8.3}$$

where, the Jones' chain is defined as $\mathbf{J}_{sp} = \mathbf{G}_p\mathbf{E}_{sp}\mathbf{K}_{sp}$ for the direction (source) independent matrix term $\mathbf{G}_p$, the direction dependent term $\mathbf{E}_{sp}$, and the phase term $\mathbf{K}_{sp}$. In this formalism the uv-plane terms are encapsulated in $\mathbf{G}_p$, and the image-plane terms are represented by $\mathbf{E}_{sp}$. The single channel data we simulate contains the following Jones' matrices in the order and the additive term due to the thermal noise,

Image-plane components

$\mathbf{N}_{\text{corr}}$ The N-correction is an alternative to the w-correction. For wide-fields, the distortions introduced by the w-effects become indistinguishable with other distortions. Correction for **N** Jones applies a term, $N = (1/\sqrt{n})e^{2\pi i w_p(n-1)}$ to add/correct for the w-projection.

Z Jones' matrix represents the ionosphere. It models the traveling ionospheric disturbances (TIDs) as a direction dependent matrix. There are various models that can be used. The ones used in this simulation has the total electron content (TEC) offset of 1 and is based on dual waves with wavelengths of 250 km and speeds of 300 km/h. The angle of the propagation of the waves is 15° counter-clockwise traveling East.

L Jones' matrix represents the time-variable parallactic angle (η) or the dipole rotation. The rotation module was used with the assumption of the equatorial mounts.

E Jones' matrix captures the pointing and beam errors. The beam model used was the default analytical model, the Westerbork (WSRT) $\cos^3$ model. The pointing errors applied are time-varying and are applied in the l, m coordinates in the sky. The maximum pointing error in both coordinates was $10''$ with variations between 1 and 2 hours.

It should be noted that the image plane components collectively are represented in the term **E** of the RIME Equation 8.3. In all of the simulations, the default values of the image components are used save for the exception of the $\mathbf{N}_{\text{corr}}$ component which is not used.

UV-plane components

G Jones' matrix captures the gains and phase errors. The models used are time-varying. The gains used vary from 0.5-1.0 in 1-2 hours period. The phase errors reach upto 60° and also vary in 1-2 hours.

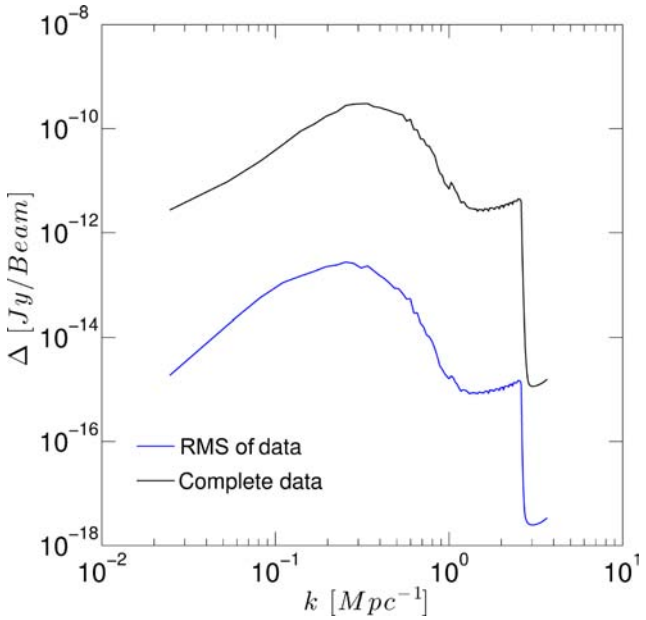

Figure 8.9: The spherically averaged spatial spectrum of the RMS EoR signal compared with the complete data model along with the thermal noise for 1000 hrs as observed by the SL10 Core.

The additive term of the thermal noise per visibility is also added for the equivalent of 1000 hours. With all the propagation effects added the simulation is performed with the SL10 Core. The result is shown in the Figure 8.9. As expected the detected signal is roughly four orders of magnitude higher than the signal of interest. What is interesting is that the features along the scales are uniquely reproduced. This dataset could be used for single channel analysis for testing various calibration and signal extraction methodologies.

The purpose of this exercise is to demonstrate the capability of the SIM framework with simple and quantifiable exercises. As the next step, using the developed tools, more

in-depth studies are currently being performed simulating realistic scenarios and data inversion mechanisms and the results will be shared in subsequent publications.

8.1.9 Dark Ages

The 21-cm radiation from earlier epoch will shed light on the foundations of the large-scale structure formation prior to the advent of the ionizing sources. This period of the evolution of the Universe is important from cosmological perspective. There is no observational data available for this period of the Universe. That in itself will be a big first step. Secondly, the primordial non-Gaussianity is less dissipated by other nonlinear dynamics during this period, therefore making it a fertile ground for such studies. In addition, this epoch is the precursor to the formation of the large-scale structures and ionizing sources making it extremely important to study. The 21-cm radiation from this region is highly redshifted leading to observational challenges plaguing the the low-frequency radio astronomy. The synthesized beam at low-frequency are larges and therefore will tend to convolve out small scale-structures of interest. The system temperatures are higher and therefore add higher noise. The propagation effects due to cosmological, extragalactic, and ionosphere are functions of frequency and further worsen the observations of the underlying signal.
This section examines a coeval box at redshift $z = 14.294$ with ionization rate of 1%. The box is taken from the same set of simulation used thus far, see Table 5.1. The observational frequency at the selected redshift is 92.87 MHz. The details of the other observational parameter is the given the Table 8.5.

z	14.294
$\Delta\theta_{\text{box}}$	3.34°
$\Delta\theta_{\text{pixel}}$	$23.88''$
$\Delta\nu_{\text{box}}$	27.11 MHz
ν_{obs}	92.87 MHz
$\langle x_m \rangle$	0.01

Table 8.5: Observational parameters for the science data for the Dark Ages studies. The size of the comoving simulation volume is 425 h^{-1} Mpc and the resolution is $504 \times 504 \times 504$.

As the first observational test, the integrated 1 MHz channel is observed with the SL10 CORE scale for 866 antennas and 1000 hours. The SEFD at 92 MHz is 2384.2 Jy and the thermal noise per visibility for 1000 hours is 3.073×10^{-3} Jy.

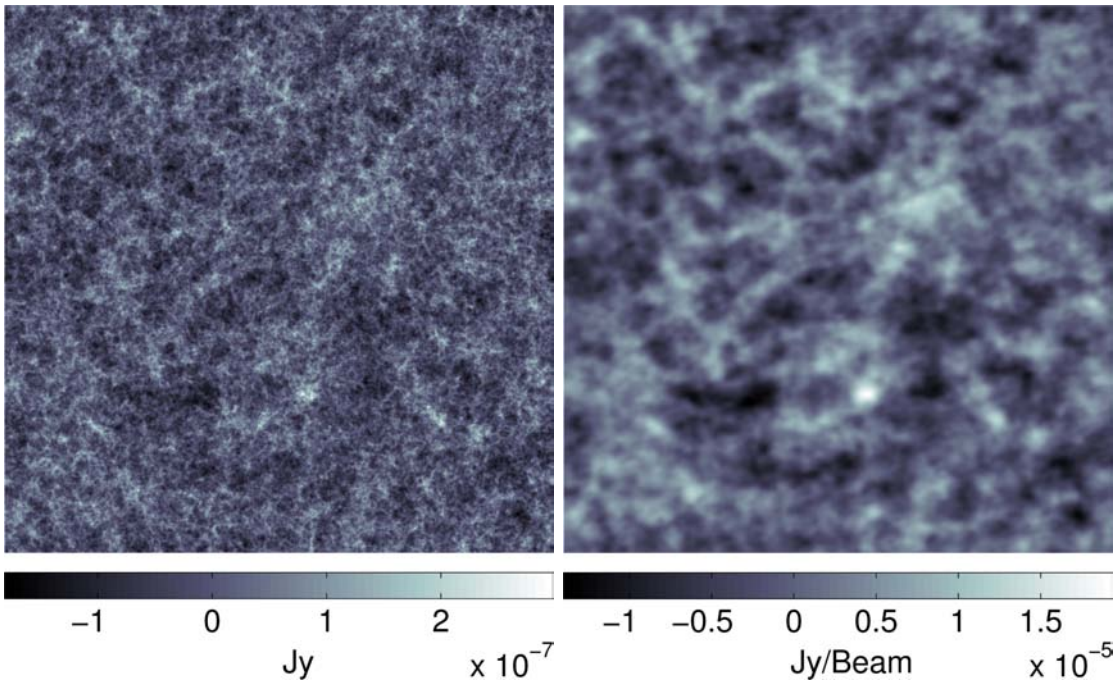

Figure 8.10: (Left) The 1 MHz channel RMS science data (neutral hydrogen) at $z = 14.294$ observed at 92 MHz with thermal noise for the SL10-Core configuration for (Right) scaled for total of 866 antennas.

The Figure 8.10 shows the integrated 1 MHz channel of the RMS sky on the left. A lot of filamentary structure in the neutral hydrogen is visible. The average ionization is barely 1%. On the right is the observed image with the thermal noise for 1000 hours. The assumption, of course, is that the foreground removal techniques are perfect and reach the thermal RMS. Upon visual inspection, the blurring is as expected due to the large beam. However, the filamentary nature of the structures is still visible. This is acutely captured by the spatial spectra in the Figure 8.11. The structures trace each other up to 10% difference for $k < 0.16$ Mpc^{-1}. Depending on the science drivers the trade-off between structure sizes and sensitivity could be estimated by adding longer baselines and additional channels. As compared to the Figure 8.5 the performance of the original BD SKA Low-1 is effective in conducting Dark Ages studies.

8.2 Current/Future Work

The SIM effort demonstrates that realistic simulation enabled by the emerging HPC technologies form the definite *third pillar* in the scientific process. As the tools, numerical techniques, programming models, and the underlying architectures advance, realistic simulations by exploring the wide phase-space of the multitude of parameters will hone in

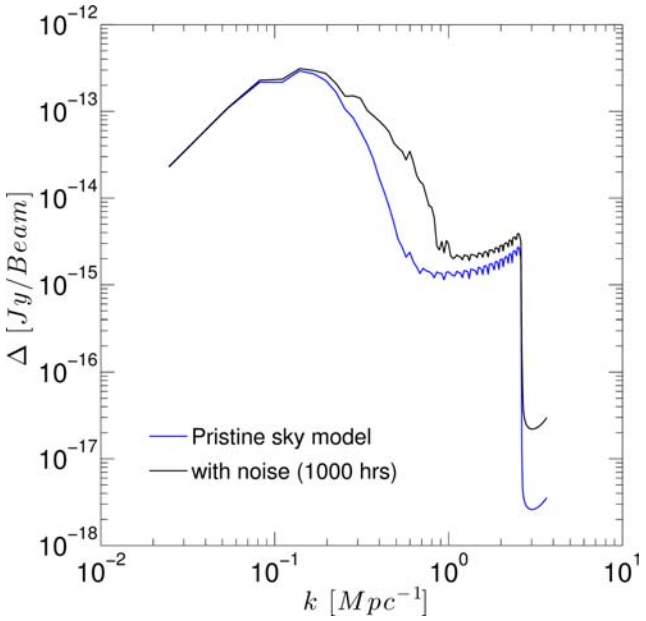

Figure 8.11: The spherically averaged spatial spectrum of the RMS sky model at $z = 14.294$ and average mass-weighted ionization of 1% compared agains t the data with the thermal noise for 1000 hrs as observed by the SL10 Core.

on optimal solutions satisfying the required constraints for future experiments. As of the writing of this document there are a few immediate ongoing efforts listed below,

Define the RMS of the foregrounds for best foreground subtraction.

Conduct 3G calibration studies on the single channel with the complete data model, specially the DDEs. Expand this to multichannel work.

Build multichannel data volumes with complete data model for blind testing of variety of emerging data processing pipelines.

I hope to continue to help the growth of the SIM components especially in compliance with HPC and adoption of massively parallel architectures. While our studies are done with the 10% of SKA-Low, increasing the number of antenna will help conduct studies where PSF accuracies are critical, such as 21-cm weak lensing. Such scaling will also help test large data solutions as they get introduced to the radio astronomy computing.

8.3 Conclusion

The next generation of large radio telescopes arrays, such as the Square Kilometre Array, will generate unprecedented amounts of data, thus severely disrupting the traditional modes of data acquisition, processing, and storage. The tools such as SIM help pave the way for testing effective methodologies of in-situ visibility processing, advanced calibration techniques, and managing resulting data volumes. The first version of SIM developed for this thesis addresses the first order of observational questions as applicable to the study of the EoR and DA. Such tools can be easily redefined to other studies.

It is noteworthy that the radio interferometry measurement equation (RIME) has exposed the opportunities for the observational simulations. The advances in HPC and scientific computing have seen sudden rise in advanced simulations of the realistic signals. SIM consolidates theses advancements and demonstrably applies them to a specific research topic.

One of the important demonstrations of the SIM tool is the study of the array configurations as applicable to the expected signal. While signal-to-noise studies provide an overview of the performance of the telescope, simulating imaging of the expected signal with proposed array configurations reveals array response in greater detail. This approach is further made realistic by incorporating more accurate models of the used propagation effects. It is conceivable to use observational data to replace models and generate less model dependent results. The modularity of these tools affords the flexibility of model exploration and constraining the models.

For the EoR observational study the approach used in the thesis was to add the contaminations to the signal piecemeal and measure the effects. While the first order studies are simplified, they clearly demonstrate the challenges in observational techniques, for example, the calibration of gain errors. A more realistic multi-channel simulation is computation limited, however, the Figure 8.9 is indicative of the single channel signal distortion when real world contaminants are added to the signal chain. The piecemeal approach allows for developing techniques for removing specific corruptions. Adding all the

propagation effects provides a fertile ground for testing out and honing those techniques.

The end-to-end simulations become far more critical when the price tags of the publicly funded experiments reach tens of billions in leading currencies. Such projects usually are multi-national, multi-year commitments thus requiring time-critical project timelines. The simulations quantify the metric needed to define these timelines. More efforts beyond the PhD thesis should be put into the development of such simulation tools by employing state-of-the-art computational techniques. Tools like SIM can generate datasets equivalent to the *first light*, very early in the project, thus precipitating the co-design and co-development of the hardware and associated software for the entire data flow. To put things in perspective, the GPU programming language CUDA is only 7 years old and is already widely adopted in the scientific HPC community. SIM provides a sandbox for testing these rapidly emerging technologies for quantifiably justifying their adoption and/or staying current with the advancements in the relevant fields.

These are extremely exciting times for the radio astronomy community. As we gear up to explore the farthest, never seen before, reaches of the Universe, we are poised to generating multitude of new techniques and technologies useful in the wide range of scientific domains. Coming years will be pivotal for the growth of radio astronomy and related HPC. It will be critical to allocate resources in this cross-domain area largely overlooked in the past. This effort hopes to demonstrate the value and the need for development in the area of realistic simulations.

Chapter 9

Constraining f_{NL}

9.1 Overview

As discussed earlier in Chapter 2 Section 2.6, the presence of primordial non-gaussianity will allow to break the degeneracy in the inflation models. So far, various methods have been deployed to estimate the dimensionless nonlinearity parameter, f_{NL}. The parameter is the amplitude of the primordial non-Gaussianity. The CMB data puts the most stringent constraints on this parameter with the latest 1-σ Planck results [Planck Collaboration et al., 2013] as, $f_{\mathrm{NL}}^{\mathrm{local}} = 2.7 \pm 5.8$, $f_{\mathrm{NL}}^{\mathrm{equal}} = -42 \pm 75$, and $f_{\mathrm{NL}}^{\mathrm{ortho}} = -25 \pm 39$. Therefore, exploring orthogonal methods to constraint f_{NL} is the next logical step. Using the redshifted 21-cm to study the primordial non-Gaussianity is examined in depth with various techniques, [Chen, 2010, Chongchitnan, 2013, Crociani et al., 2009, D'Aloisio et al., 2013, Joudaki et al., 2011, Lewis, 2011, Lidz et al., 2013, Mao et al., 2013].

The presence of the primordial non-Gaussianity will manifest in the clustering of the galactic halos that eventually spawn ionizing stars. Thus, leading to the patchiness of the 21-cm signal that will differ with the one generated with a Gaussian inflationary potential. The volumetric data from the tomographic observations of the redshifted 21-cm signal will then contain the imprints of the primordial non-gaussianity. As the 21-cm experiments come online, testing the methodologies to determine the primordial non-Gaussianity presents itself as a very powerful application for SIM.

This work compares reionization histories of the simulated non-Gaussian and Gaussian

models and explores the significance of the observational signatures. The work uses two simulations generated with the same seed but different $f_{\rm NL}$ values, namely, $f_{\rm NL}$ = 0 and 50. The comoving volume of the simulations is 114 h^{-1} Mpc and ranges from $30.556 < z < 8.456$. The data was created earlier for different set of studies by Ilian Iliev in 2009.

We compare the two datasets using three methodologies, (i) comparing the power spectra, (ii) conducting the bias study, and finally (iii) estimating the bispectrum with observational effects. In the following sections, we discuss the results for the three different studies.

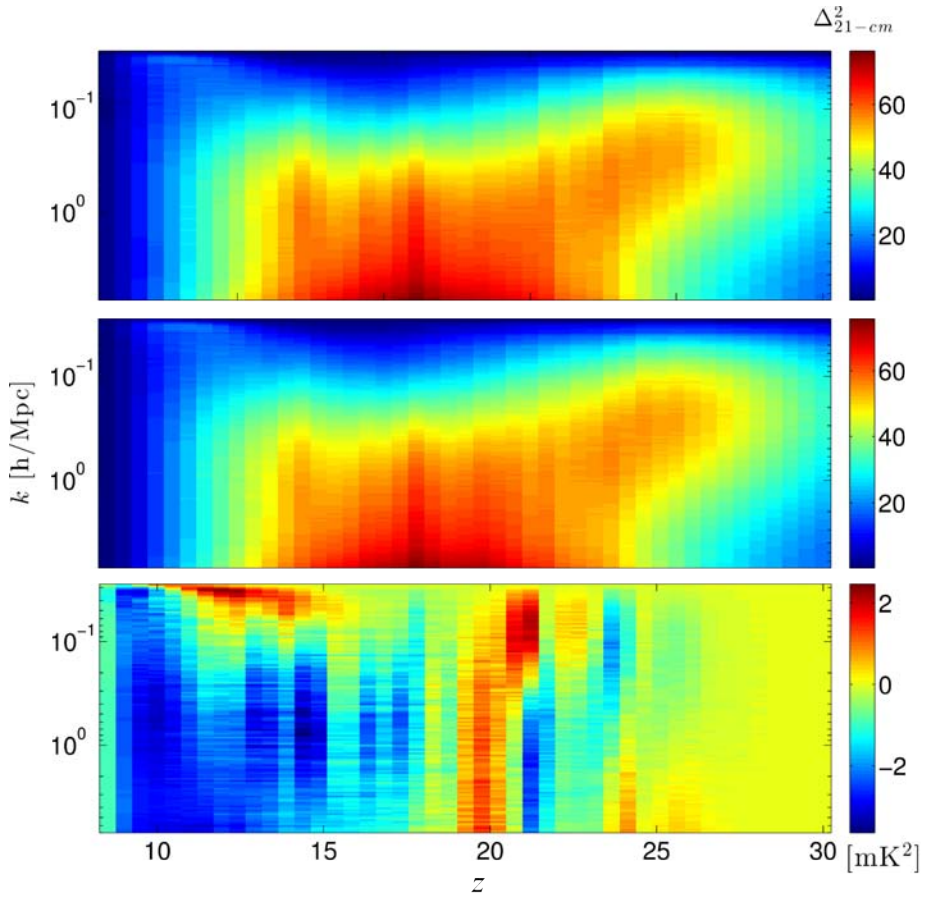

Figure 9.1: Power spectra ($\Delta^2_{\text{21-cm}}$) for $f_{\rm NL} = 0$ (top), $f_{\rm NL} = 50$ (middle), and the difference $f^{50}_{\rm NL} - f^{0}_{\rm NL}$ (bottom).

9.2 Power Spectra

The very first approach builds the 21-cm power spectra for the two separate datasets and gauges any differences. We use the MMRRM methodology of Mao et al. [2012] to generate the linear 21-cm power spectra. As discussed in the Appendix B, the MMRRM

code also performs the μ-decomposition of the power spectrum. This allows to compare the different moments of the power spectra representing disparate physical phenomenon across the entire ionization history.

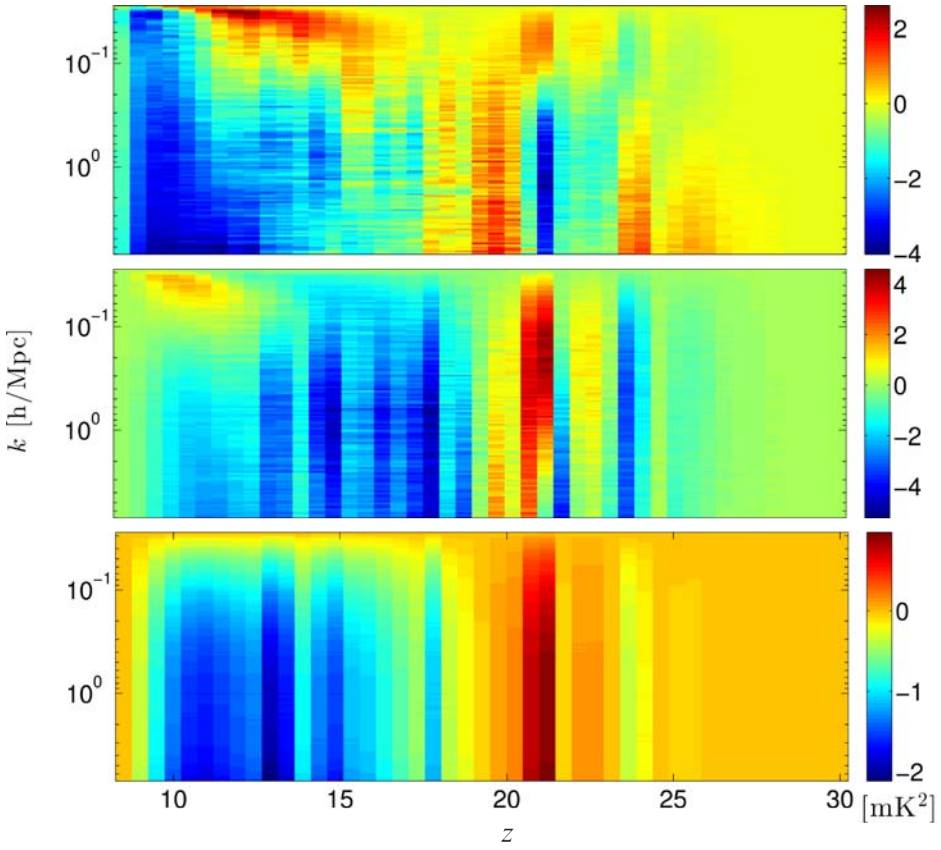

Figure 9.2: The difference $f_{\rm NL}^{50} - f_{\rm NL}^{0}$ of the μ-decomposed components of the power spectra, μ^0 (top), μ^2 (middle), and μ^4 (bottom).

We difference the two sets of complete spectral history, $f_{\rm NL} = 0, 50$, of the Gaussian and non-Gaussian cases in order to examine if the power spectrum captures any residual non-Gaussianity. If non-Gauussianity affects the clustering and thus the 21-cm signal, the residuals of the power spectrum should appear in the differences. The Figure 9.1 shows the power spectra from the Gaussian (top) and non-Gaussian (middle) case along with their difference (bottom). The first thing evident from the power spectra evolution of the Gaussian and non-Gaussian case is that they are very similar in cursory comparison. There's a lot of power in the small scale as the ionization starts, which fades away as the ionization reaches completion. As the ionization progresses, the power in the larger scales increases due to the merging of bubbles into larger volumes. By $\langle x_m \rangle = 40\%$ the individual power spectrum start to develop a 'knee' at small k values. This knee starts to peak and takes over the power from larger k-values as the ionization reaches towards

completion. The power in the small-scale bubbles plateaus and slowly goes down as the small bubble populations are subsumed into larger ionized regions. The difference-plot is mostly noisy with two hotspots. The elongated region from $z < 15$ in $k < 0.1$ is an interesting feature. Primarily because any non-Gaussian residual should appear in the large-scales of the simulation volume. The fact that this is at the edge may also mean that the box size used for this study may not be sufficient. To test if the feature is spurious we conducted two additional studies. In the first study we used another set of 114 h^{-1} Mpc simulation generated with a different seed with no non-Gaussianity. The difference in the spectra did not show any features at the lower k values. In the second study, as shown in the Figure 9.2, we differenced the μ-decomposed spectra. What is interesting to note is the feature of interest appears very strongly for μ^0 component but gradually fades for μ^2 and completely vanishes for μ^4. While these results are not conclusive they motivate the next two studies.

9.3 Bias Study

The second study is the bias study in collaboration with Anson D' Aloiso. The ionized density biases for four different redshifts, $z = 13.331, 9.611, 9.026,$ and 8.636 were estimated by HS from the simulated data and shared with Anson for calculating the $f_{\rm NL}$ using his power spectrum technique. Anson also wrote a brief note explaining the results which is transcribed below.

9.3.1 Definitions

The impact of primordial non-Gaussianity on the statistics of reionization has been explored by a number of authors [Chongchitnan, 2013, D'Aloisio et al., 2013, Joudaki et al., 2011, Lidz et al., 2013, Mao et al., 2013]. Unfortunately, each set of authors chose to quantify the scale-dependent effects on the ionization field with a different bias parameter. These bias parameters are all related, but care must be taken to avoid confusion and false comparisons. The ionized density bias calculated herein follows the definition from D'Aloisio et al. [2013].

9.3.2 Ionized Density Bias

Let $\rho_{\rm HII}(\mathbf{r}, z)$ denote the mass density of ionized hydrogen (what we will call the ionized density), and let us define the ionized density contrast as,

$$\delta_{\rho_{\rm HII}}(\mathbf{r}, z) = \frac{\rho_{\rm HII}(\mathbf{r}, z)}{\bar{\rho}_{\rm HII}(z)} - 1 \tag{9.1}$$

where, $\bar{\rho}_{\rm HII}(z)$ is the mean ionized density at redshift z. The ionized density bias is defined as,

$$b_{\rho{\rm HII}}(k, z) \equiv \frac{\widetilde{\delta}_{\rho{\rm HII}}(k, z)}{\widetilde{\delta}(k, z)} \tag{9.2}$$

where, $\widetilde{\delta}_{\rho{\rm HII}}$ and $\widetilde{\delta}(k, z)$ are the Fourier transforms of the matter and ionized density contrasts respectively.

The results are expressed in ionized density bias for two primary reasons, (i) It is the most natural quantity to calculate within the linear perturbation theory of reionization (LPTR - see [D'Aloisio et al., 2013, Zhang et al., 2007]) and (ii) The calculation of the ionized density bias within the analytical excursion-set model of reionization (ESMR) yields an expression which has almost exactly the same form as the well-known non-Gaussian halo bias. It thus seemed to be the most natural quantity in our formalism.

In D'Aloisio et al. [2013], the ESMR is used to show that the non-Gaussian ionized density bias is,

$$b^{\rm NG}_{\rho{\rm HII}} = b^{\rm G}_{\rho{\rm HII}} + \Delta b^{(i)}_{\rho{\rm HII}} + \Delta b^{(d)}_{\rho{\rm HII}} \tag{9.3}$$

where, $b^{\rm G}_{\rho{\rm HII}}$ is the Gaussian bias (*i.e.*, in a model with the same source efficiency parameters), and$\Delta\ b^{(i)}_{\rho{\rm HII}}$ and$\Delta\ b^{(d)}_{\rho{\rm HII}}$ are the scale-independent and -dependent corrections due non-Gaussianity respectively (see §2.3.2 of D'Aloisio et al. [2013]). The scale-dependent correction is of particular interest here, and has the form,

$$\Delta b^{(d)}_{\rho{\rm HII}} = 2\delta_c\ (b^{\rm G}_{\rho{\rm HII}} - 1)\ \frac{\mathcal{F}^{(3)}_{min}(k)}{\mathcal{M}_{min}(k)} \tag{9.4}$$

where, the the ratio $\mathcal{F}^{(3)}_{min}(k)/\mathcal{M}_{min}(k)$ is the form factor that encapsulates the scale-dependence, please see equation (17), (33), and (34) of D'Aloisio et al. [2013]. In the

small k limit of the so-called "local model" of non-Gaussianity, the Equation 9.4 reduces to$\Delta\ b^{(d)}_{\rho\mathrm{HII}} \propto (b^{\mathrm{G}}_{\rho\mathrm{HII}} - 1)/k^2$, *i.e.*, the ionized density bias scales as k^{-2}, like the well-known halo bias result. Note that the Equation 9.3 was tested against the LPTR for a number of different reionization models. It was found that it provides a reasonably accurate mapping between $b^{\mathrm{G}}_{\rho\mathrm{HII}}$ and $b^{\mathrm{NG}}_{\rho\mathrm{HII}}$. (see §4.4 of D'Aloisio et al. [2013]).

The Ionized Fraction Bias

Another way to quantify the impact of primordial non-Gaussianity on the large- scale structure of reionization is the ionized fraction bias. Let $x_i(\mathbf{r}, z)$ denote the ionized fraction, and let $\delta_x(\mathbf{r}, z)$ denote the ionized fraction contrast,

$$\delta_x(\mathbf{r}, z) = \frac{x_i(\mathbf{r}, z)}{\bar{x}_i(z)} - 1 \tag{9.5}$$

where, $\bar{x}_i(z)$ is the spatially averaged ionized fraction at redshift z. The ionized fraction bias is defined as,

$$b_x(k, z) = \frac{\widetilde{\delta}_x(k, z)}{\widetilde{\delta}(k, z)} \tag{9.6}$$

The bias b_x is related to $b_{\rho\mathrm{HII}}$ on large scales by, (see §2.1 D'Aloisio et al. [2013])

$$b_x(k, z) = b_{\rho\mathrm{HII}}(k, z) - 1 \tag{9.7}$$

Thus the scale-dependent non-Gaussian correction to the ionized fraction bias is,

$$\Delta b^{(d)}_x(k) = 2\delta_c\ b^{\mathrm{G}}_x\ \frac{\mathcal{F}^{(3)}_{min}(k)}{\mathcal{M}_{min}(k)} \tag{9.8}$$

This is the equation that will be tested in the following exercise, especially as the ionized fraction bias is easier to calculate from the simulation data compared to the density bias. The ionized fraction bias was estimated [by HS] as,

$$b_x(k) = \frac{P_{\delta_x\delta}(k)}{P_{\delta\delta}(k)} \tag{9.9}$$

where, $P_{\delta_x\delta}(k)$ is the cross-spectrum of δ_x and δ (where δ is the matter density contrast), and $P_{\delta\delta}(k)$ is the standard matter power spectrum.

9.3.3 Comparison Methodology

In what follows, will consider the difference between the non-Gaussian and Gaussian ionized fraction biases,

$$b_x^{\rm NG} - b_x^{\rm G} = \Delta b_x^{(i)} + \Delta b_x^{(d)}(k) \tag{9.10}$$

where, the simulations have fixed source efficiency parameters (i.e. the only thing different between the reionization models is the non-Gaussianity). We will compare $b_x^{\rm NG} - b_x^{\rm G}$ observed in the C^2-Ray simulations to the "predicted" $b_x^{\rm NG} - b_x^{\rm G}$ from the analytical results. To obtain the latter, the Gaussian ionized fraction bias from the simulation [provided by HS] are plugged in the Equation 9.8 to produce the predicted$\Delta\ b_x^{(d)}(k)$. The analytical results from ESMR are used to generate the$\Delta\ b_x^{(i)}$.

9.3.4 Caveats

There are several issues to bear in mind when viewing the results of the comparison below:

1. *Effects of self-regulation*: The C^2-Ray simulations model the effects of "self-regulation" on reionization, *i.e.*, sources below a halo mass threshold of 10^9 M$_\odot$ are suppressed if they reside within an H II region. The analytical model considered here does not account for such feedback effects, so the validity of the Equation 9.8 in this context is not clear. Thus the comparison is not "apples to apples", so to speak. As discussed below, the comparison might help shed light on the impact of self-regulation, but it would be nice to first establish (or not) the analytical results by comparing against a simulation with a more similar reionization model.

2. *The simulation box size I*: The simulation box size is L = 114 h^{-1} Mpc on a side, which allows to probe down to k values of $(2\pi)/(114/0.7)$ h^{-1} Mpc = 0.08 Mpc^{-1}. The scale-dependent effect of primordial non-Gaussianity on b_x is truly a large-scale effect ($k < 0.01$ Mpc^{-1}). The effect is really quite small for $k > 0.01$ Mpc^{-1} (see Fig. 6 of D'Aloisio et al. [2013]), so the simulation box size is not ideal for this comparison.

3. *The simulation box size II*: The local model of non-Gaussianity couples large- and small-scale modes in the initial density fluctuations. With a box size as small as L = 114 h^{-1} Mpc , I worry if we could be missing important large-scale modes (with

wavelengths longer than the box) that would otherwise be coupled to the smaller-scale modes in our box. If so, I wonder what this does to the accuracy of the halo bias.

4. *Box size and regime of validity of the analytical calculations*: The analytical results in D'Aloisio et al. [2013] were derived in the large-scale limit ($k \ll 1$), a regime in which the Gaussian halo bias is scale-independent. Additionally, our results apply to scales much larger than the mean free path of UV photons through the IGM. These conditions may not be met over the k-range in the simulations, especially near the end of reionization.

9.3.5 Results

Comment on the mean ionized fractions in the simulations

Before presenting the comparison, I would like to comment on something curious about the mean ionized fractions in the C^2-Ray simulations. Table 1 compares the mass- and volume-weighted mean ionized fractions in the Gaussian and non-Gaussian ($f_{\rm NL} = 50$) C^2-Ray simulations (these numbers were provided by HS). In D'Aloisio et al. [2013], we showed that $f_{\rm NL} = 50$ (or more generally positive $f_{\rm NL}$) makes reionization end slightly earlier than the corresponding Gaussian case, and that the non-Gaussian reionization history deviates most from the Gaussian case at the earliest times (see Fig. 2 of that paper; note that Crociani et al. [2009] reached a similar conclusion). This has a simple explanation. Reionization sources (halos above M$\sim 10^8$ M$^\odot$) become more and more rare with increasing redshift. Since the effects of non-Gaussianity are most evident in the abundance and bias of the rarest objects, it follows that the effects of non-Gaussianity on the reionization history is most evident at high redshifts. I am therefore surprised to see such little difference in the ionized fractions at $z = 13.221$, relative to the lower redshifts in Table 1. In fact, the % difference in x_i appears to grow with decreasing redshift, except near the end of reionization ($\langle x_i \rangle \sim 0.9$). It is also important to note that the mean ionized fractions at $z = 13.221$ for $f_{\rm NL} = 50$ are lower than their Gaussian counterparts at the same redshift. This defies my expectation, since the reionization sources are more abundant in models with $f_{\rm NL} = 50$ compared to the Gaussian case.

Putting the peculiarity of the $z = 13.221$ numbers aside, perhaps the trend of increasing |%

difference| from $z = 9.611$ to $z = 9.026$ is a result of self-regulation? Suppose reionization starts with halos above 10^8 $M^{\odot}$, but self-regulation shuts down many of those halos, so halos with mass $> 10^9$ $M^{\odot}$ dominate more and more as reionization proceeds. Halos with mass $> 10^9$ $M^{\odot}$ are rarer than halos with mass $\sim 10^8$ $M^{\odot}$, so the statistics of the former are more impacted by non-Gaussianity compared to the latter. I could imagine that this interplay between the $\sim 10^8$ $M^{\odot}$ and the $\sim 10^9$ $M^{\odot}$ halos could explain the discrepancy with my expectations (for which I am relying on a simpler model of reionization).

	Mass-weighted Mean ionized Fraction		
Redshift	Gaussian	$f_{\rm NL} = 50$	% Difference
13.221	0.1063	0.1055	-0.8
9.611	0.4832	0.5013	3.7
9.026	0.6922	0.7265	5.0
8.636	0.9186	0.9517	3.6
	Volume-weighted Mean ionized Fraction		
13.221	0.0759	0.0746	-1.8
9.611	0.4109	0.4275	4.0
9.026	0.6262	0.6654	6.3
8.636	0.8945	0.9372	4.8

Table 9.1: Comparison of global ionized fractions in the Gaussian and non-Gaussian C^2-Ray simulations.

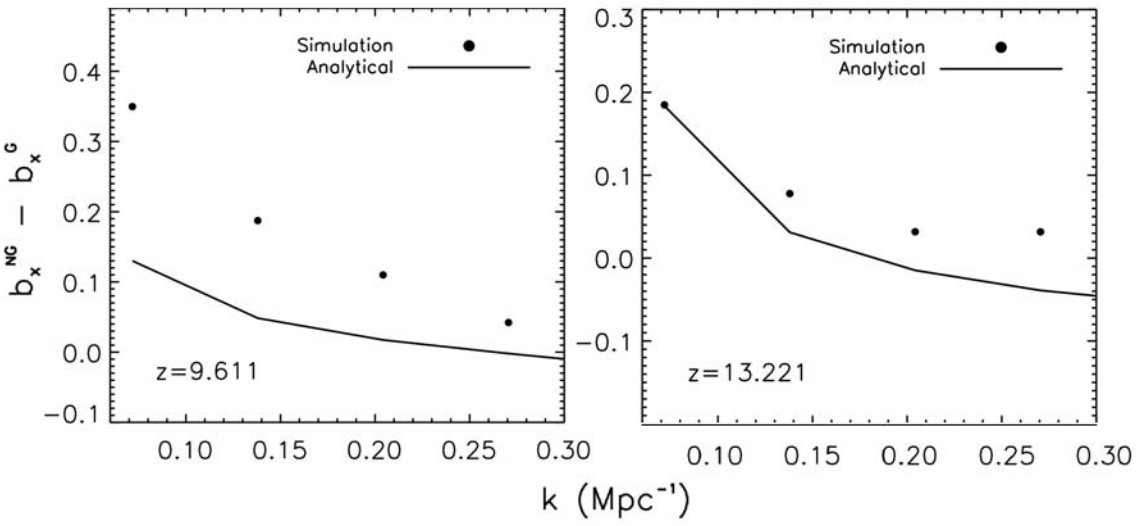

Figure 9.3: Comparison of the predicted ionized fraction bias (from a simple analytical model of reionization) to that observed in the C^2-Ray simulation. See text for more details.

The Ionized Fraction Bias

The Figure 9.3 compares $b_x^{\rm NG} - b_x^{\rm G}$ from the C^2-Ray simulations to the theoretical predictions, as described in the methodology section above. I show results from redshifts $z = 13.221$ and $z = 9.611$ because, at these redshifts, $b_x^{\rm G}(k)$ plateaus to a roughly constant value as k gets smaller. At $z = 9.026$ and 8.636, $b_x^{\rm G}(k)$ never plateaus before reaching the smallest k, *i.e.*, $b_x^{\rm G}(k)$ is scale-dependent on the largest scales probed by our simulation box. This is a regime in which we should not apply our analytical results. Note that I also show the bias up to a maximum k of 0.3 Mpc^{-1}, since our analytical results only apply in the limit of small k (see §9.3.4 above).

9.4 Measuring the Bispectrum

In the third and the final study, we estimate the bispectrum of the datasets using the estimation methodology of Regan [2011]. This ongoing study is conducted in close collaboration with Donough Regan under the guidance of Andrew Liddle and Ilian Iliev. The motivation of this study is to estimate the shape of the bispectrum and the error in the amplitude,$\Delta\ f_{\rm NL}$, from the Gaussian and non-Gaussian datasets. Thereafter, the datasets are convolved with the telescope beams corresponding to their observational frequencies and determine the same parameters. We use SIM to extract beams for observational frequencies corresponding to $z = 13.221, 9.661, 9.026,$ and 8.636 for the SL10 configuration. The frequencies are, $\nu_{\rm obs} \sim 100, 135, 140,$ and 150 MHz. One obvious drawback with lower frequencies is that the beams are large and therefore tend to average out the underlying features. Thus warranting that deconvolution is able to extract features relevant for the estimation of the non-Gaussian bispectrum. The data cubes for the four redshifts are converted to Jy and convolved with the extracted beams.

The Figure 9.4 shows the power spectra of the four data cubes for the pristine ioniaed fraction and post convolution data. It is evident from the power spectrum, that the formation of the structure increases the power at large scales. However, convolution with the synthesized beam redistributes the power and makes some of the signals indistinguishable. For example, the large-scale structures at redshifts $z = 9.611$ and 9.026 have almost an order of magnitude difference in power. This difference is diminished post observation.

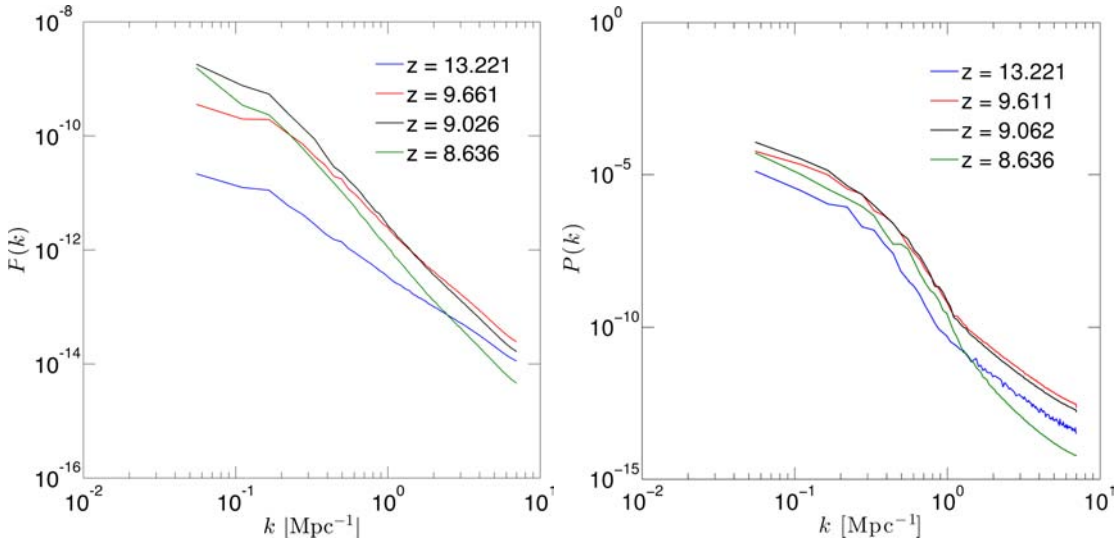

Figure 9.4: The power spectra for the ionized fraction in Jy (left) and simulated data observed with SL10 configuration, Jy/Beam (right).

Next, we generate the bispectrum for both the data cubes and plot them in the tetrapyd form [Fergusson et al., 2010]. Recall, that the dirac delta term in the bispectrum equation 2.33 impose triangle constraints on the wave-vectors $\mathbf{k_1}, \mathbf{k_2}$, and $\mathbf{k_3}$. The tetrahedral volume over a triangular pyramid provides a domain for the the wave-vectors in the Fourier domain. This domain is called the *tetrapyd* and shown in the Figure 9.5. See [Fergusson et al., 2010, Schmittfull et al., 2013].

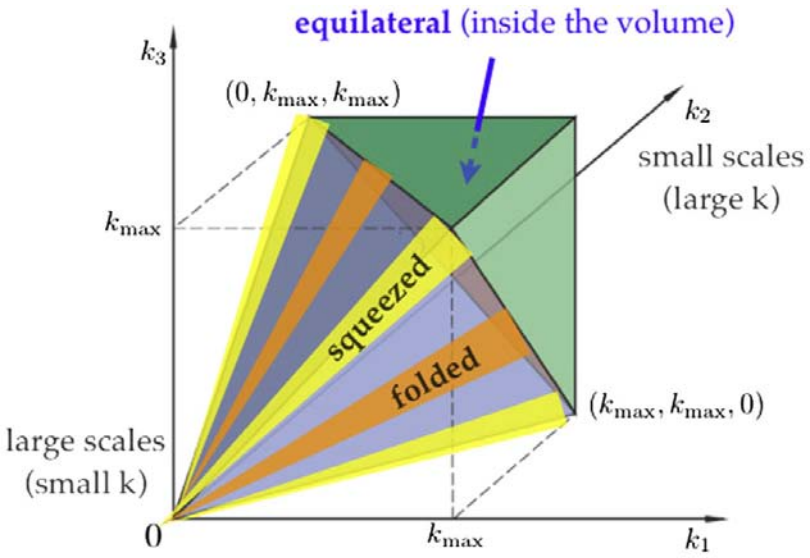

Figure 9.5: *Space of triangles with sides k_1, k_2, k_3, i.e., each point inside the tetrapyd volume corresponds to a triangle configuration. Squeezed, folded and equilateral configurations are highlighted.* The figure and caption are from, Schmittfull et al. [2013].

The distribution of the spectrum on this domain allows for separation of nonlinear

processes responsible for the bispectrum. For example, primordial non-Gaussianity appears separately from the nonlinear processes due to gravitational collapse or ionization. The bispectrum will contain all these processes in the form of different triangles (equilateral, squeezed, and folded). The underlying physical processes have different dependence on the wave numbers, k_1, k_2, and k_3, thus resulting in different shapes of the bispectra, see Figure 2.2. As shown in the Figure 9.5, the squeezed triangle, where one wave number is much smaller than the other two, represents multiple field inflationary models. This shape is also known as local shape. The volume of the tetrapyd is $k^3_{\text{max}}/2$.

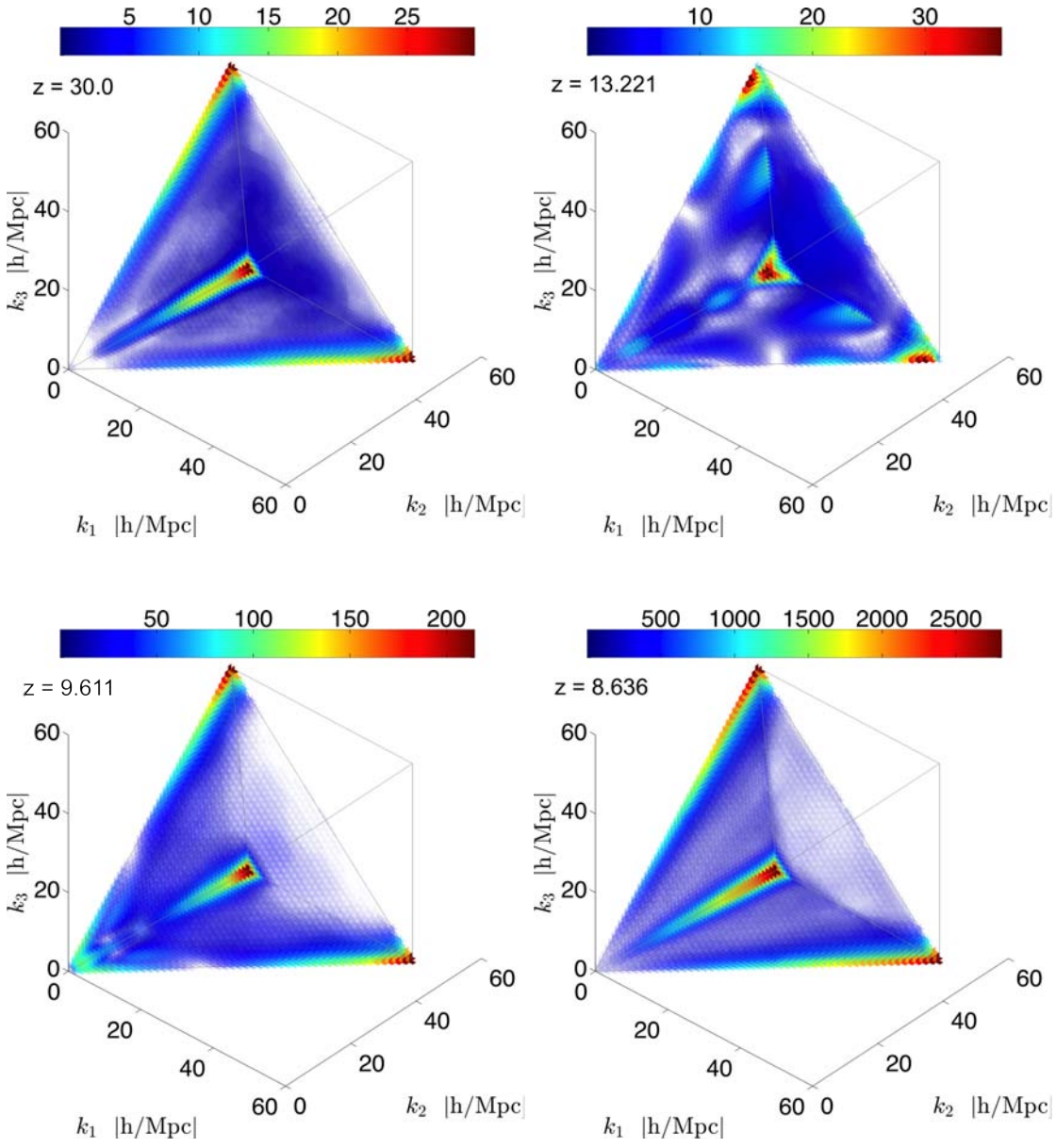

Figure 9.6: The bispectrum for the ionized fraction. The input data of the ionized fraction is in Jy, however, the bispectrum is in arbitrary units relative units. The color bar represents the relative strength of the modes.

The Figure 9.6 shows the tetrpyds of the ionization data from four redshift ranges, namely, $z = 30.0, 13.221, 9.611,$ and 8.636. The triangles are represented on the axes resolution of $50k/k_{\max}$. 50 polynomials are used to define the bispectrum shapes.

With no ionizing sources to initiate the ionization process, at $z = 30.0$, (top, left) of Figure 9.6, the bispectrum captures the nonlinearity of the gravitational collapse along with the primordial non-Gaussianity. The local shape of the bispectrum is very distinct in the figure. The power in the squeezed triangle limit is concentrated at small scales. As the ionization begins, $< x_m >= 7\%$ at $z = 13.221$, the power in the bispecrum is dispersed across the tetrapyd. The local shape is no longer discernible. It is worth noting that as the ionization reach 93% at $z = 8.636$, the original bispectrum starts to reappear. One explanation of this is that the primordial non-Gaussianity gets buried under the more dominant nonlinearities due to the patchy ionization and towards the completion of the ionization, the non-Gaussianity is visible again. Note that this exercise is performed on the pristine data.

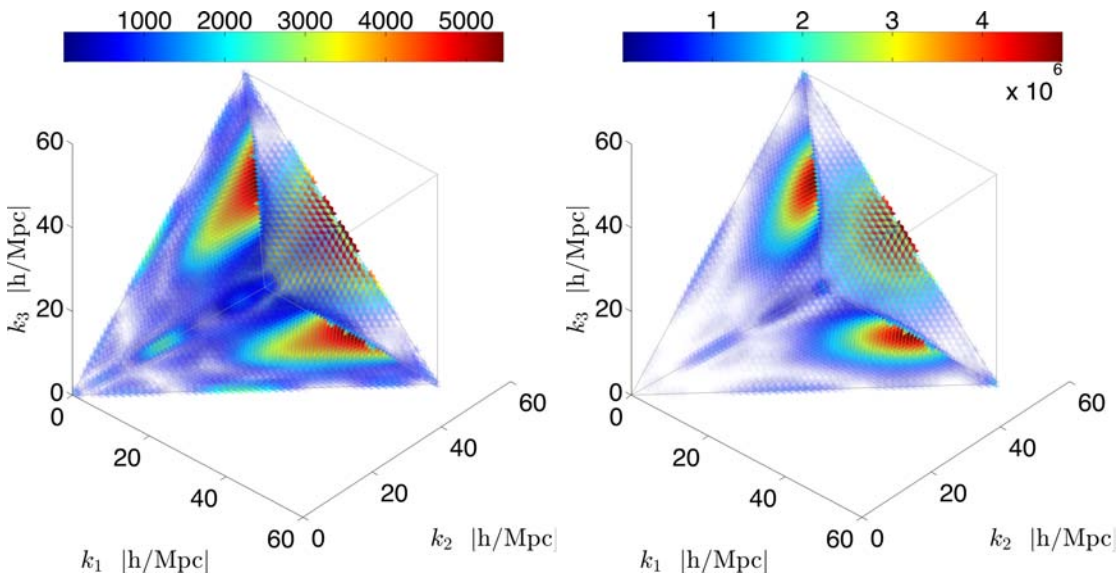

Figure 9.7: The bispectrum spectrum of the observed ionized fraction. The input data of the ionized fraction is in Jy/Beam, however, the bispectrum is in arbitrary units relative units. The color bar represents the relative strength of the modes.

The Figure 9.7 shows two extreme ends of the dataset of the ionization history. It is immediately evident that the beam convolution wipes out any semblance of the bispectrum, and redistributes the power across the domain. This is just the beam convolution. We have not yet considered the entire series of propagation effects that

will corrupt the ionization data. This opens up a testbed for exploring techniques that will be well suited to best extract the non-Gaussianity that readily appears in the pristine data. These results motivate the next round of studies where we will clean the observed data and qualify errors on the signal.

Caveats

The generation of the bispectrum also yields the$\Delta\ f_{\rm NL}$. We list the values in Table 9.2. The values are not reliable. While the shape of the bispectrum is captured by the code, the amplitude is suspect and requires additional investigation. This is primarily due to the normalization factor in the bispectrum. The difference of the values between the pristine and the observed is also due to the difference of units, Jy and Jy/Beam respectively. For this reason, the color bar numbers are also not reliable. As the next steps we plan to resolve the normalization factor and repeat the exercise. We also plan to use 3-point correlation codes to directly estimate the bispectrum and compare are the results. Thereafter, we will explore the technique(s) that will optimally extract the primordial non-Gaussian shape from the observed dataset and explore real world challenges.

z	$\Delta f_{\rm NL}$	
	ionized frac	observed
13.221	1.528×10^{2}	1.535
9.611	4.303×10^{1}	3.107×10^{-2}
9.026	2.179×10^{1}	1.467×10^{-1}
8.636	2.954	1.986×10^{-3}

Table 9.2:$\Delta\ f_{\rm NL}$ estimated for ionized fraction and observed with SKA-class telescope.

Part IV

Epilogue

This work sought to consolidate wide range of the state-of-the-art tools to build a framework for conducting in depth observational studies for the upcoming EoR and Dark Ages experiments with the redshifted 21-cm. Using the Lyman-limit system models based on observational data, we explored the effects of the LLS absorbers on the ionization history. We examined the morphological evolution of the H II regions and determined that the presence of LLS delays the end of ionization ($\langle x_m \rangle$ 99%) by$\Delta\ z \sim 0.8$. We build the SIM framework incorporating CubeP^{3}M, C^{2}Ray, and MeqTrees connected with the SIM Middleware. This allowed for conducting preliminary trade-off studies with SKA core size variations and extragalactic foreground calibration and removal. We also explored the possibility of constraining the amplitude parameter for the primordial non-Gaussianity by using the tomographic redshifted 21-cm data.

By developing solutions, the research has established the need for tools and simulations that can explore and provide solutions for a wide range of observational challenges. There is a clear need for standardization in the software development within the wide astronomy/physics communities. To successfully address the massive data problem will require harnessing the emerging parallel compute architectures and programming models. This in turn will require the adoption of advanced software engineering practices. Throw away codes in non-HPC compliant languages developed at student level will have to be replaced by professional, tested, public domain, advanced solutions.

Many radio telescope arrays today do not have a software equivalent of SIM. Most of the trade-off studies are left for specialized domain experts or third party scientists. In the literature, there are many Fisher Matrix, image plane, and limited sampling function studies that attempt to address variety of observational issues. The tools like SIM provide the exploration of the parametric phase-space critical for discovering optimal roadmap for strategic mission planning. SIM also defines the figure of merit as a standard for

comparison of disparate experiments.

With SIM, we now plan to conduct more in-depth studies for the observational and science goals afforded by the redshifted 21-cm. We also wish to provide datasets to the wider community to conduct its own tests in extracting the underlying signal, thus opening the phase-space to the wider community of experts. This research was deeply rewarding and illuminating. I hope it adds to the foundation of more advanced efforts to come in the future.

Bibliography

Atacama Large Millimeter/Sub-millimeter Array

(http://www.almaobservatory.org/). 75

Australian Square Kilometre Array Pathfinder

(http://www.atnf.csiro.au/projects/askap/). 75

Low Frequency Array

(http://www.lofar.org/). 75

Square Kilometre Array.

(http://www.skatelescope.org/). 75

Expanded Very Large Array

(http://www.nrao.edu/index.php/about/facilities/vlaevla). 75

A. Lewis. Early Universe. 2012. URL `http://cosmologist.info/teaching/EU/notes_inflation.pdf`. 25

F. B. Abdalla. Towards third-generation calibration in radio astronomy. *MCCT SKADS Mixed Workshop:*, 2009. 91

T. Abel and B. D. Wandelt. Adaptive ray tracing for radiative transfer around point sources. *MNRAS*, 330:L53–L56, March 2002. doi: 10.1046/j.1365-8711.2002.05206.x. 72

T. Abel, M. L. Norman, and P. Madau. Photon-conserving Radiative Transfer around Point Sources in Multidimensional Numerical Cosmology. *ApJ*, 523:66–71, September 1999. doi: 10.1086/307739. 65

P. A. R. Ade, N. Aghanim, Z. Ahmed, R. W. Aikin, K. D. Alexander, M. Arnaud, J. Aumont, C. Baccigalupi, A. J. Banday, D. Barkats, and et al. Joint Analysis of BICEP 2 /K e c k A r r a y and Planck Data. *Physical Review Letters*, 114(10):101301, March 2015. doi: 10.1103/PhysRevLett.114.101301. 7, 19

A. Albrecht and P. J. Steinhardt. Cosmology for grand unified theories with radiatively induced symmetry breaking. *Physical Review Letters*, 48:1220–1223, April 1982. doi: 10.1103/PhysRevLett.48.1220. 24

M. A. Alvarez and T. Abel. The Effect of Absorption Systems on Cosmic Reionization. *ApJ*, 747:126, March 2012. doi: 10.1088/0004-637X/747/2/126. 48, 67

R. Athreya. A New Approach to Mitigation of Radio Frequency Interference in Interferometric Data. *ApJ*, 696:885–890, May 2009. doi: 10.1088/0004-637X/696/1/885. 11

W. A. Baan, P. A. Fridman, and R. P. Millenaar. Radio Frequency Interference Mitigation at the Westerbork Synthesis Radio Telescope: Algorithms, Test Observations, and System Implementation. *AJ*, 128:933–949, August 2004. doi: 10.1086/422350. 11

R. Barkana and A. Loeb. A Method for Separating the Physics from the Astrophysics of High-Redshift 21 Centimeter Fluctuations. *APJ Letters*, 624:L65–L68, May 2005. doi: 10.1086/430599. 173, 174

R. H. Becker, X. Fan, R. L. White, M. A. Strauss, V. K. Narayanan, R. H. Lupton, J. E. Gunn, J. Annis, N. A. Bahcall, J. Brinkmann, A. J. Connolly, I. Csabai, P. C. Czarapata, M. Doi, T. M. Heckman, G. S. Hennessy, Ž. Ivezić, G. R. Knapp, D. Q. Lamb, T. A. McKay, J. A. Munn, T. Nash, R. Nichol, J. R. Pier, G. T. Richards, D. P. Schneider, C. Stoughton, A. S. Szalay, A. R. Thakar, and D. G. York. Evidence for Reionization at z˜6: Detection of a Gunn-Peterson Trough in a z=6.28 Quasar. *AJ*, 122:2850–2857, December 2001. doi: 10.1086/324231. 44

N. D. R. Bhat, J. M. Cordes, S. Chatterjee, and T. J. W. Lazio. Radio frequency interference identification and mitigation using simultaneous dual-station observations. *Radio Science*, 40:RS5S14, June 2005. doi: 10.1029/2004RS003172. 11

BICEP2 Collaboration, P. A. R Ade, R. W. Aikin, D. Barkats, S. J. Benton, C. A. Bischoff, J. J. Bock, J. A. Brevik, I. Buder, E. Bullock, C. D. Dowell, L. Duband, J. P. Filippini, S. Fliescher, S. R. Golwala, M. Halpern, M. Hasselfield, S. R. Hildebrandt, G. C. Hilton, V. V. Hristov, K. D. Irwin, K. S. Karkare, J. P. Kaufman, B. G. Keating, S. A. Kernasovskiy, J. M. Kovac, C. L. Kuo, E. M. Leitch, M. Lueker, P. Mason, C. B. Netterfield, H. T. Nguyen, R. O'Brient, R. W. Ogburn, IV, A. Orlando, C. Pryke, C. D. Reintsema, S. Richter, R. Schwarz, C. D. Sheehy, Z. K. Staniszewski, R. V. Sudiwala, G. P. Teply, J. E. Tolan, A. D. Turner, A. G. Vieregg, C. L. Wong, and K. W. Yoon. BICEP2 I: Detection Of B-mode Polarization at Degree Angular Scales. *ArXiv e-prints*, March 2014. 7, 19

J. S. Bolton and M. G. Haehnelt. The observed ionization rate of the intergalactic medium and the ionizing emissivity at z $\geq$ 5: Evidence for a photon-starved and extended epoch of reionization. *MNRAS*, 382:325–341, November 2007. doi: 10.1111/j.1365-2966.2007.12372.x. 45

J. S. Bolton, G. D. Becker, J. S. B. Wyithe, M. G. Haehnelt, and W. L. W. Sargent. A first direct measurement of the intergalactic medium temperature around a quasar at z = 6. *MNRAS*, 406:612–625, July 2010. doi: 10.1111/j.1365-2966.2010.16701.x. 45

J. R. Bond and G. Efstathiou. Cosmic background radiation anisotropies in universes dominated by nonbaryonic dark matter. *APJ Letters*, 285:L45–L48, October 1984. doi: 10.1086/184362. 45

M. Born and E. Wolf. *Principles of Optics*. Cambridge University Press, October 1999. 52, 53

R. J. Bouwens, G. D. Illingworth, I. Labbe, P. A. Oesch, M. Trenti, C. M. Carollo, P. G. van Dokkum, M. Franx, M. Stiavelli, V. González, D. Magee, and L. Bradley. A candidate redshift z˜10 galaxy and rapid changes in that population at an age of 500Myr. *Nature*, 469:504–507, January 2011. doi: 10.1038/nature09717. 20, 46

R. Braun. SKA1 Level 0 Science Requirements. *SKA - TEL.SCI - SKO - SRQ - 001*, February 2014. 87, 124, 125

Roberta Brawer. Inflationary cosmology and the horizon and flatness problems. *MIT*, 1995. 24

E. Chapman, F. B. Abdalla, G. Harker, V. Jelić, P. Labropoulos, S. Zaroubi, M. A. Brentjens, A. G. de Bruyn, and L. V. E. Koopmans. Foreground removal using FASTICA: a showcase of LOFAR-EoR. *MNRAS*, 423:2518–2532, July 2012. doi: 10.1111/j.1365-2966.2012.21065.x. 11, 81

E. Chapman, F. B. Abdalla, J. Bobin, J.-L. Starck, G. Harker, V. Jelić, P. Labropoulos, S. Zaroubi, M. A. Brentjens, A. G. de Bruyn, and L. V. E. Koopmans. The scale of the problem: recovering images of reionization with Generalized Morphological Component Analysis. *MNRAS*, 429:165–176, February 2013. doi: 10.1093/mnras/sts333. 81

E. Chapman, S. Zaroubi, and F. Abdalla. Foreground Removal vs. Foreground Avoidance: Contamination of the EoR Window. *ArXiv e-prints*, August 2014. 81

X. Chen. Primordial Non-Gaussianities from Inflation Models. *Advances in Astronomy*, 2010:638979, 2010. doi: 10.1155/2010/638979. 136

S. Chongchitnan. The 21cm power spectrum and the shapes of non-Gaussianity. *Journal of Cosmology and Astroparticle Physics*, 3:037, March 2013. doi: 10.1088/1475-7516/2013/03/037. 136, 139

T. L. Chow. *Gravity, Black Holes, and the Very Early Universe*. Springer Science+Business Media, 2008. 20

B. Ciardi. Cosmic reionization: theoretical modelling and forthcoming observations. In *IAU Joint Discussion*, volume 12 of *IAU Joint Discussion*, August 2006. 47

A. S. Cohen and H. J. A. Röttgering. Probing Fine-Scale Ionospheric Structure with the Very Large Array Radio Telescope. *AJ*, 138:439–447, August 2009. doi: 10.1088/0004-6256/138/2/439. 11

T. J. Cornwell, M. A. Holdaway, and J. M. Uson. Radio-interferometric imaging of very large objects: implications for array design. *AAP*, 271:697, April 1993. 88

M. Crocce, S. Pueblas, and R. Scoccimarro. Transients from initial conditions in

cosmological simulations. *Mon.Not.Roy.Astron.Soc.*, 373:369–381, 2006. URL http://arxiv.org/abs/astro-ph/0606505. 63

D. Crociani, L. Moscardini, M. Viel, and S. Matarrese. The effects of primordial non-Gaussianity on the cosmological reionization. *MNRAS*, 394:133–141, March 2009. doi: 10.1111/j.1365-2966.2008.14325.x. 136, 143

A. D'Aloisio, J. Zhang, P. R. Shapiro, and Y. Mao. The scale-dependent signature of primordial non-Gaussianity in the large-scale structure of cosmic reionization. *MNRAS*, 433:2900–2919, August 2013. doi: 10.1093/mnras/stt926. 136, 139, 140, 141, 142, 143

J. R. Fergusson, M. Liguori, and E. P. S. Shellard. General cmb and primordial bispectrum estimation: Mode expansion, map making, and measures of $F_{\rm nl}$. *Phys. Rev. D*, 82: 023502, Jul 2010. doi: 10.1103/PhysRevD.82.023502. URL http://link.aps.org/doi/10.1103/PhysRevD.82.023502. 146

G. B. Field. Excitation of the Hydrogen 21-CM Line. *Proceedings of the IRE*, 46:240–250, January 1958. doi: 10.1109/JRPROC.1958.286741. 42

G. B. Field. The Spin Temperature of Intergalactic Neutral Hydrogen. *ApJ*, 129:536, May 1959. doi: 10.1086/146653. 40, 80, 106

K. Finlator, S. P. Oh, F. Özel, and R. Davé. Gas clumping in self-consistent reionization models. *Mon.Not.Roy.Astron.Soc.*, 427:2464–2479, December 2012. doi: 10.1111/j.1365-2966.2012.22114.x. 47

P. A. Fridman. Statistically Stable Estimates of Variance in Radio-Astronomy Observations as Tools for Radio-Frequency Interference Mitigation. *AJ*, 135:1810–1824, May 2008. doi: 10.1088/0004-6256/135/5/1810. 11

M. M. Friedrich, G. Mellema, M. A. Alvarez, P. R. Shapiro, and I. T. Iliev. Topology and sizes of H II regions during cosmic reionization. *MNRAS*, 413:1353–1372, May 2011. doi: 10.1111/j.1365-2966.2011.18219.x. 98

Steven Furlanetto, S. Peng Oh, and Frank Briggs. Cosmology at low frequencies: The 21 cm transition and the high-redshift universe. *Phys.Rept.*, 433:181–301, 2006. URL http://arxiv.org/abs/astro-ph/0608032. 5, 42, 43, 48

G. W. Gibbons and N. Turok. Measure problem in cosmology. *Physical Review D*, 77(6): 063516, March 2008. doi: 10.1103/PhysRevD.77.063516. 29

J. W. Goodman. *Statistical Optics*. Weiley Series - Pure and applied optics, 1985. 53

J. W. Goodman. *Introduction to Fourier optics*. Roberts and Company Publishers, 2005. 52

J. E. Gunn and B. A. Peterson. On the Density of Neutral Hydrogen in Intergalactic Space. *ApJ*, 142:1633–1641, November 1965. doi: 10.1086/148444. 44

A. H. Guth. Inflationary universe: A possible solution to the horizon and flatness problems. *Physical Review D*, 23:347–356, January 1981. doi: 10.1103/PhysRevD.23.347. 19, 25

J. P. Hamaker. Understanding radio polarimetry. IV. The full-coherency analogue of scalar self-calibration: Self-alignment, dynamic range and polarimetric fidelity. *Astronomy & Astrophysics Supplement*, 143:515–534, May 2000. doi: 10.1051/aas:2000337. 51

J. P. Hamaker and J. D. Bregman. Understanding radio polarimetry. III. Interpreting the IAU/IEEE definitions of the Stokes parameters. *Astronomy & Astrophysics Supplement*, 117:161–165, May 1996. 51

J. P. Hamaker, J. D. Bregman, and R. J. Sault. Understanding radio polarimetry. I. Mathematical foundations. *Astronomy & Astrophysics Supplement*, 117:137–147, May 1996. 51, 58, 60

G. Harker, S. Zaroubi, G. Bernardi, M. A. Brentjens, A. G. de Bruyn, B. Ciardi, V. Jelić, L. V. E. Koopmans, P. Labropoulos, G. Mellema, A. Offringa, V. N. Pandey, A. H. Pawlik, J. Schaye, R. M. Thomas, and S. Yatawatta. Power spectrum extraction for redshifted 21-cm Epoch of Reionization experiments: the LOFAR case. *Mon.Not.Roy.Astron.Soc.*, 405:2492–2504, July 2010. doi: 10.1111/j.1365-2966.2010.16628.x. 8, 48

J. Harnois-Déraps, U.-L. Pen, I. T. Iliev, H. Merz, J. D. Emberson, and V. Desjacques. High-performance P^3M N-body code: CUBEP^{3}M. *Mon.Not.Roy.Astron.Soc.*, 436:540–559, November 2013. doi: 10.1093/mnras/stt1591. 63

E. Hecht. *Optics 4th edition*. Addison-Wesley, 2001. 52

A. Hewish. The diffraction of radio waves in passing through a phase-changing ionosphere. *Proceedings of the Royal Society of London. Series A. Mathematical and Physical Sciences*, 209(1096):81–96, 1951. doi: 10.1098/rspa.1951.0189. URL http://rspa.royalsocietypublishing.org/content/209/1096/81.abstract. 11

A. Hewish. The diffraction of galactic radio waves as a method of investigating the irregular structure of the ionosphere. *Proceedings of the Royal Society of London. Series A. Mathematical and Physical Sciences*, 214(1119):494–514, 1952. doi: 10.1098/rspa.1952.0185. URL http://rspa.royalsocietypublishing.org/content/214/1119/494.abstract. 11

E. Hubble. A Relation between Distance and Radial Velocity among Extra-Galactic Nebulae. *Proceedings of the National Academy of Science*, 15:168–173, March 1929. doi: 10.1073/pnas.15.3.168. 18

Henry Hurwitz and R. Clark Jones. "A new calculus for the treatment of optical systems, II. Proof of three general equivalence theorems". *Journal of the Optical Society of America*, 31:493–499, 1941. 58

I. T. Iliev, P. R. Shapiro, and A. C. Raga. Minihalo photoevaporation during cosmic reionization: evaporation times and photon consumption rates. *Mon.Not.Roy.Astron.Soc.*, 361:405–414, August 2005. doi: 10.1111/j.1365-2966.2005.09155.x. 48

I. T. Iliev, G. Mellema, P. R. Shapiro, and U.-L. Pen. Self-regulated reionization. *Mon.Not.Roy.Astron.Soc.*, 376:534–548, April 2007. doi: 10.1111/j.1365-2966.2007.11482.x. 48, 63

I. T. Iliev, G. Mellema, P. R. Shapiro, U.-L. Pen, Y. Mao, J. Koda, and K. Ahn. Can 21-cm observations discriminate between high-mass and low-mass galaxies as reionization sources? *Mon.Not.Roy.Astron.Soc.*, 423:2222–2253, July 2012. doi: 10.1111/j.1365-2966.2012.21032.x. 64, 96

I. T. Iliev, G. Mellema, K. Ahn, P. R. Shapiro, Y. Mao, and U.-L. Pen. Simulating cosmic reionization: how large a volume is large enough? *MNRAS*, 439:725–743, March 2014. doi: 10.1093/mnras/stt2497. 124

Ilian T. Iliev, Garrelt Mellema, Ue-Li Pen, Hugh Merz, Paul R. Shapiro, and Marcelo A. Alvarez. Simulating cosmic reionization at large scales i: the geometry of reionization. *Mon.Not.Roy.Astron.Soc.*, 369:1625–1638, 2006. URL http://arxiv.org/abs/astro-ph/0512187. 63, 64, 94, 100

V. Jelić, S. Zaroubi, P. Labropoulos, G. Bernardi, A. G. de Bruyn, and L. V. E. Koopmans. Realistic simulations of the Galactic polarized foreground: consequences for 21-cm reionization detection experiments. *MNRAS*, 409:1647–1659, December 2010. doi: 10.1111/j.1365-2966.2010.17407.x. 81

R. Clark Jones. "A new calculus for the treatment of optical systems, I. Description and Discussion of the Calculus". *Journal of the Optical Society of America*, 31:488–493, 1941a. 58

R. Clark Jones. "A new calculus for the treatment of optical systems, III. The Sohncke Theory of optical activity". *Journal of the Optical Society of America*, 31:500–503, 1941b. 58

S. Joudaki, O. Doré, L. Ferramacho, M. Kaplinghat, and M. G. Santos. Primordial Non-Gaussianity from the 21 cm Power Spectrum during the Epoch of Reionization. *Physical Review Letters*, 107(13):131304, September 2011. doi: 10.1103/PhysRevLett.107.131304. 136, 139

A. A. Kaurov and N. Y. Gnedin. Effect of Halo Bias and Lyman Limit Systems on the History of Cosmic Reionization. *ApJ*, 771:35, July 2013. doi: 10.1088/0004-637X/771/1/35. 47

K. Kohler and N. Y. Gnedin. Lyman Limit Systems in Cosmological Simulations. *ApJ*, 655:685–690, February 2007. doi: 10.1086/510443. 49

E. Komatsu, J. Dunkley, M. R. Nolta, C. L. Bennett, B. Gold, G. Hinshaw, N. Jarosik, D. Larson, M. Limon, L. Page, D. N. Spergel, M. Halpern, R. S. Hill, A. Kogut, S. S. Meyer, G. S. Tucker, J. L. Weiland, E. Wollack, and E. L. Wright. Five-Year Wilkinson Microwave Anisotropy Probe Observations: Cosmological Interpretation. *ApJS*, 180:330–376, February 2009. doi: 10.1088/0067-0049/180/2/330. 31, 32

L. V. E. Koopmans. Ionospheric Power-spectrum Tomography in Radio Interferometry. *ApJ*, 718:963–971, August 2010. doi: 10.1088/0004-637X/718/2/963. 11

G. Lemaître. Un Univers homogène de masse constante et de rayon croissant rendant compte de la vitesse radiale des nébuleuses extra-galactiques. *Annales de la Societe Scietifique de Bruxelles*, 47:49–59, 1927. 18

G. Lemaître. The Beginning of the World from the Point of View of Quantum Theory. *Nature*, 127:706, May 1931. doi: 10.1038/127706b0. 18

A. Lewis. The real shape of non-Gaussianities. *Journal of Cosmology and Astroparticle Physics*, 10:026, October 2011. doi: 10.1088/1475-7516/2011/10/026. 31, 136

Antony Lewis, Anthony Challinor, and Anthony Lasenby. Efficient computation of CMB anisotropies in closed FRW models. *Astrophys. J.*, 538:473–476, 2000. 63

A. Liddle. *An Introduction to Modern Cosmology, Second Edition*. Wiley, May 2003. 20, 23

A. Lidz, E. J. Baxter, P. Adshead, and S. Dodelson. Primordial non-Gaussianity and reionization. *Physical Review D*, 88(2):023534, July 2013. doi: 10.1103/PhysRevD.88.023534. 136, 139

A. Linde. *Inflationary theory versus the ekpyrotic/cyclic scenario.*, pages 801–838. November 2003. 29

A. D. Linde. A new inflationary universe scenario: A possible solution of the horizon, flatness, homogeneity, isotropy and primordial monopole problems. *Physics Letters B*, 108:389–393, February 1982. doi: 10.1016/0370-2693(82)91219-9. 25

A. Loeb. First Light. *ArXiv Astrophysics e-prints*, March 2006. 41, 43

F. Löffler, J. Faber, E. Bentivegna, T. Bode, P. Diener, R. Haas, I. Hinder, B. C. Mundim, C. D. Ott, E. Schnetter, G. Allen, M. Campanelli, and P. Laguna. The Einstein Toolkit: a community computational infrastructure for relativistic astrophysics. *Classical and Quantum Gravity*, 29(11):115001, June 2012. doi: 10.1088/0264-9381/29/11/115001. 75

C. J. Lonsdale, R. J. Cappallo, M. F. Morales, F. H. Briggs, L. Benkevitch, J. D. Bowman, J. D. Bunton, S. Burns, B. E. Corey, L. Desouza, S. S. Doeleman, M. Derome, A. Deshpande, M. R. Gopala, L. J. Greenhill, D. E. Herne, J. N. Hewitt, P. A. Kamini, J. C. Kasper, B. B. Kincaid, J. Kocz, E. Kowald, E. Kratzenberg, D. Kumar, M. J. Lynch, S. Madhavi, M. Matejek, D. A. Mitchell, E. Morgan, D. Oberoi, S. Ord, J. Pathikulangara, T. Prabu, A. Rogers, A. Roshi, J. E. Salah, R. J. Sault, N. U. Shankar, K. S. Srivani, J. Stevens, S. Tingay, A. Vaccarella, M. Waterson, R. B. Wayth, R. L. Webster, A. R. Whitney, A. Williams, and C. Williams. The Murchison Widefield Array: Design Overview. *IEEE Proceedings*, 97:1497–1506, August 2009. doi: 10.1109/JPROC.2009.2017564. 8, 48

S. Lorenzoni. Star-Forming Galaxies at z˜8-9 from HST/WFC3: Implications for Reionization. In *Galaxy Formation*, page 22P, July 2011. 47

D. H. Lyth and A. A. Riotto. Particle physics models of inflation and the cosmological density perturbation. *Phys.Rept.*, 314:1–146, June 1999. doi: 10.1016/S0370-1573(98)00128-8. 6

Gordon J. MacDonald. Spectral analysis of time series generated by nonlinear processes. *Reviews of Geophysics*, 27(4):449–469, 1989. ISSN 1944-9208. doi: 10.1029/RG027i004p00449. URL http://dx.doi.org/10.1029/RG027i004p00449. 31

Y. Mao, P. R. Shapiro, G. Mellema, I. T. Iliev, J. Koda, and K. Ahn. Redshift-space distortion of the 21-cm background from the epoch of reionization - I. Methodology re-examined. *MNRAS*, 422:926–954, May 2012. doi: 10.1111/j.1365-2966.2012.20471.x. 110, 137, 173, 174

Y. Mao, A. D'Aloisio, J. Zhang, and P. R. Shapiro. Primordial non-Gaussianity estimation using 21 cm tomography from the epoch of reionization. *Physical Review D*, 88(8):081303, October 2013. doi: 10.1103/PhysRevD.88.081303. 136, 139

M. McQuinn, A. Lidz, O. Zahn, S. Dutta, L. Hernquist, and M. Zaldarriaga. The morphology of HII regions during reionization. *Mon.Not.Roy.Astron.Soc.*, 377:1043–1063, May 2007. doi: 10.1111/j.1365-2966.2007.11489.x. 47

Matthew McQuinn, S. Peng Oh, and C.-A. Faucher-Giguere. On lyman-limit systems and

the evolution of the intergalactic ionizing background. *Astrophys.J.743:82, 2011*, 01 2011. URL http://arxiv.org/abs/1101.1964. 49, 68, 114

G. Mellema, L. V. E. Koopmans, F. A. Abdalla, G. Bernardi, B. Ciardi, S. Daiboo, A. G. de Bruyn, K. K. Datta, H. Falcke, A. Ferrara, I. T. Iliev, F. Iocco, V. Jelić, H. Jensen, R. Joseph, P. Labroupoulos, A. Meiksin, A. Mesinger, A. R. Offringa, V. N. Pandey, J. R. Pritchard, M. G. Santos, D. J. Schwarz, B. Semelin, H. Vedantham, S. Yatawatta, and S. Zaroubi. Reionization and the Cosmic Dawn with the Square Kilometre Array. *Experimental Astronomy*, 36:235–318, August 2013. doi: 10.1007/s10686-013-9334-5. 47

G. Mellema, L. Koopmans, H. Shukla, K. K. Datta, A. Mesinger, S. Majumdar, and on behalf of the CD/EoR Science Working Group. HI tomographic imaging of the Cosmic Dawn and Epoch of Reionization with SKA. *Accepted for publication in the SKA Science Book 'Advancing Astrophysics with the Square Kilometre Array', to appear in 2015. PoS (AASKA14) 010*, 2015. 171

Garrelt Mellema, Ilian T. Iliev, Marcelo A. Alvarez, and Paul R. Shapiro. C^2-Ray: A new method for photon-conserving transport of ionizing radiation. *New Astronomy*, 11(5): 374–395, March 2006a. URL http://arxiv.org/abs/astro-ph/0508416. 64, 71, 72

Garrelt Mellema, Ilian T. Iliev, Ue-Li Pen, and Paul R. Shapiro. Simulating cosmic reionization at large scales ii: the 21-cm emission features and statistical signals. *Mon.Not.Roy.Astron.Soc.*, 372:679–692, 2006b. URL http://arxiv.org/abs/astro-ph/0603518. 48, 63

J. Miralda-Escudé. On the Evolution of the Ionizing Emissivity of Galaxies and Quasars Required by the Hydrogen Reionization. *ApJ*, 597:66–73, November 2003. doi: 10.1086/378286. 47, 68

C. W. Misner, K. S. Thorne, and J. A. Wheeler. *Gravitation*. W.H. Freeman and Co., 1973. 20

M. F. Morales, J. D. Bowman, and J. N. Hewitt. Improving Foreground Subtraction in Statistical Observations of 21 cm Emission from the Epoch of Reionization. *ApJ*, 648: 767–773, September 2006. doi: 10.1086/506135. 11

R. J. Nijober. UV Bricks. *LOFAR - Project Documentation*, 2005. 91

J. E. Noordam and O. M. Smirnov. The MeqTrees software system and its use for third-generation calibration of radio interferometers. *Astronomy & Astrophysics Journal*, 524: A61, December 2010. doi: 10.1051/0004-6361/201015013. 61, 90

J. E. Noordam and O. M. Smirnov. MeqTrees: Software package for implementing Measurement Equations, September 2012. Astrophysics Source Code Library. 61

A. R. Offringa, A. G. de Bruyn, M. Biehl, S. Zaroubi, G. Bernardi, and V. N. Pandey. Post-correlation radio frequency interference classification methods. *MNRAS*, 405:155–167, June 2010a. doi: 10.1111/j.1365-2966.2010.16471.x. 11

A. R. Offringa, A. G. de Bruyn, S. Zaroubi, and M. Biehl. Post-correlation RFI detection. In *RFI Mitigation Workshop*, May 2010b. 11

D. E. Osterbrock. *Astrophysics of gaseous nebulae and active galactic nuclei.* University Science Books, 1989. 65

G. Paciga, T.-C. Chang, Y. Gupta, R. Nityanada, J. Odegova, U.-L. Pen, J. B. Peterson, J. Roy, and K. Sigurdson. The GMRT Epoch of Reionization experiment: a new upper limit on the neutral hydrogen power spectrum at z $\sim$ 8.6. *Mon.Not.Roy.Astron.Soc.*, 413:1174–1183, May 2011. doi: 10.1111/j.1365-2966.2011.18208.x. 8, 48

H. Park, P. R. Shapiro, E. Komatsu, I. T. Iliev, K. Ahn, and G. Mellema. The Kinetic Sunyaev-Zel'dovich Effect as a Probe of the Physics of Cosmic Reionization: The Effect of Self-regulated Reionization. *ApJ*, 769:93, June 2013. doi: 10.1088/0004-637X/769/2/93. 45

A. R. Parsons, D. C. Backer, G. S. Foster, M. C. H. Wright, R. F. Bradley, N. E. Gugliucci, C. R. Parashare, E. E. Benoit, J. E. Aguirre, D. C. Jacobs, C. L. Carilli, D. Herne, M. J. Lynch, J. R. Manley, and D. J. Werthimer. The Precision Array for Probing the Epoch of Re-ionization: Eight Station Results. *Astronomical Journal*, 139:1468–1480, April 2010. doi: 10.1088/0004-6256/139/4/1468. 8, 48

J. A. Peacock. *Cosmological Physics.* January 1999. 29

P. J. E. Peebles and J. T. Yu. Primeval Adiabatic Perturbation in an Expanding Universe. *ApJ*, 162:815, December 1970. doi: 10.1086/150713. 45

R. Penrose. Difficulties with inflationary cosmology. *Annals of the New York Academy of Sciences*, 571:249–264, December 1989. doi: 10.1111/j.1749-6632.1989.tb50513.x. 29

A. A. Penzias and R. W. Wilson. A Measurement of Excess Antenna Temperature at 4080 Mc/s. *Astrophysical Journal*, 142:419–421, July 1965. doi: 10.1086/148307. 18

P. Petitjean, J. K. Webb, M. Rauch, R. F. Carswell, and K. Lanzetta. Evidence for structure in the H I column density distribution of QSO absorbers. *MNRAS*, 262: 499–505, May 1993. 67

Planck Collaboration, P. A. R. Ade, N. Aghanim, C. Armitage-Caplan, M. Arnaud, M. Ashdown, F. Atrio-Barandela, J. Aumont, C. Baccigalupi, A. J. Banday, and et al. Planck 2013 results. I. Overview of products and scientific results. *ArXiv e-prints*, March 2013. 5, 6, 7, 18, 45, 47, 136

Planck Collaboration, R. Adam, P. A. R. Ade, N. Aghanim, M. Arnaud, J. Aumont, C. Baccigalupi, A. J. Banday, R. B. Barreiro, J. G. Bartlett, and et al. Planck intermediate results. XXX. The angular power spectrum of polarized dust emission at intermediate and high Galactic latitudes. *ArXiv e-prints*, September 2014. 7, 19

N. J. Popławski. Cosmology with torsion: An alternative to cosmic inflation. *Physics Letters B*, 694:181–185, November 2010. doi: 10.1016/j.physletb.2010.09.056. 29

W. H. Press, S. A. Teukolsky, W. T. Vetterling, and B. P. Flannery. *Numerical recipes in FORTRAN. The art of scientific computing*. Press Syndicate of the University of Cambridge, 1992. 100

J. R. Pritchard and A. Loeb. 21 cm cosmology in the 21st century. *Reports on Progress in Physics*, 75(8):086901, August 2012. doi: 10.1088/0034-4885/75/8/086901. 5, 40, 42, 43, 44

J. X. Prochaska, J. M. O'Meara, and G. Worseck. A Definitive Survey for Lyman Limit Systems at $z \sim 3.5$ with the Sloan Digital Sky Survey. *ApJ,*, 718:392–416, July 2010. doi: 10.1088/0004-637X/718/1/392. 49

D. Regan, P. Mukherjee, and D. Seery. General CMB bispectrum analysis using wavelets and separable modes. *Phys. Rev. D*, 88(4):043512, August 2013. doi: 10.1103/PhysRevD.88.043512. 34

D. M. Regan. *Measuring CMB non-Gaussianity as a probe of Inflation and Cosmic Strings*. PhD thesis, PhD Thesis, 2011, 2011. 33, 145

J. Ribaudo, N. Lehner, and J. C. Howk. A Hubble Space Telescope Study of Lyman Limit Systems: Census and Evolution. *ApJ*, 736:42, July 2011. doi: 10.1088/0004-637X/736/1/42. 49

W. L. W. Sargent. The Origin and Evolution of Large-Scale Structure in the Universe. In J. de Boer, E. dal, and O. Ulfbeck, editors, *The Lesson of Quantum Theory*, page 263, 1986. 46

R. J. Sault, J. P. Hamaker, and J. D. Bregman. Understanding radio polarimetry. II. Instrumental calibration of an interferometer array. *Astronomy & Astrophysics Supplement*, 117:149–159, May 1996. 51

R. T. Schilizzi. The Square Kilometer Array. In J. M. Oschmann, Jr., editor, *Ground-based Telescopes*, volume 5489 of *Society of Photo-Optical Instrumentation Engineers (SPIE) Conference Series*, pages 62–71, October 2004. doi: 10.1117/12.551206. 48

M. M. Schmittfull, D. M. Regan, and E. P. S. Shellard. Fast estimation of gravitational and primordial bispectra in large scale structures. *Phys. Rev. D*, 88(6):063512, September 2013. doi: 10.1103/PhysRevD.88.063512. 146

B. Schutz. *A First Course in General Relativity*. Cambridge University Press, May 2009. 20

U. Seljak and M. Zaldarriaga. A Line-of-Sight Integration Approach to Cosmic Microwave Background Anisotropies. *ApJ*, 469:437, October 1996. doi: 10.1086/177793. 63

P. R. Shapiro, Y. Mao, I. T. Iliev, G. Mellema, K. K. Datta, K. Ahn, and J. Koda. Will Nonlinear Peculiar Velocity and Inhomogeneous Reionization Spoil 21 cm Cosmology from the Epoch of Reionization? *Physical Review Letters*, 110(15):151301, April 2013. doi: 10.1103/PhysRevLett.110.151301. 176

P. A. Shaver, R. A. Windhorst, P. Madau, and A. G. de Bruyn. Can the reionization epoch be detected as a global signature in the cosmic background? *AAP*, 345:380–390, May 1999. 10

Hemant Shukla. Infrastructure for Astrophysics Applications Computing (ISAAC). , 2010-2014. URL http://iccs.lbl.gov/research/isaac/index.html. 13

Hemant Shukla, Hsi-Yu Schive, Tak-Pong Woo, and Tzihong Chiueh. Multi-science applications with single codebase - GAMER - for massively parallel architectures. In Scott Lathrop, Jim Costa, and William Kramer, editors, *Conference on High Performance Computing Networking, Storage and Analysis, SC 2011, Seattle, WA, USA, November 12-18, 2011*, page 37. ACM, 2011. ISBN 978-1-4503-0771-0. doi: 10.1145/2063384.2063433. URL http://doi.acm.org/10.1145/2063384.2063433. 75

Hemant Shukla, G. Mellema, I. T. Iliev, L. V. E. Koopmans, and O. M. Smirnov. Observing the Epoch of Reionization and Dark Ages with 21-cm: III - In the presence of Lyman Limit Systems. *(In Preparation)*, 2014. 115

O. M. Smirnov. Revisiting the radio interferometer measurement equation. I. A full-sky Jones formalism. *Astronomy & Astrophysics Journal*, 527:A106, March 2011a. doi: 10.1051/0004-6361/201016082. 51, 58, 59, 90

O. M. Smirnov. Revisiting the radio interferometer measurement equation. II. Calibration and direction-dependent effects. *Astronomy & Astrophysics Journal*, 527:A107, March 2011b. doi: 10.1051/0004-6361/201116434. 51, 90, 126

O. M. Smirnov. Revisiting the radio interferometer measurement equation. III. Addressing direction-dependent effects in 21 cm WSRT observations of 3C 147. *Astronomy & Astrophysics Journal*, 527:A108, March 2011c. doi: 10.1051/0004-6361/201116435. 51, 90

O. M. Smirnov. Revisiting the radio interferometer measurement equation. IV. A generalized tensor formalism. *Astronomy & Astrophysics Journal*, 531:A159, July 2011d. doi: 10.1051/0004-6361/201116764. 51, 61, 90

E. Sobacchi and A. Mesinger. Inhomogeneous recombinations during cosmic reionization.

Mon.Not.Roy.Astron.Soc., 440:1662–1673, May 2014. doi: 10.1093/mnras/stu377. 47, 49, 66, 115

Antoinette Songaila and Lennox L. Cowie. The evolution of lyman limit absorption systems to redshift six. *ApJ,*, 721:1448–1466, 2010. URL http://arxiv.org/abs/1007.3262. 49, 67, 68, 69, 114

P. J. Steinhardt, N. Turok, and G. D. Starkman. Endless Universe: Beyond the Big Bang. *Physics Today*, 61(1):59, 2008. doi: 10.1063/1.2835155. 29

N. Sugiyama. Cosmic Background Anisotropies in Cold Dark Matter Cosmology. *ApJS*, 100:281, October 1995. doi: 10.1086/192220. 45

R. A. Sunyaev. Fluctuations of the microwave background radiation. In M. S. Longair and J. Einasto, editors, *Large Scale Structures in the Universe*, volume 79 of *IAU Symposium*, pages 393–402, 1978. 19

R. A. Sunyaev and Y. B. Zeldovich. The Observations of Relic Radiation as a Test of the Nature of X-Ray Radiation from the Clusters of Galaxies. *Comments on Astrophysics and Space Physics*, 4:173, November 1972. 45

C. Tasse, S. van der Tol, J. van Zwieten, G. van Diepen, and S. Bhatnagar. Applying full polarization A-Projection to very wide field of view instruments: An imager for LOFAR. *AAP*, 553:A105, May 2013. doi: 10.1051/0004-6361/201220882. 11

G. B. Taylor, C. L. Carilli, and R. A. Perley, editors. *Synthesis Imaging in Radio Astronomy II*, volume 180 of *Astronomical Society of the Pacific Conference Series*, 1999. 51

A. R. Thompson, J. M. Moran, and G. W. Swenson. *Interferometry and Synthesis in Radio Astronomy, John Wiley Sons, 2001.* John Wiley & Sons, 2001. 51, 53, 120

D. Tytler. QSO Lyman limit absorption. *Nature*, 298:427–432, July 1982. doi: 10.1038/298427a0. 49

M. P. van Haarlem, M. W. Wise, A. W. Gunst, G. Heald, J. P. McKean, J. W. T. Hessels, A. G. de Bruyn, R. Nijboer, J. Swinbank, R. Fallows, M. Brentjens, A. Nelles, R. Beck, H. Falcke, R. Fender, J. Hörandel, L. V. E. Koopmans, G. Mann, G. Miley,

H. Röttgering, B. W. Stappers, R. A. M. J. Wijers, S. Zaroubi, M. van den Akker, A. Alexov, J. Anderson, K. Anderson, A. van Ardenne, M. Arts, A. Asgekar, I. M. Avruch, F. Batejat, L. Bähren, M. E. Bell, M. R. Bell, I. van Bemmel, P. Bennema, M. J. Bentum, G. Bernardi, P. Best, L. Bîrzan, A. Bonafede, A.-J. Boonstra, R. Braun, J. Bregman, F. Breitling, R. H. van de Brink, J. Broderick, P. C. Broekema, W. N. Brouw, M. Brüggen, H. R. Butcher, W. van Cappellen, B. Ciardi, T. Coenen, J. Conway, A. Coolen, A. Corstanje, S. Damstra, O. Davies, A. T. Deller, R.-J. Dettmar, G. van Diepen, K. Dijkstra, P. Donker, A. Doorduin, J. Dromer, M. Drost, A. van Duin, J. Eislöffel, J. van Enst, C. Ferrari, W. Frieswijk, H. Gankema, M. A. Garrett, F. de Gasperin, M. Gerbers, E. de Geus, J.-M. Grießmeier, T. Grit, P. Gruppen, J. P. Hamaker, T. Hassall, M. Hoeft, H. A. Holties, A. Horneffer, A. van der Horst, A. van Houwelingen, A. Huijgen, M. Iacobelli, H. Intema, N. Jackson, V. Jelic, A. de Jong, E. Juette, D. Kant, A. Karastergiou, A. Koers, H. Kollen, V. I. Kondratiev, E. Kooistra, Y. Koopman, A. Koster, M. Kuniyoshi, M. Kramer, G. Kuper, P. Lambropoulos, C. Law, J. van Leeuwen, J. Lemaitre, M. Loose, P. Maat, G. Macario, S. Markoff, J. Masters, R. A. McFadden, D. McKay-Bukowski, H. Meijering, H. Meulman, M. Mevius, E. Middelberg, R. Millenaar, J. C. A. Miller-Jones, R. N. Mohan, J. D. Mol, J. Morawietz, R. Morganti, D. D. Mulcahy, E. Mulder, H. Munk, L. Nieuwenhuis, R. van Nieuwpoort, J. E. Noordam, M. Norden, A. Noutsos, A. R. Offringa, H. Olofsson, A. Omar, E. Orrú, R. Overeem, H. Paas, M. Pandey-Pommier, V. N. Pandey, R. Pizzo, A. Polatidis, D. Rafferty, S. Rawlings, W. Reich, J.-P. de Reijer, J. Reitsma, G. A. Renting, P. Riemers, E. Rol, J. W. Romein, J. Roosjen, M. Ruiter, A. Scaife, K. van der Schaaf, B. Scheers, P. Schellart, A. Schoenmakers, G. Schoonderbeek, M. Serylak, A. Shulevski, J. Sluman, O. Smirnov, C. Sobey, H. Spreeuw, M. Steinmetz, C. G. M. Sterks, H.-J. Stiepel, K. Stuurwold, M. Tagger, Y. Tang, C. Tasse, I. Thomas, S. Thoudam, M. C. Toribio, B. van der Tol, O. Usov, M. van Veelen, A.-J. van der Veen, S. ter Veen, J. P. W. Verbiest, R. Vermeulen, N. Vermaas, C. Vocks, C. Vogt, M. de Vos, E. van der Wal, R. van Weeren, H. Weggemans, P. Weltevrede, S. White, S. J. Wijnholds, T. Wilhelmsson, O. Wucknitz, S. Yatawatta, P. Zarka, A. Zensus, and J. van Zwieten. LOFAR: The LOw-Frequency ARray. *AAP*, 556:A2, August 2013. doi: 10.1051/0004-6361/201220873. 8, 9

W. A. Watson, I. T. Iliev, A. D'Aloisio, A. Knebe, P. R. Shapiro, and G. Yepes. The halo mass function through the cosmic ages. *MNRAS*, 433:1230–1245, August 2013. doi: 10.1093/mnras/stt791. 64

T. L. Wilson, K. Rohlfs, and S. Hüttemeister. *Tools of Radio Astronomy*. Springer-Verlag Berlin Heidelberg, 2013. doi: 10.1007/978-3-642-39950-3. 51

B. Winkel, J. Kerp, and S. Stanko. RFI detection by automated feature extraction and statistical analysis. *Astronomische Nachrichten*, 328:68–79, January 2007. doi: 10.1002/asna.200610661. 11

S. A. Wouthuysen. On the excitation mechanism of the 21-cm (radio-frequency) interstellar hydrogen emission line. *AJ*, 57:31–32, 1952. doi: 10.1086/106661. 42

S. Yatawatta. Fundamental Limitations of Pixel Based Image Deconvolution in Radio Astronomy. *ArXiv e-prints*, August 2010. 119

O. Zahn, A. Lidz, M. McQuinn, S. Dutta, L. Hernquist, M. Zaldarriaga, and S. R. Furlanetto. Simulations and Analytic Calculations of Bubble Growth during Hydrogen Reionization. *ApJ*, 654:12–26, January 2007. doi: 10.1086/509597. 100, 103

M. Zaldarriaga. Polarization of the microwave background in reionized models. *Phys. Rev. D*, 55:1822–1829, February 1997. doi: 10.1103/PhysRevD.55.1822. 45

S. Zaroubi. The Epoch of Reionization. In T. Wiklind, B. Mobasher, and V. Bromm, editors, *Astrophysics and Space Science Library*, volume 396 of *Astrophysics and Space Science Library*, page 45, 2013. doi: 10.1007/978-3-642-32362-1_2. 45

J. Zhang, L. Hui, and Z. Haiman. A linear perturbation theory of inhomogeneous reionization. *MNRAS*, 375:324–336, February 2007. doi: 10.1111/j.1365-2966.2006.11311.x. 140

Appendix A

Publications

The papers related to the research in this thesis are in the works and will be submitted in the coming months. The papers currently under preparation are,

Published

1. H I tomographic imaging of the Cosmic Dawn and Epoch of Reionization with SKA. G. Mellema, L. Koopmans, H. Shukla, K. K. Datta, A. Mesinger, S. Majumdar, and on behalf of the CD/EoR Science Working Group. Accepted for publication in the SKA Science Book Advancing Astrophysics with the Square Kilometre Array, to appear in 2015. PoS (AASKA14) 010, 2015. [Mellema et al., 2015]

Submitted to MNRAS (under review)

2. The Effects of Lyman-Limit Systems on the Evolution and Observability of the Epoch of Reionization. Hemant Shukla, Garrlet Mellema, Ilian T, Iliev, and Paul R. Shapiro. [In preparation, 2014]

In Preparation

3. Observing the Epoch of Reionization & Dark Ages with redshifted 21-cm, I. With the next-generation SKA-class interferometry arrays. Hemant Shukla, Leon V. E. Koopmans, Oleg M. Smirnov, and Ilian T. Iliev. [In preparation, 2014]

4. Observing the Epoch of Reionization & Dark Ages with redshifted 21-cm. II. Searching for Primordial non-Gaussianity. Hemant Shukla, Donough Regan, Andrew Liddle, Anson D'Aloisio, and Ilian T. Iliev. [In preparation, 2014]

5. Observing the Epoch of Reionization & Dark Ages with redshifted 21-cm. III. In the presences of the Lyman-limit Systems. Hemant Shukla, Garrelt Mellema, and Ilian T. Iliev. [In preparation, 2014]

Appendix B

The MM-RRM Power Spectrum and Definitions

The first order statistical property from the observational 21-cm tomography data is the spherically averaged power spectrum, P_{21}, of the differential brightness temperature, δT_b, defined as following,

$$\langle \widetilde{\delta T_b^\star}(\mathbf{k}) \widetilde{\delta T_b}(\mathbf{k}') \rangle = (2\pi^3) P_{21}(\mathbf{k}) \delta_D^3(\mathbf{k} - \mathbf{k}') \tag{B.1}$$

where, $\widetilde{\delta T_b}$ is the Fourier transform of the differential brightness temperature, $\widetilde{\delta T_b^\star}$ is the complex conjugate, and $\delta_{\rm D}^3$ is the three-dimensional Dirac delta function representing the sampling function of the Fourier transformed quantity. The power spectrum is customarily represented as a dimensionless quantity given as following,

$$\Delta^2_{\text{21-cm}}(k) = \frac{k^3}{2\pi^2} P_{21}(k) \tag{B.2}$$

The power spectrum of a volume represented in real space is isotropic. However, in the redshift space (observed data), the power spectrum is a function of the wave-vector $\mathbf{k}$. Now the power spectrum is decomposed into polynomial components in the cosine of the angle of the wave vector k and the the line of sight denoted as $\mu = k_{\parallel}/|\mathbf{k}|$. Barkana and Loeb [2005] and Mao et al. [2012] separately showed that the moments of the polynomial represent power spectra of different physical processes. The decomposed power spectrum

is written as,

$$P_{21}(k,\mu) = P_{\mu^0}(k) + P_{\mu^2}(k)\mu^2 + P_{\mu^4}(k)\mu^4 \tag{B.3}$$

and, the moments are given as,

$$\begin{aligned} P_{\mu^0} &= \widehat{\delta T_b}^{\,2}\; P_{\delta_{\rho_{\rm HI}},\delta_{\rho_{\rm HI}}}(k) \\ P_{\mu^2} &= 2\widehat{\delta T_b}^{\,2}\; P_{\delta_{\rho_{\rm HI}},\delta_{\rho_{\rm H}}}(k) \\ P_{\mu^4} &= \widehat{\delta T_b}^{\,2}\; P_{\delta_{\rho_{\rm H}},\delta_{\rho_{\rm H}}}(k) \end{aligned} \tag{B.4}$$

where, $P_{a,a}$ is the autocorrelation of the field $a(\mathbf{x})$, and $P_{a,b}$ is the cross-correlation of the fields $a(\mathbf{x})$ and $b(\mathbf{x})$.

There are various schemes for estimating the power spectrum, in this letter we demonstrate the results from the *mesh-to-mesh real-to-redshift-space mapping* (MM-RRM) methodology from Mao et al. [2012]. The MM-RRM ties the ionization fraction and density and velocity files as input to estimate the power spectrum. The output files, `_monopole_` and `_mudecomp_` have the following columns,

Columns in `_monopole_` files

k (unit less): k modes unit less

Nmode: N modes

k (h/Mpc): k mode in comoving coordinates

$\Delta^2_{21\text{-}cm(NL)}$: nonlinear power spectrum in redshift-space.

$\Delta^2_{21\text{-}cm(FL)}$: linear power spectrum as in Barkana-Loeb formula [Barkana and Loeb, 2005]

$\Delta^2_{21\text{-}cm(QL)}$: quasi-linear power spectrum

$\Delta^2_{HI(FL)}$: this is another version of quasi-linear power spectrum

$\Delta^2_{HI(NL)}$: this is second-order nonlinear correction to the quasi-linear power spectrum

$\Delta^2_{\mu_0}$: 0th-moment power spectrum in the quasi-linear formula

$\Delta^2_{\mu_2}$: same, but the 2nd-moment

$\Delta^2_{\mu_4}$: same, but the 4th-moment

The $\mu - decomp$ columns in `_monpole_` files are the predictions in the quasi-linear μ-decomposition scheme. The Figure B.1, shows the each of the `_monopole_` columns for the simulation of volume size $114h^{-1}Mpc$ at mass weighted ionization fraction of 50% at $z = 9.457$.

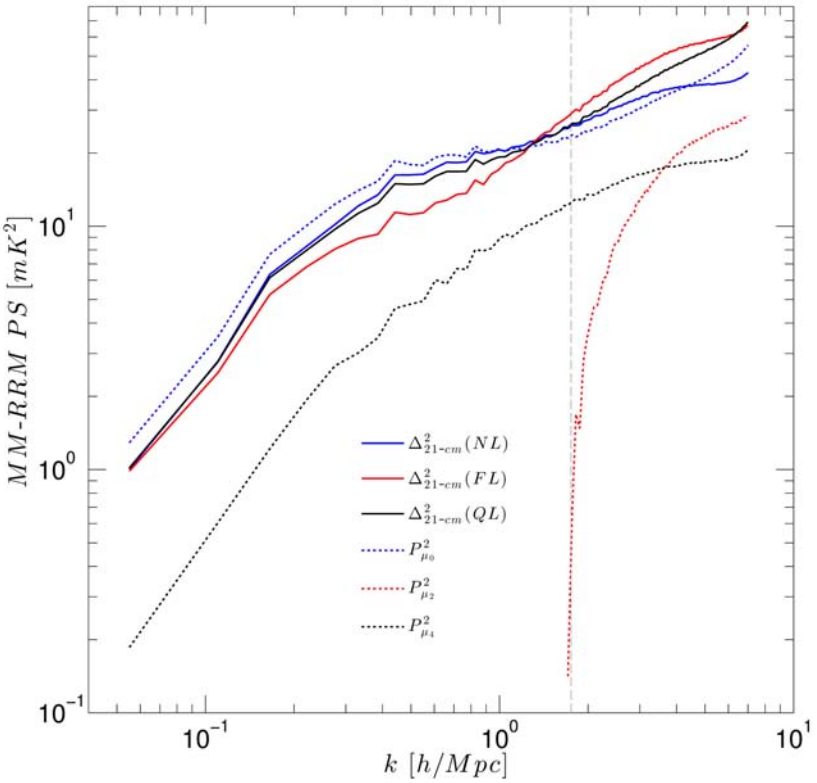

Figure B.1: The grey vertical line at $k_N^{256}/4 = 1.75h/Mpc$ marks the limit beyond which the errors in the estimation of PS in MM-RRM scheme are large.

Columns in `_mudecomp_` files

k (unit less): k modes unit less

Nmode: N modes

k (h/Mpc): k mode in comoving coordinates

$\Delta^2_{\mu_0}$: 0th-moment power spectrum in the quasi-linear formula

$\Delta^2_{\mu_2}$: same, but the 2nd-moment

$\Delta^2_{\mu_4}$: same, but the 4th-moment

$\sigma(\Delta^2_{\mu_0})$: error in best-fit of 0th-moment

$\sigma(\Delta^2_{\mu_2})$: same, but for 2nd-moment

$\sigma(\Delta^2_{\mu_4})$: same, but for 4-th moment

$\Delta^2_{\mu_4}$(L): linear 4th-moment

The μ-decomp `_mudecomp_` files are the best-fit value of moments from the decomposition of three-dimensional power spectrum. The power spectra output misses some small k modes, because (i) the minimum mode that can do decomposition is $k = 2$ (three different angle μ for decomposition into three moments are needed), and (ii) the decomposition is practically binned logarithmically, so smallest k modes are grouped together into one bin. The errors of the best-fit moments are estimated in the process of χ^2 fitting the 3D power spectrum within a spherical k-shell into the assumed μ^4 decomposition, and the error in the 3D power spectrum is essentially the sampling variance for the number of available modes. For details see Shapiro et al. [2013]. The Figure B.2 shows the three estimated moments with the errors.

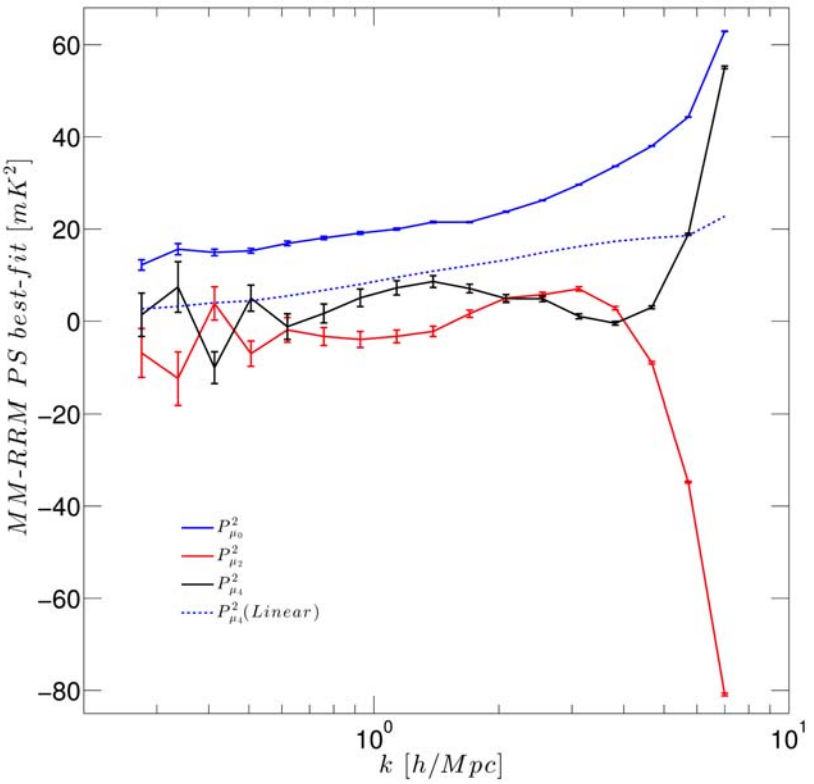

Figure B.2: The best-fit estimates of moments from 3D power spectrum.